DIPLOMA THESIS

Real-time artifact correction of EEG Signals acquired during simultaneous fMRI

Asmir Hrnic

Institute of Medical Engineering
Graz University of Technology
Kronesgasse 5, A - 8010 Graz

Supervisor:
Ao.Univ.-Prof. Dipl.-Ing. Dr.techn. Hermann Scharfetter

In collaboration with:

g.tec Guger Technologies OG
Herbersteinstrasse 60, A-8020 Graz

Supervisor:
Dipl.-Ing. Dr.techn. Günter Edlinger

Graz, (Month, Year)

Abstract

The advantage of a simultaneous recording of the electroencephalogram (EEG) and the functional magnetic tomography (fMRI) lies in the high temporal and spatial resolution of neural activity.

Due to the intensive magnetic fields of the MR-environment, the EEG signal is corrupted by the so called Imaging artifact (IA), as well as the Pulse Related artifact (PA). These artifacts must be corrected in real time, in conduction with EEG based Brain Computer Interface (BCI) experiments. Current artifact reduction methods were discussed and applied as real-time correction methods. The applied methods were tested on a subject by means of a motor imagery BCI and compared to measurements outside of MRI surroundings.

Keywords: EEG, fMRI, BCI, imaging artifacts, pulse related artifacts

Zusammenfassung

Der Vorteil einer simultanen Erfassung des Elektroenzephalogramms (EEG) und der funktionellen Magnetresonanztomographie (fMRT) liegt in der hohen zeitlichen sowie örtlichen Auflösung neuronaler Aktivität.

Aufgrund des intensiven magnetischen Feldes der MR-Umgebung, werden allerdings dem EEG-Signal der sogenannte Imaging Artefakt (IA), sowie der Pulse related Artefakt (PA) überlagert. Diese Artefakte müssen bei der Durchführung von EEG basierten Brain Computer Interface (BCI) Experimenten in Echtzeit korrigiert werden. Im Zuge dieser Arbeit wurden gängige Artefakt-Korrektur Methoden diskutiert und Methoden zur Echtzeit Korrektur umgesetzt. Die umgesetzten Methoden wurden anhand eines Motor Imagery BCI's an einem Probanden getestet und mit Messungen außerhalb der MRI Umgebung verglichen.

Statutory Declaration

I declare that I have authored this thesis independently, that I have not used other than the declared sources / resources, and that I have explicitly marked all material which has been quoted either literally or by content from the used sources.

december 16, 2011 _____

Signature

Acknowledgements

I would hereby like to thank everybody who co-operated on the accomplishment of this work.

First of all, I want to thank the chief executive of g.tec medical engineering GmbH, Dipl.-Ing. Dr.techn. Günter Edlinger for sharing the enthusiasm for this topic and providing the outstanding technical-methodical support and motivation for this work. Furthermore, I would like to thank all my co-workers, especially Dipl.-Ing. Franz Laundl, Dipl.-Ing. Thomas Maresch, Dipl.-Ing. Norbert Barry and Dipl.-Ing. Matthias Zeintlinger for their assistance and constructive discussions. A special thanks to Ing. Mag.rer. nat.Gunther Krausz, who invested a lot of patience, commitment and methodical knowledge in the course of the test measurements and evaluations. I am also thankful for the prompt and competent support from the company Micromed S.p.A.

Furthermore, I like to thank Ao.Univ.-Prof. Dipl.-Ing. Dr.techn. Hermann Scharfetter for the excellent supervision at the Technical University of Graz, as well as Dipl.-Ing. Clemens Diwoky and Dipl.-Ing. Peter Opriessnig for the valuable collaboration at the MRI scanner.

I am particularly pleased to say thank you to my dear friends. Especially I want to set Nikita Sharov, Johannes Zitz and Enes Karasuljic apart, who helped me with the technical realizations and measurements.

A special thank you goes to my parents Asim and Esmina, my grandparents Rasema and Mustafa, as well as my brother Said and his wife Emina for being part of my life and giving me the motivation and courage for my personal development. I also want to thank Neila for being with us and enriching our lives.

Finally, I would sincerely like to thank the person who had the most positive effect on me during the course of this work. She helped me not only with her linguistic skills, but she is also a wonderful friend and advisor. Hvala ti Admira, v. te.

Thank you,

Contents

1 Introduction

A *brain computer interface* (BCI) allows the control of computers and other electrical devices solely by means of human brain activity. The communication between the user and the device describes a closed communication loop, starting from the measurement of brain activity during a specific mental task (*paradigm*). This task contains a finite number of options which associate a computer command to the spatially and temporally resolved brain activity signal. The loop is closed if the intention during the performance of the paradigm was recognized properly and the command was executed accordingly (*feedback*).

The clinical applicability of this procedure depends heavily on the brain activity measurement method. The good temporal resolution, the simple signal processing and mobility of *electroencephalogram* (EEG) based BCI systems allow compact communication systems for *locked-in* patients, or individuals with motor impairments (Kübler, Kotchoubey *et al.*, 2007). The comparatively better spatial resolution of BCI systems based on *functional magnetic resonance imaging* (fMRI) provides the opportunity to extract not only cortical, but also sub-cortical brain areas for neuronal feedback (Caria, Veit *et al.*, 2007).

Since 1993, epilepsy research has encouraged the efforts to combine these two measurement methods, which have enabled the development of MRI-safe EEG systems (Mulert e Lemieux, 2010). The expected benefit of a combined EEG/fMRI examination is the acquisition of the brain activity with a high temporal and spatial resolution. However, these benefits are offset by a set of MRI related artifacts which affect the EEG signal. Over time, several methods were proposed to suppress these artifacts. The goal of the presented thesis is to extend an EEG based motor imagery BCI for a combined EEG/fMRI examination, in order to evaluate the possibility of real-time investigation of processes in the human brain during a BCI experiment. The special conditions associated with a BCI require real-time artifact suppression methods, which are realized in this work using MATLAB Simulink (MATLAB, 2003) development environment. These methods are tested by executing the BCI in MRI environment with a commercially available MRI-safe EEG amplifier, and compared to tests outside the MRI surroundings. Beforehand, an introduction part shows the physical coherences of EEG, fMRI and BCI and discusses the occurring artifacts during concurrent EEG/fMRI measurements and conventional artifact suppression methods.

2 Basics of EEG

The *electro encephalogram* (EEG) graphically describes the changes of electrical potentials of the human brain over time. The increasing signal can be measured by means of electrodes which are placed on the surface of the head (Schandry, 2006).

The sources of the measured potential differences are the so called *excitatory postsynaptic potentials* (EPSP's) or *inhibitory postsynaptic potentials* (IPSP's) respectively, which rely on changes of ionic concentrations in neurons. The potential of one neuron is too weak to be registered on the head surface, thus only superimposed potentials can be detected by the electrodes. So if many neurons generate the same potential differences, then the EEG signal amplitude increases, because the neurons work synchronized. The maximal amplitudes on the scalp are in the range of micro-volts. The further chapters give an overview on how to position the electrodes and which typical phenomena can be detected in the EEG.

2.1 Positioning the electrodes

The information processing of the human brain occurs in certain areas, depending on the type of input. For instance, the *sensomotoric cortex* is responsible for motor activities (Schandry, 2006) (see overview of functional regions in Figure 1), so if a specific area needs to be observed, then the electrodes have to be positioned over it.

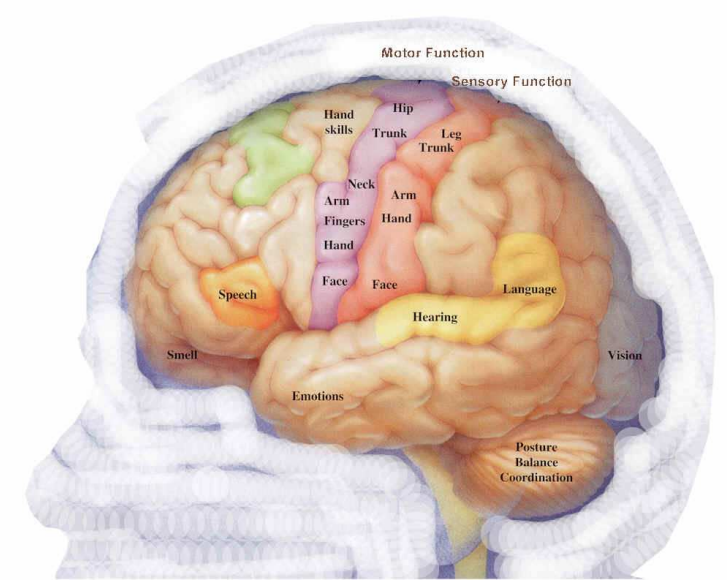

Figure 1: Functional regions of the human brain (University Hospitals of Cleveland, 2005)

As the human brain varies in shape and size, a relation-based system called the *10-20 System* was established to position the electrodes over these areas in a cohesive pattern. It became

internationally approved after it was described by the *International Federation Societies for Electroencephalography and Clincal Neurophysiology* (Klem, Luders et al., 1999). As mentioned before, the system is based on relative distances, so the distance between *nasion* (deepened area between nose and forehead) and *inion* (most prominent projection of the occipital bone at the lower rear part of the skull) is defined as 100% and divided into 10%-20%-20%-20%-20%-10% steps (Milnik, 2009). The space between the two *preaulicular points* (deepening in the ear in front of the auditory canal) is split in the same manner, so the resulting coordinates define the electrode positions (Figure 2). The naming of the electrodes is also standardized.

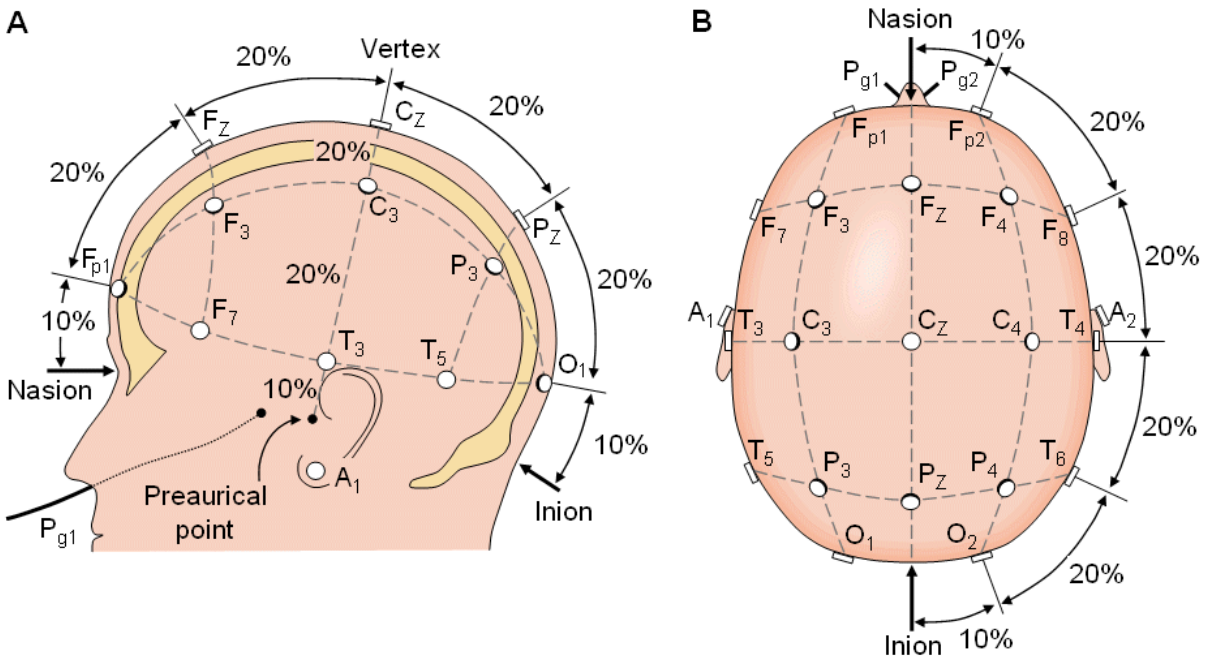

Figure 2: Definition of the electrode positions according the 10-20 system (Malmivuo e Plonsey, 1995)

For applications with higher spatial resolutions, the *10-10 system* was defined which is based on the 10-20 system. The difference is that one additional electrode is placed concentrically between two electrodes of the 10-20 system. Figure 3 shows the electrodes' positions corresponding to the 10-10 system.

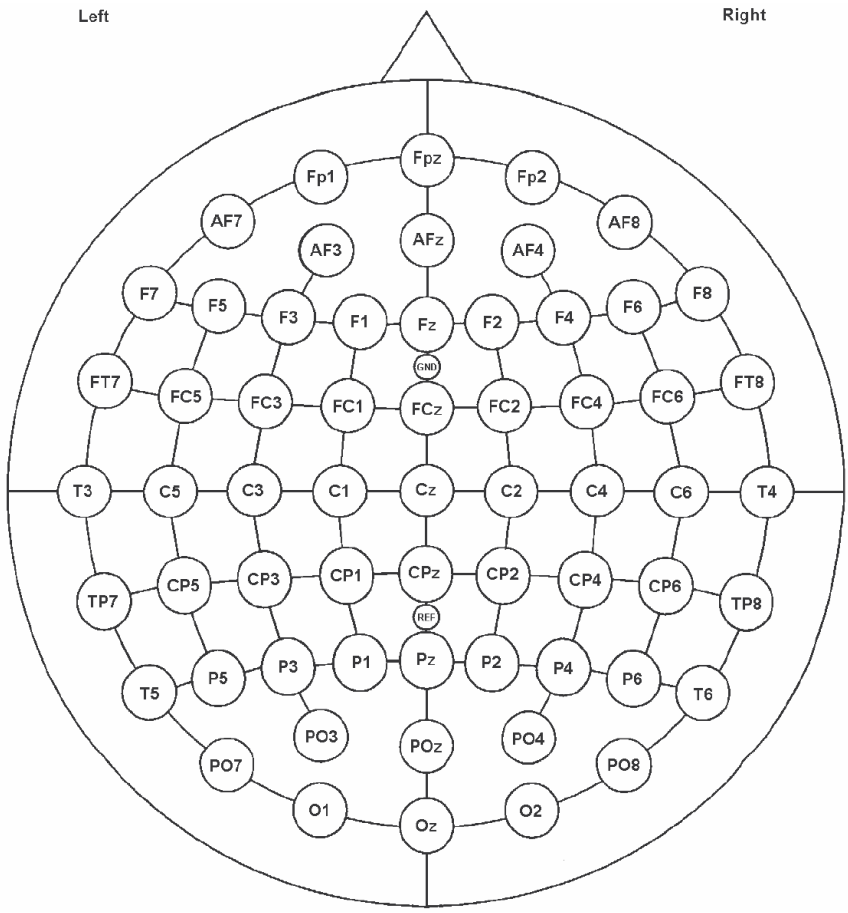

Figure 3: Top view of EEG electrode positions according the 10-10 system. The triangle on top of the circle indicates the nose (Micromed_S.P.A., 2009)

2.1.1 Reference Electrode

The EEG is the difference of the potential between two electrodes, whereas one electrode is defined as the reference with a potential of zero volt. The reference electrode is usually fixed (the usual position is the earlobe) and all remaining are related to it. Another possibility to specify the reference is the *bipolar* order, where one adjacent electrode is defined as the reference (Neudörfler, 2002). A mathematical method for the calculation of the reference point is the *Common Average Reference* (CAR). It is based on the calculation of a global mean value of all electrodes. A Further computational method is the Laplace derivation, where the mean value is subtracted from either 4 or 8 adjacent electrodes.

2.2 Types of EEG potentials

The brain activity can be evaluated by observing various phenomena in the EEG signal. These can be divided into 2 main parts (Schandry, 2006):

- Spontaneous EEG
- Evoked potentials

Additionally, the frequency range is divided into the following bands (Lytton, 2002):

- Delta: < 4Hz
- Theta: 4-8Hz
- Alpha: 8-13Hz
- Beta: 13-30Hz
- Gamma: > 30Hz

2.2.1 Spontaneous EEG

The *spontaneous EEG* is a result of stochastic voltage swings, depending on the physical state of the person at rest. The stochastic voltage variations are not correlated to stimulations, so the averaging over time equals nearly zero.

2.2.2 Evoked potentials

Evoked potentials can be observed by exposing the subject to a specified stimulus. The basic graduation is based on the way in which the stimulus is evoked (Niedermeyer, 2004):

- Visually evoked potentials (light flashes, pictures…)
- Auditory evoked potentials (sounds, clicks…)
- Somatosensory evoked potentials (tactile stimuli, …)
- Olfactory evoked potentials (smell)

A further distinction criteria of evoked potentials is if the EEG answer occurs phase locked to the stimulus. Phase locked potentials or *event related potentials* (ERP) can be filtered out of the spontaneous EEG signal by averaging over several trials. The so called *event-related EEG response* can occur in form of an amplitude decrease or increase directly after the stimulus, but not necessarily phase locked to the stimulation.
Evoked potentials and the possibility to detect them in an EEG signal are the basis for making brain computer interfaces (BCI) possible, which are described in detail in chapter 3.

3 Brain Computer Interfaces

A *Brain Computer Interface* (BCI) is a communication system which enables a person to control an electronic device only by means of brain activity (Wolpaw, Birbaumer *et al.*, 2002). The underlying measurement methods of the brain activity may vary. However, the most frequently used and reliable non-invasive method for BCI is EEG, followed by the rarely applied method fMRI. The latter is more usable for localization of active regions, based on predefined tasks on account of the excellent spatial resolution. The advantageous time resolution and mobility of the former method makes it not only useful for research, but also for explicit applications such as communication systems for individuals with locked-in syndrome. A further advantage of EEG based BCIs is the reduced complexity of signal processing methods to extract parameters for the generation of control signals. The further chapters explain the detailed principal function of BCI, and the basic EEG phenomena which can be used to realize BCI applications.

3.1 Functional parts of BCI

The main idea behind the BCI is to control a computer application by carrying out a specific mental task. The mental task is performed in a certain way, in order to evoke a defined brain activation phenomenon which can be categorized into different classes. Each class stands for a predefined control command of the application. The successful outcome of a control process is reached, if the intention of the user is properly recognized. Before a BCI can be used, the computer needs to generate specific parameters which allow the separation of the classes in an offline training phase. The following use of the BCI is performed online. Figure 4 shows the necessary steps to perform a BCI communication.

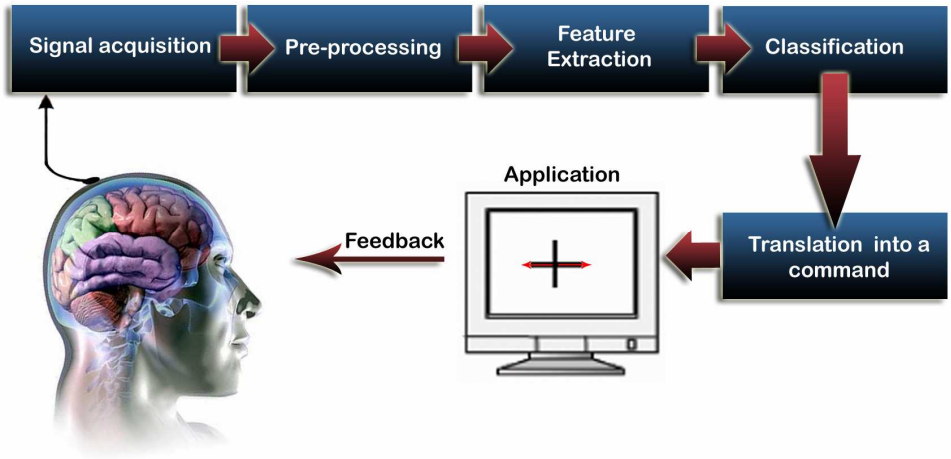

Figure 4: Functional Parts of a brain computer interface (Department of Biomedical Engineering Nitro Lab, 2010)

Signal acquisition:

Several methods such as fMRI or EEG can be used to obtain signals reflecting the brain activity of the user.

Pre-processing:

This step is necessary to remove artifacts and irrelevant data from the recorded signal.

Feature extraction:

The task of the feature extraction block is to analyze the signal within the response time and convert the observed data into certain parameters called *features*. With the help of these features, it is possible to describe the evoked potential analytically.

Classification:

Based on the extracted features, classification algorithms assign the measured signal to one of at least two classes.

Translation into a command:

After a successful classification, the application executes a command which is associated to the referred class.

Feedback:

At the end of the control process, the classification result (in terms of the execution of the command) is presented to the user on the screen.

3.2 Approaches for EEG based BCI

This chapter gives a short overview of EEG phenomena, which can be observed in the EEG signal and used for BCI applications.

3.2.1 Slow cortical potentials (SPC)

SPC's are slow, ramp shaped, potential drifts in the EEG. The signal drops slowly if the user prepares for a specific event. If the brain processes this event, the EEG signal rises again.

In a BCI application, the user learns by obtaining feedback to control the behaviour of the signal drifts. The signal drifts can be referred to defined commands like: on, off or left, right (Hinterberger, Schmidt *et al.*, 2004).

3.2.2 Visual Evoked Potentials and Steady-State Visual Evoked Potentials

As stated in chapter 2.2.2 (page 5), visual evoked potentials occur after visual stimulations.

If the stimulation frequency is beyond 2 Hz, the response is a characteristic curve or a so-called *transient visual evoked potential* (VEP). The relevant component (P300 component) is a positive response which occurs 300 ms after the stimulation. It rises if a certain event becomes more relevant for the user than others. VEP based BCI's use different flashing time points for several commands or symbols. If the P300 component is relevant enough at a defined time point, then the user's choice can be detected (Kaper, 2006).
If the stimulation frequency exceeds 6 Hz, the response occurs as multiples of the stimulation frequency. Such responses are referred to as *steady-state visual evoked potentials* (SSVEP).
SSVEP's can be used in BCI applications to code symbols with different flashing frequencies. The response frequency varies, depending on the user's symbol choice, so the intention of the user can be recognized (Farwell e Donchin, 1988).

3.2.3 Event-related synchronization/de-synchronization

The movement or the imagination of limb movement results in enhancement (*event-related synchronization, ERS*) or attenuation (*event-related de-synchronization, ERD*) of the EEG amplitude over the *sensomotoric cortex* of the brain (see Figure 5). The raised EEG amplitude indicates synchronized work of neurons and a low information processing. A consequent amplitude diminishment results in higher mental activity.

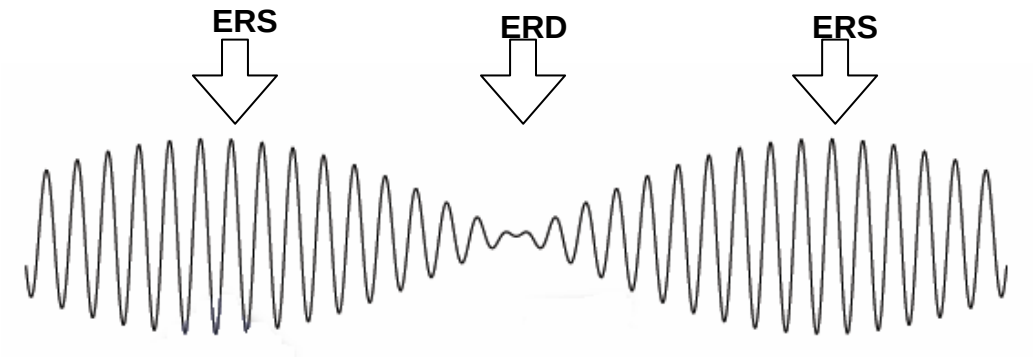

Figure 5: ERS: synchronized neuronal activity leads to EEG amplitude enhancement, and reduced information processing. ERD: de-synchronized neuronal work leads to EEG amplitude attenuation and higher information processing in the brain. Modified from (Laboratory of Brain-Computer Interfaces)

The phenomenon can be observed in two separate frequency areas:

- μ-Rhythm (7-13 Hz)
- β-Rhythm (18-30 Hz)

Depending on the imagined limb, the ERD/ERS arises at different positions on the sensomotoric cortex, so it can be discovered if the user is visualizing a limb movement and if so, it is possible to find out which is visualized (Pfurtscheller e Neuper, 2001), (Pfurtscheller, 2001).

3.3 g.tec Motor imagery BCI

The EEG based motor imagery BCI presented in this chapter is the basis for the exploration of quality and timing issues in combined EEG/fMRI BCI experiments in the course of this thesis. It relies on ERD/ERS potentials in the EEG and is split into two different phases. The first phase (training phase), serves to collect training data for the classifier. After the offline classification, the computer is able to give feedback online in the second phase (feedback phase) (Pfurtscheller e Neuper, 2001).

The experiment is based on the imagination of finger movements, which can be recognized by measuring the EEG signal over the sensomotoric cortex area. The BCI application displays arrows pointing to the right or left in a pseudo-random sequence (Figure 6). Afterwards, the test person concentrates on the imagination of finger movements of the corresponding hand. One trial lasts 8 seconds and one session takes 40 trials.

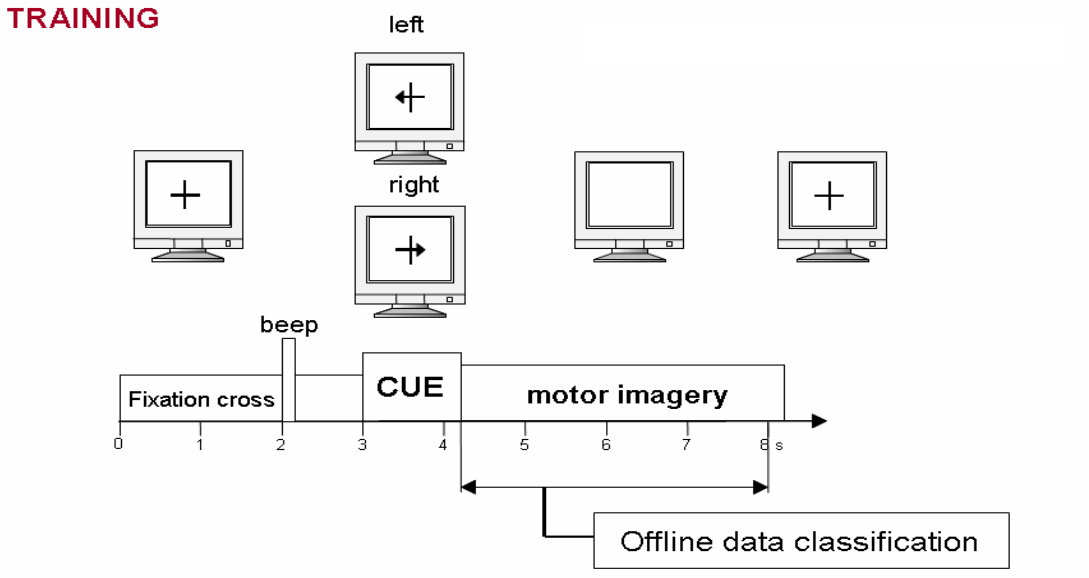

Figure 6: g.tec Motor imagery brain computer interface paradigm. Training phase (G.Tec-Medical-Engineering-Gmbh, 2009)

The classifier decides if the imagination corresponds to the proper arrow directions. The classification result is shown as an ascending beam in the classified direction, directly after the display of the arrow (see Figure 7).

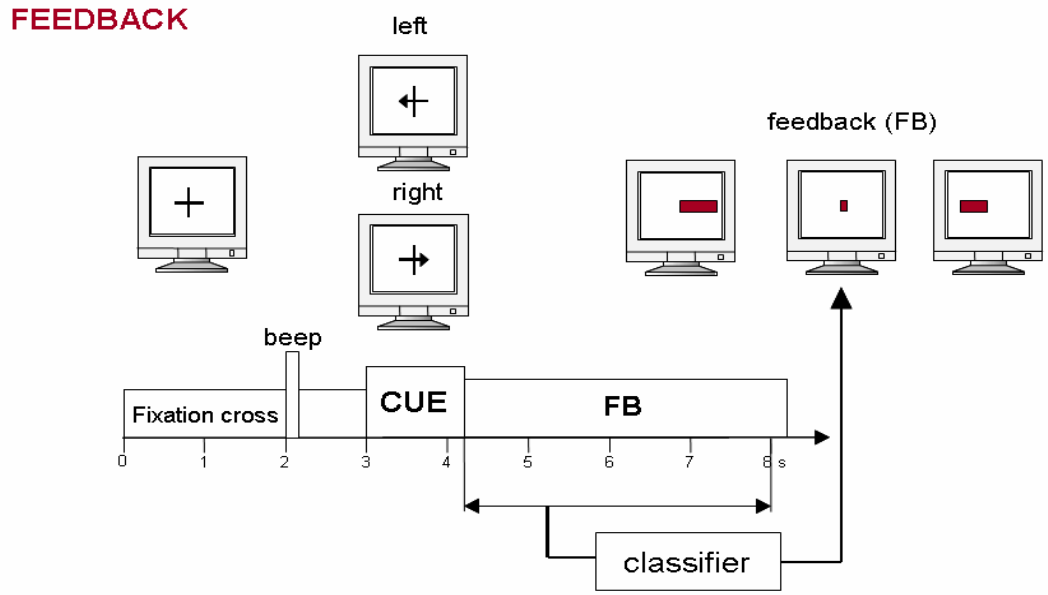

Figure 7: g.tec Motor imagery brain computer interface paradigm. Feedback phase (G.Tec-Medical-Engineering-Gmbh, 2009)

Figure 8 shows the Simulink model (MATLAB, 2003) of the BCI system. Below, an explanation of the BCI segments according to the overview in chapter 3.1 (page 6) can be found.

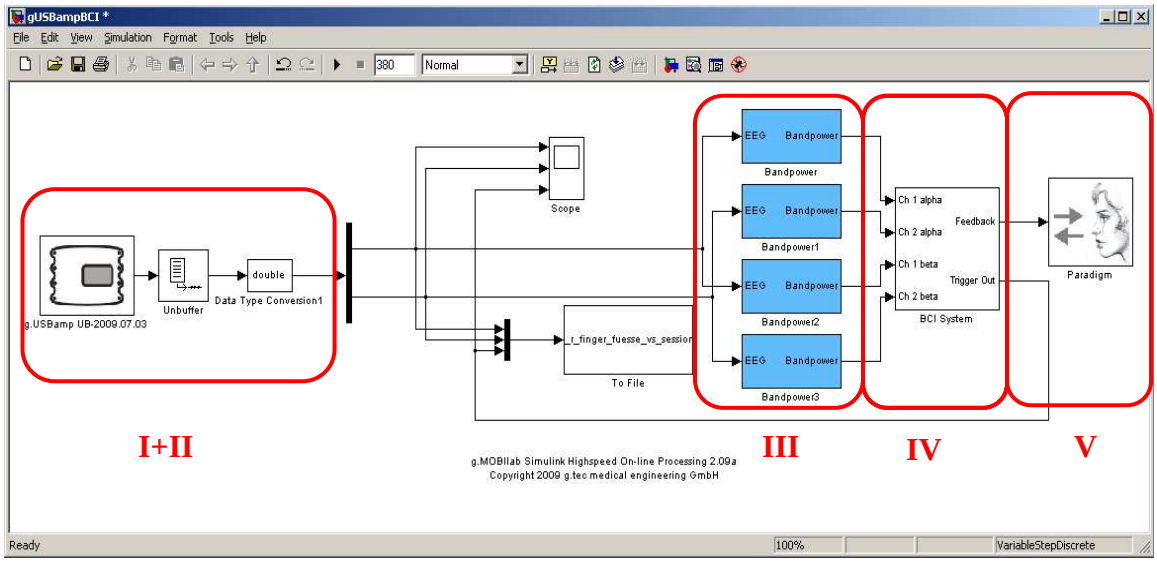

Figure 8: Simulink model of g.tec motor imagery brain computer interface

I Signal acquisition:

EEG is acquired using a 16 channel EEG amplifier (g.USBamp, g.tec medical engineering GmbH, Graz, Austria), with a sample frequency of 256 Hz. Impedance is kept below 5 kΩ with electrode gel. The channels FC3/C3 and FC4/C4 beyond the left and right motor cortex

are recorded in a bipolar manner to avoid movement artifacts. The paradigm is visualized in a Matlab figure.

II Pre-processing:

The acquired signal is band pass filtered with a butterworth 3rd order filter in the range of 0.5-30 Hz. An additional 50 Hz notch filter suppresses the power line frequency.

III Feature extraction:

As stated in chapter 3.2.3 (Page 8) ERS/ERD results in amplitude enhancements/attenuations depending on the mental activity. In order to represent this signal variation over time the band power is continuously calculated within a time window of one second for both ERS/ERD relevant frequency regions separately (see a Simulink Subsystem of the Bandpower block of Figure 8 in Figure 9).

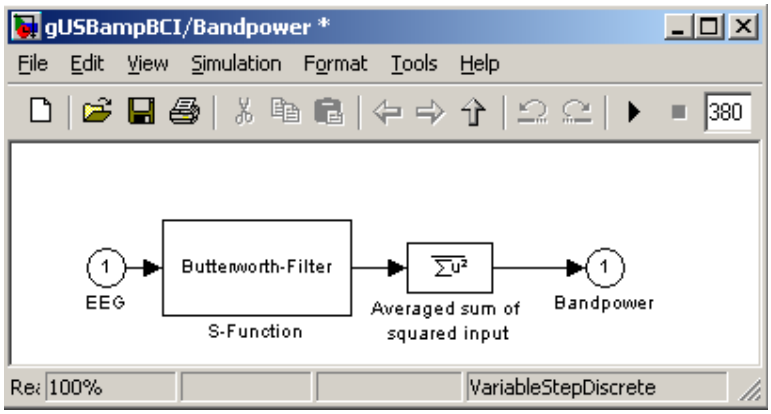

Figure 9: Bandpower block of g.tec Motor imagery BCI Simulink model

The ERS/ERD active frequency bands (chapter 3.2.3, page 8) are slightly different from individual to individual, so the analysis of so-called *time frequency maps* helps to redefine the regions and to get a priori information of the EEG signal quality.

Figure 10 shows an exemplary time-frequency map of a right index finger movement at the C3 electrode. The map resolves the EEG at the time point of finger movement in the frequency (y-direction) and time domain (x-direction). The ERS/ERD related amplitude enhancements/attenuations are colour-coded.

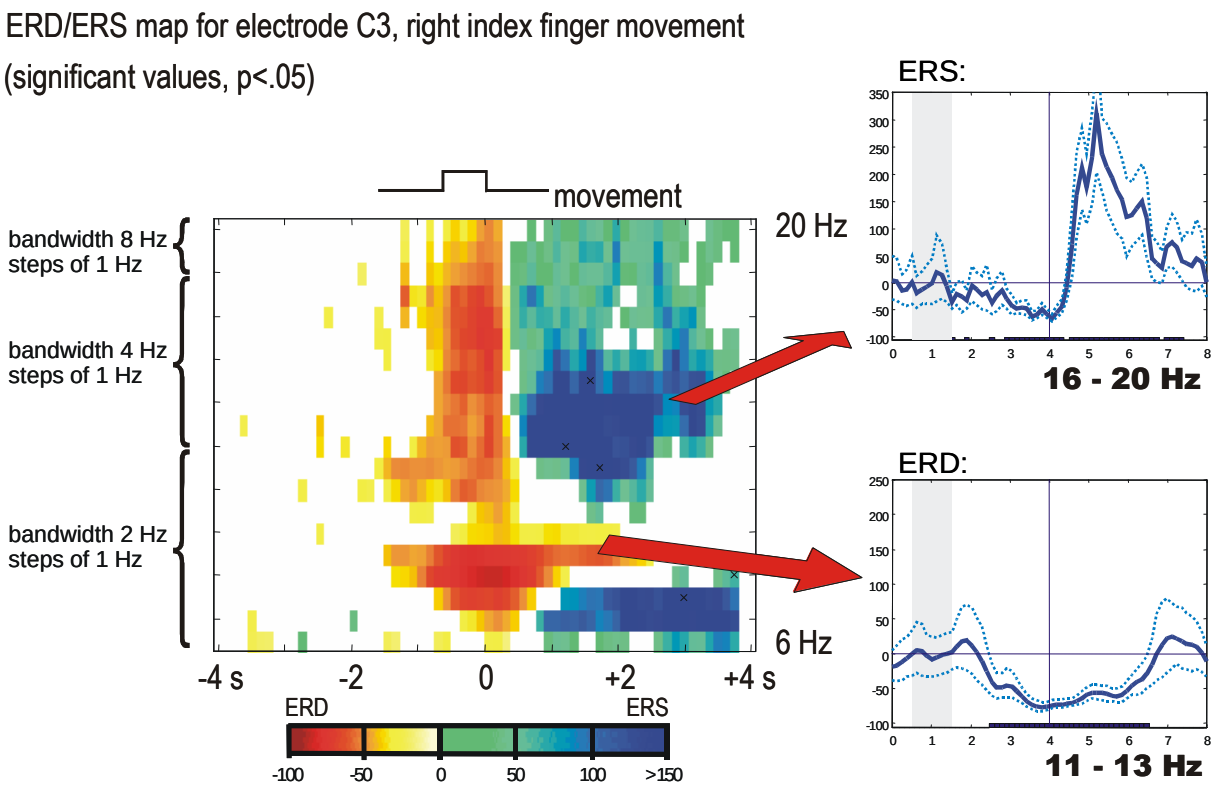

Figure 10: exemplary time-frequency map of a right index finger movement at the C3 electrode. ERS (blue)/ERD(red) (G.Tec-Medical-Engineering-Gmbh, 2009)

By calculation of time frequency maps of all EEG electrodes, the active brain areas during the stimulation can be observed. Such a map is visualized according the 10-10 system in Figure 11. The top figure shows the maps of right hand movement imagination trials, and the bottom figure the corresponding trials of the left hand imagination (160 trials, common average reference). What can be observed here is that after the imagination start of the right- and left hand respectively (red timeline), the activity in the brain occurs as ERD in the appropriate laterally reversed hemisphere. According to the ERD/ERS active frequency regions the band power filters are set.

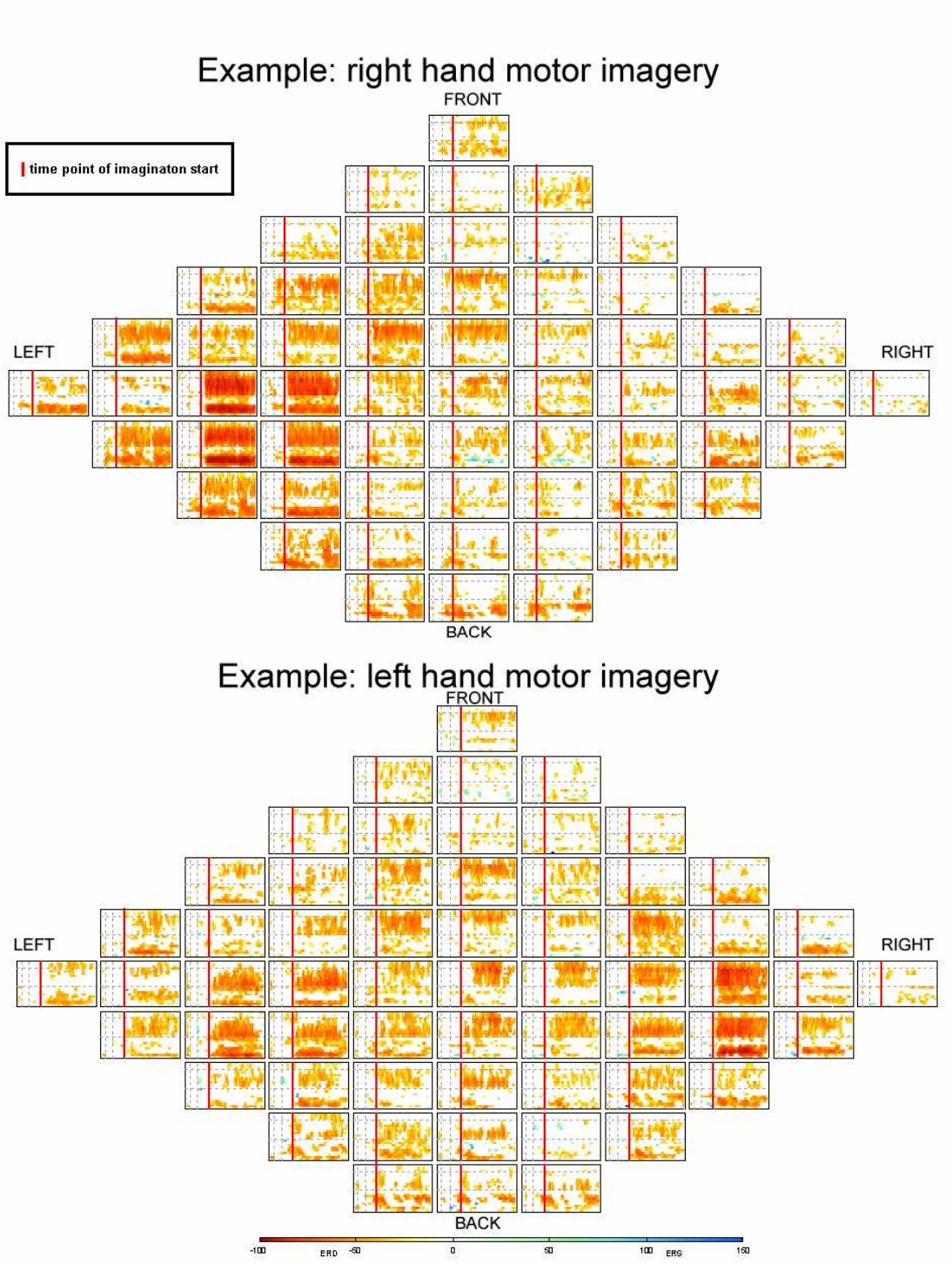

Figure 11: Time Frequency Maps of all EEG channels according the 10-10 system during a motor imagery BCI experiment. The red line indicates the imagination start point.
TOP: right hand movement imagination trials
BOTTOM: left hand movement imagination trials. (G.Tec-Medical-Engineering-Gmbh, 2009)

IV Classification:

After the training phase the data is classified offline with *Fisher's Linear Discriminant Analysis* (LDA) method (Duda, Hart *et al.*, 2000), using the program g.BSanyalyze (g.tec

medical engineering GmbH, Graz, Austria). The fundamental purpose of this method is to find a discriminant function $g(\vec{x})$ (3.1) which separates the recorded data (represented by different features) into two different classes.

$$g(\vec{x}) = \vec{w}^t X + b \tag{3.1}$$

$\vec{w}$ …weight vector

X …feature matrix

b …*bias*

For a binary classification problem the data which is represented by the feature matrix X is pointed to class one if $g(\vec{x}) > 0$ and class two if $g(\vec{x}) < 0$. The data representing feature matrix X consists of the band power values of all 40 trials of a session at equidistant time points (usually one second) within the trial period of 8 seconds. By following the known sequential order (in this case: 40 trials, 20 left and 20 right) of the arrow directions, the trials can be pooled together into 2 sub feature matrices $X_1 = \{\vec{x}_1^{C1}, ..., \vec{x}_{20}^{C1}\}$, $X_2 = \{\vec{x}_1^{C2}, ..., \vec{x}_{20}^{C2}\}$ according to the classes C1 and C2. The feature vectors $\vec{x}_1^{C1}, ..., \vec{x}_{20}^{C1}$ and $\vec{x}_1^{C2}, ..., \vec{x}_{20}^{C2}$ consist of the band power values within the ERD/ERS active frequencies for each class and EEG channel (C3, C4):

$$\begin{aligned}
\vec{x}_1^{C1} &= [BP_{1,C3,\mu-Rythm}^{C1}, BP_{1,C3,\beta-Rythm}^{C1}, BP_{1,C4,\mu-Rythm}^{C1}, BP_{1,C4,\beta-Rythm}^{C1}] \\
&\vdots \\
\vec{x}_{20}^{C1} &= [BP_{20,C3,\mu-Rythm}^{C1}, BP_{20,C3,\beta-Rythm}^{C1}, BP_{20,C4,\mu-Rythm}^{C1}, BP_{20,C4,\beta-Rythm}^{C1}]
\end{aligned} \tag{3.2}$$

$$\begin{aligned}
\vec{x}_1^{C2} &= [BP_{1,C3,\mu-Rythm}^{C2}, BP_{1,C3,\beta-Rythm}^{C2}, BP_{1,C4,\mu-Rythm}^{C2}, BP_{1,C4,\beta-Rythm}^{C2}] \\
&\vdots \\
\vec{x}_{20}^{C1} &= [BP_{20,C3,\mu-Rythm}^{C2}, BP_{20,C3,\beta-Rythm}^{C2}, BP_{20,C4,\mu-Rythm}^{C2}, BP_{20,C4,\beta-Rythm}^{C2}]
\end{aligned} \tag{3.3}$$

For a graphical 2 dimensional demonstration of the LDA procedure (Figure 12) two features per class (µ-rhythm at C3 and µ rhythm at C4) are used. The basic classification criteria is to define $\vec{w}$ so that the distance of the arithmetical averages m_1, m_2 of the feature values projected onto the discriminant function is a maximum, and the variance (elliptical circles in Figure 12) of each class should be a minimum.

$$m_1 = \frac{1}{N}\sum_{\vec{x}_1 \in C1} X_1, m_2 = \frac{1}{N}\sum_{\vec{x}_2 \in C2} X_2 \qquad , N = 20 \tag{3.4}$$

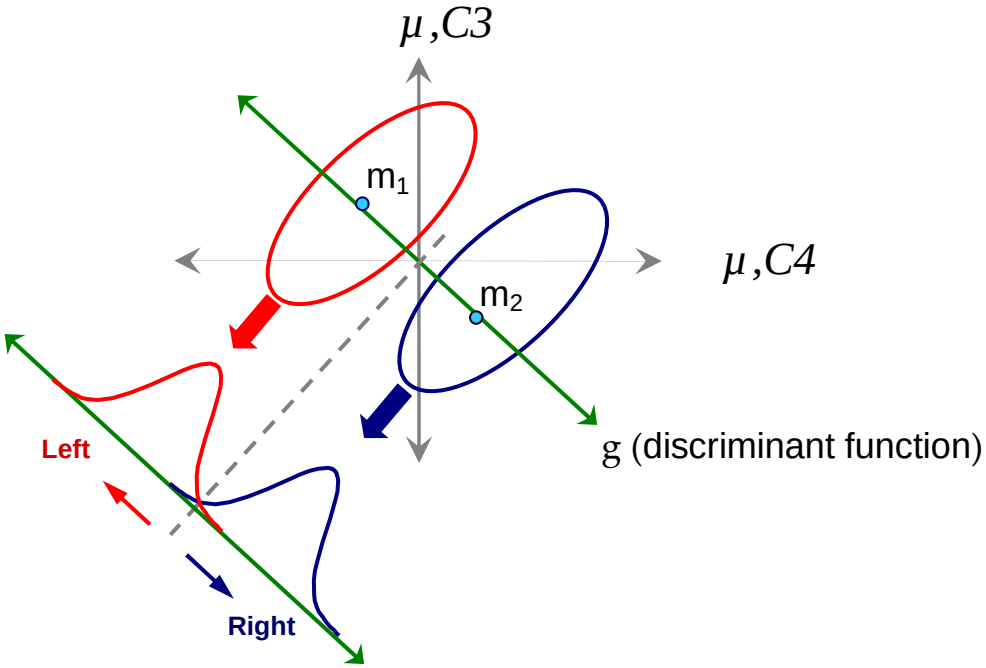

Figure 12: Illustration of the projection of the averaged feature matrices X_1, X_2 on the discriminant function g . The elliptical circles indicate the spread in values (Duda, Hart *et al.*, 2000)

Afterwards, the bias *b*, which indicates the distance of *g(x)* to the origin of the ordinates, is calculated. This procedure is repeated 8 times according to every second of the paradigm. The qualitative analysis of the resulting 8 weight vectors and bias values is proceeded by calculating the classification error using a *ten cross fold validation* (Ye, 2004). The weight vector and bias which lead to the lowest classification error are used for the online classification.

By means of this specific motor task the desired time course of the classification error can be defined (see Figure 13). Until the time point of imagination start (4.25 sec.) the classification error should be about 50 percent. This means that the observed data can't be classified neither to class 'left' nor class 'right'. Subsequently, during the imagination phase the classification error should fall to zero, which means that the classification works properly during the whole imagination phase. Based on empirical observations the drop of the error to at least 10 % or below can be considered as excellent result.

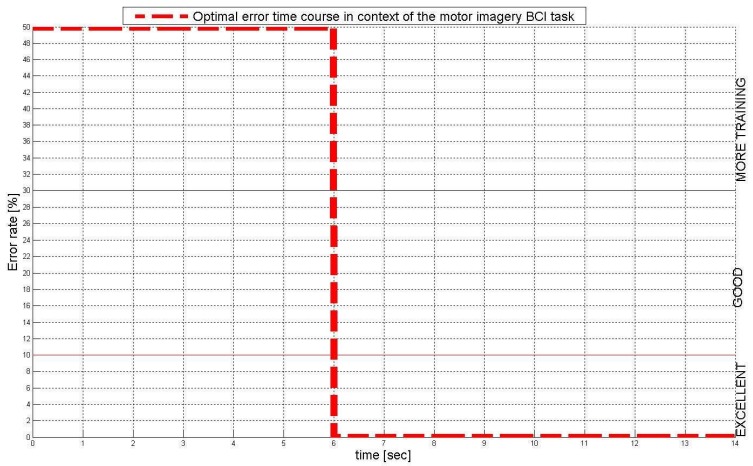

Figure 13 optimal time course of the classification error during the motor imagery task.

V Translation into a command and feedback:

After the offline classification the discriminant function $g(\vec{x})$(3.1) can be calculated in real-time and presented to the user graphically as feedback in the imagination phase of the paradigm. For this purpose the weight vector $\vec{w}$ and the bias b are loaded into the BCI System block (Figure 14), and calculated with the features according (3.1). The resulting function if visualized as a bar graph which points to left if $g(\vec{x}) < 0$ and right if $g(\vec{x}) > 0$. The amplitude of the bar graph is updated for every data sample and represents the decidedness of the classification.

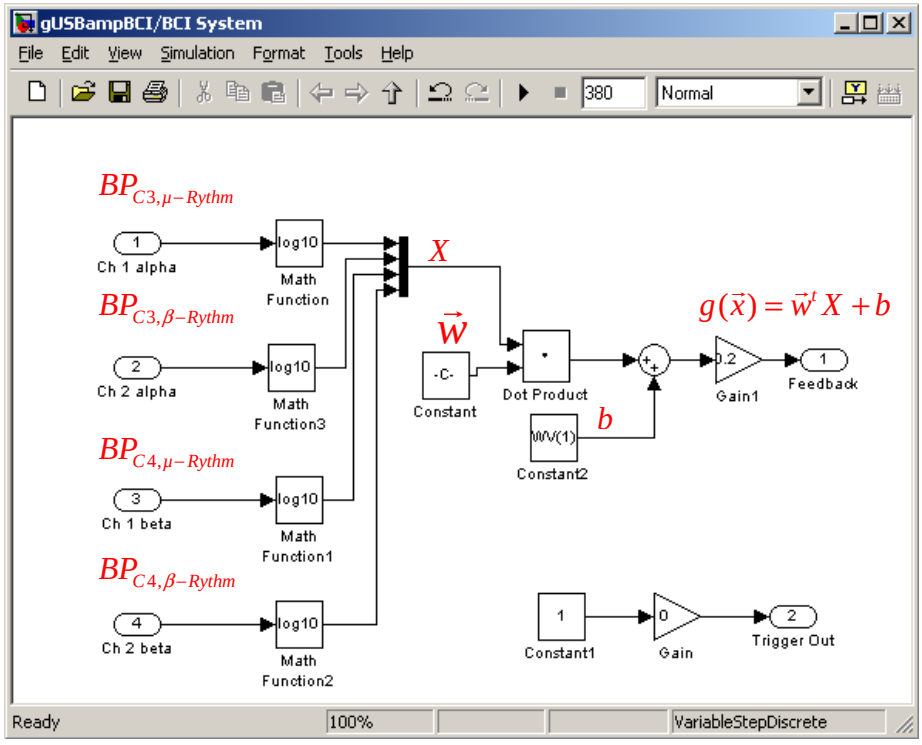

Figure 14: BCI System block of g.tec Motor imagery BCI Simulink model

4 Basics of functional Magnet Resonance Imaging (fMRI)

The functional examination of human brain activity by fMRI is based on a non-invasive imaging technique called *Magnetic Resonance Imaging (MRI)*. The basic principle is to utilize a physical feature of atomic nuclei called “nucleic spin”. Only nuclei with a spin cause weak magnetic fields which can be manipulated by magnets in order to make them measurable and spatially resolvable. The result is a stack of grey level images. The fact that makes MRI applicable for humans is that the hydrogen nucleus, which satisfies the above mentioned physical feature, is highly available in the human brain and body. The following description (see also Figure 15) is a short summary of the main components of a MR imaging machine and their tasks in the process of making MR images.

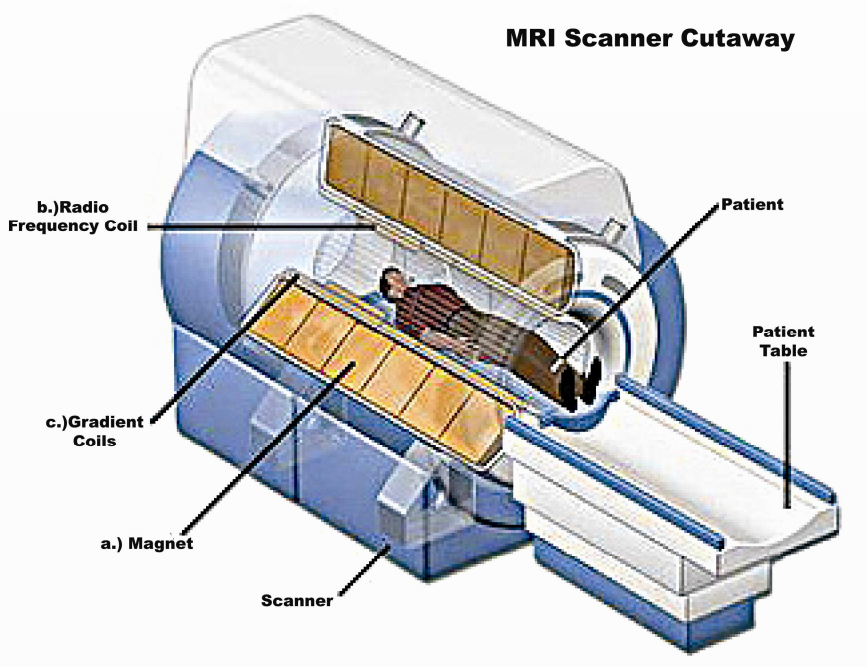

Figure 15: Main parts of a MRI scanner (Center-for-Integrating-Research-&-Learning, 2010)

a) A strong superconducting magnet creates a static magnetic field B_0 by polarizing the magnetic moments of the hydrogen nuclei. The resulting net magnetization is the basis for the MR signal. The magnet needs to be cooled down by a helium pump, which must constantly remain active to maintain super-conduction.

b) A radio frequency coil (*RF coil*) disturbs the magnetization of the nuclei by applying an RF pulse with a defined resonance frequency, which depends on the strength of the above mentioned static field. After the RF pulse has been applied, the magnetization returns to the primary direction and the nuclei emit the absorbed energy. Usually the same RF coil is used to pick up the emitted MR signal.

c) Before the MR signal can be picked up by the RF coil, it needs to be spatially encoded. For this, the slice images are divided into a matrix consisting of volume elements called voxels. The spatial association of the MR signal to voxel elements is carried out by three additional coils named *gradient coils*. All three are based on the principle that the resonance frequency of the net magnetization is dependant on the strength of the static field. The first coil (*Gss*) produces a gradient field along the direction of the static field B0 (z-coordinate). The superimposed field results in every slice having a different resonance frequency, which makes it possible to distinguish them in the frequency domain. The two remaining gradient coils resolve the MR signal into the x and y direction. The former makes sure that the voxel rows of a layer are distinguishable by phase shifts (G_{PE}), whereas the latter makes the voxels within a voxel row separable by means of frequency shifts (G_{FE}).

The received raw MR signal is digitally represented in the so called *k-space*. After a 2-dimensional Fourier transformation in x-y direction, the signal amplitude of the MR signal can be associated to spatial points.

The excellent contrast resolution of MR images can be used to make a phenomenon called *BOLD effect* (Blood Oxygen Level Dependency) visible which is indirectly connected to the functional brain activity, so the MR technique is relevant for functional analysis of the human brain. The BOLD effect is based on the assumption that externally stimulated areas of the brain induce a higher oxygenation level in the stimulated area. The para-magnetism of higher oxygenated blood diminishes over time, which affects the strength of the received MR signal and therewith the contrast level in the MR image. The difference in contrast to normal, non-oxygenated blood is approximately 15 %, and the time consumption of the BOLD answer is also limited.

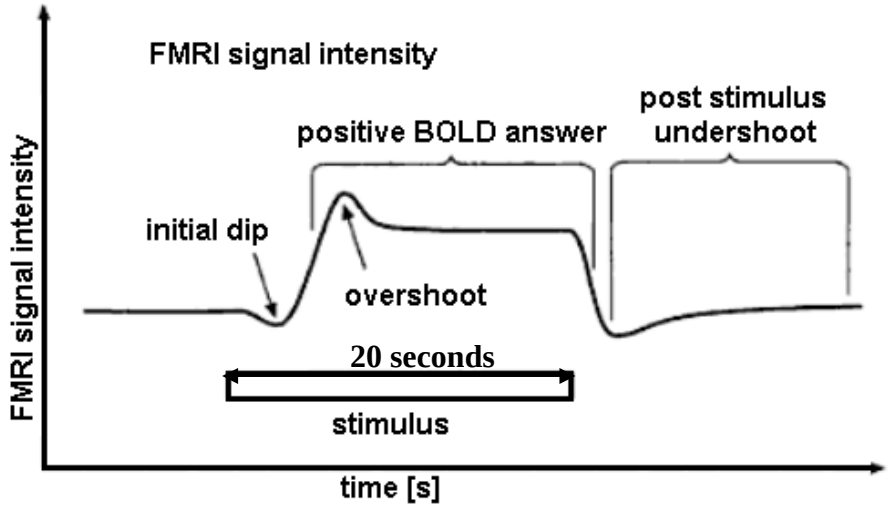

Figure 16: time course of the BOLD effect after a stimulation of 20 sec. Modified from (Walter, 2005)

Figure 16 shows the characteristic time course of the BOLD response after a stimulation of 20 seconds. The initial dip is followed by an overshot and a post-stimulus undershot. The time consumption (usually up to 15 sec.) needs to be taken into consideration in the stimulation process.

4.1 Echo Planar Imaging (EPI)

The BOLD answer results in contrast changes in the MR image and therefore the recording time of the stimulated area needs to be shorter than the BOLD answer itself. Consequently, an ultra fast imaging sequence called Echo Planar Imaging (EPI) is used, which allows to record all slices of a volume within the time of less than 3 second. The following table contains a list of important settings related to the recording of MR images:

- **TR Time:**
  Time duration to record all slices of a volume.
- **Number of Slices:**
  Number of layers of the observed volume.
- **Slice Thickness**
  The thickness of imaging slices in millimetres.
- **Slice Gap:**
  The not measured distance between the slices in millimetres. A lower gap can introduce more noise into adjoining slices.
- **TE Time:**
  The echo time (TE) represents the time in milliseconds between the application of the RF pulse and the peak of the received MR signal
- **Field of view (FOV):**
  The field of view is defined as the size of the two dimensional spatial encoding area of the image. It is defined in units of mm^2.
- **Matrix Size:**
  Two-dimensional number of volume elements within a MR image (for example: 64x64, 128x128…)

A sequence diagram, which shows the chronological switching order of the RF and the gradient coils, is depicted in Figure 17. Combined EEG/fMRI studies mostly suffer from the

superimposition of the resulting magnetic fields and the EEG signal. Chapter 5 (Page 25) explains the artifacts in detail and the possibilities to reduce them.

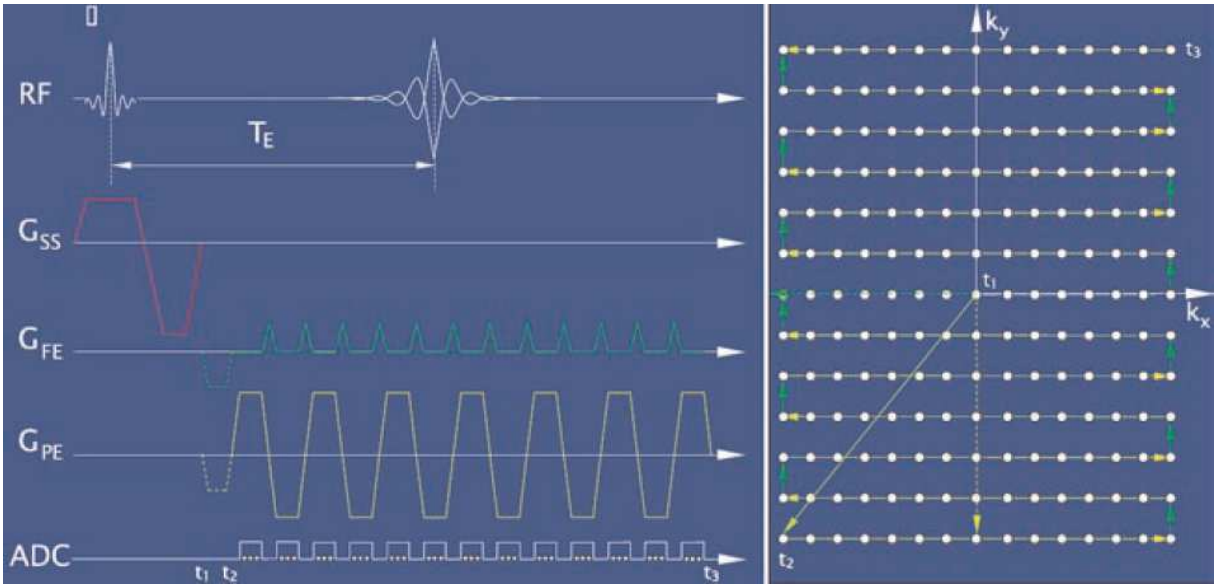

Figure 17: Sequence diagram of an EPI sequence and the representation in the k-space.(Scott H. Faro, 2010)

4.2 Statistical Parametric Mapping (SPM)

The principal approach of fMRI studies is to expose the test persons to sensory stimuli for a certain time period and compare the resulting activation of a brain region to resting phases or activations in other brain regions. The result is a spatial contrast difference in the fMRI images, depending on the predefined conditions. These contrasts can be visualized using the widely approved Matlab tool named SPM (*Statistical Parametric Mapping*) (Wellcome Department of Imaging Neuroscience, London; www.fil.ion.ucl.ac.uk/spm). Before the images can be statistically analyzed, a set of pre-processing steps has to be run through, which is summed up in the following sub chapters.

4.2.1 Data preparation

The fMRI images, which are available in the DICOM format, have to be converted into a proprietary format of SPM. Subsequently, the spatial zero point of all images is set at the *Commissura Anterior* (see Figure 18), so that the following normalization on a standardized brain map can be made efficiently.

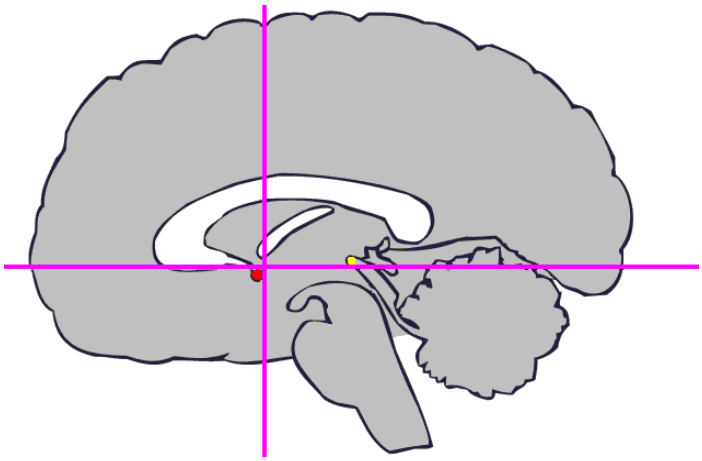

Figure 18: Illustration of the Commissura Anterior (red point), which is defined as the spatial zero point in fMRI scans (Mrc Cognitionand Brain Sciences Unit Cambridge, 2006)

4.2.2 Movement correction

The movements of the head in the course of the fMRI measurement are compensated by using the first image in a time series as reference. The subsequent movement correction is done by aligning the remaining images, so that the difference in brightness is minimized. The movements are represented by translational and rotational vectors, which indicate the relative deviation to the reference position in millimetres or degrees (see example in Figure 19). Based on this vector, test persons with too strong movements can be segregated.

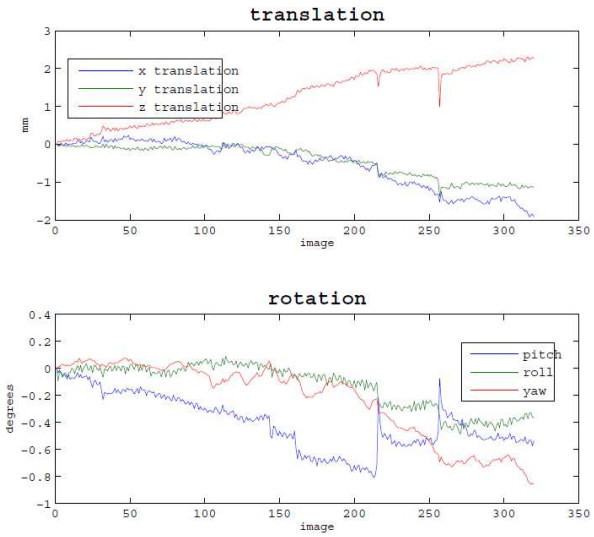

Figure 19: Example of a translational (top) and rotational (bottom) movement vector which indicates the deviation of the head position relative to a reference

4.2.3 Slice time acquisition correction

During the acquisition of a volume, the slices are recorded consecutively, which means that if the volume record lasts 3 seconds, then the last slice is acquired 3 sec. later than the first slice. In order to correct this time shift, the time series is transformed voxel-wise in the frequency

domain. The time difference is expressed as phase delay to a defined reference slice (usually the middle slice). The data is transformed back to the time domain after an interpolative correction of the phase delay.

4.2.4 Normalization

The normalization step is necessary to assign the stimulated regions to functional sections of the brain. Therefore the images are transformed into a standardized space (*MNI space*). The nonlinear transformation into this space allows the assignment of the functional activations to anatomical brain areas independent of individual brain anatomy.

4.2.5 Smoothing

In the final pre-processing step, a smoothing filter is used to flatten the signal and improve the signal to noise ratio.

4.2.6 Evaluation of results

After the pre-processing, the statistical model (design matrix) is built with the help of the experiment paradigm. Therefore the images are separated according to the conditions (for example: active phase to inactive phase), and the statistical significance of the greyscale differences is calculated. The underlying statistical method is a voxel-wise *t-/F-Test*, by which a univariate standard test for every voxel is carried out in order to calculate the significance of greyscale differences.

Figure 20 shows the paradigm of an exemplary finger tapping paradigm. At intervals of 40 seconds, the finger tapping of the right hand is alternated with resting phases. During every phase a set of 5 volume scans is acquired.

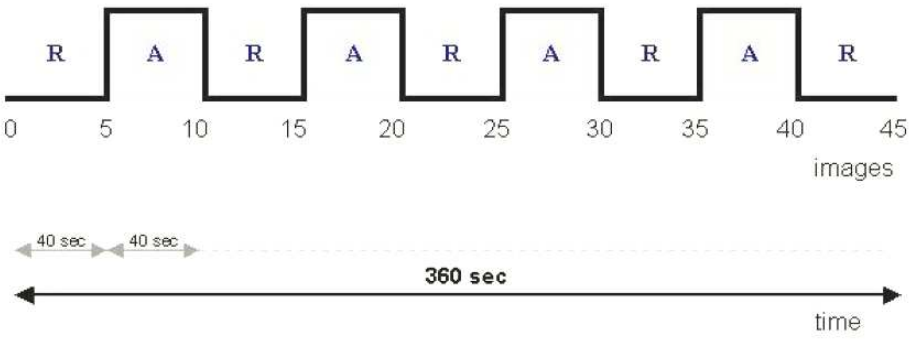

Figure 20 The paradigm of an exemplary finger tapping experiment. A→ Active finger tapping. R→ Resting phase

SPM assigns the scans according the paradigm by building a design matrix (see Figure 21 for the tapping example). The contrast vector defines the contrast level of the paradigm phases. A p-value table sums up the clusters which passed the significance test. The default p-value threshold is 0.001. The more significant the activation is the higher the contrast in the SPM glass brain. In the p-value table the coordinates of the activations in the MNI-space can be found.

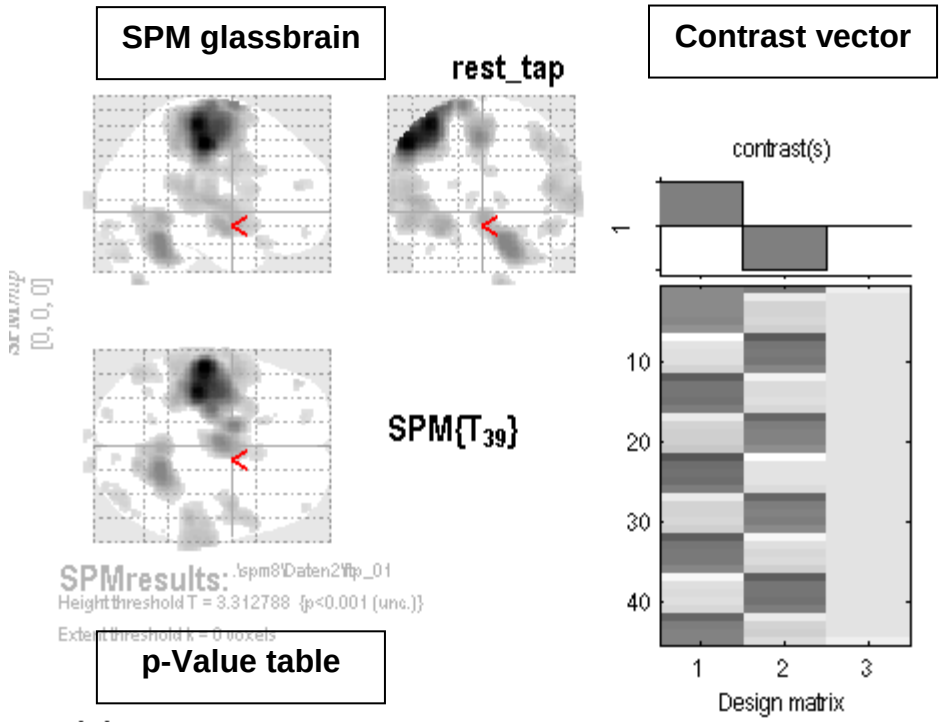

Statistics: *p-values adjusted for search volume*

set-level		cluster-level				peak-level					mm mm mm		
p	c	$p_{FWE-corr}$	$q_{FDR-corr}$	k_E	p_{uncorr}	$p_{FWE-corr}$	$q_{FDR-corr}$	T	(Z=)	p_{uncorr}			
0.000	24	0.000	0.000	11300	0.000	0.000	0.000	16.05	Inf	0.000	-56	-20	50
						0.000	0.000	15.45	Inf	0.000	-38	-26	62
						0.000	0.000	11.96	7.71	0.000	-38	-10	60
		0.000	0.000	1909	0.000	0.000	0.000	8.43	6.32	0.000	16	-54	-18
						0.000	0.000	8.35	6.29	0.000	22	-50	-26
						0.004	0.003	6.38	5.25	0.000	2	-52	-4
		0.000	0.000	1851	0.000	0.035	0.020	5.55	4.73	0.000	50	-30	18
						0.087	0.043	5.19	4.50	0.000	68	-18	14
						0.108	0.046	5.11	4.44	0.000	66	-24	8
		0.079	0.052	270	0.011	0.087	0.043	5.19	4.50	0.000	42	0	48
		0.552	0.320	94	0.107	0.098	0.044	5.15	4.47	0.000	14	-68	-48
		0.107	0.060	241	0.015	0.287	0.098	4.68	4.15	0.000	-52	-66	-2
						0.890	0.450	3.90	3.56	0.000	-50	-56	-4
		0.066	0.052	287	0.009	0.314	0.105	4.64	4.12	0.000	50	10	-10
						0.551	0.200	4.33	3.89	0.000	50	-2	-8
		0.966	0.676	20	0.450	0.590	0.218	4.29	3.86	0.000	-46	48	18
		0.171	0.086	199	0.025	0.689	0.275	4.17	3.77	0.000	38	-80	-32
						0.987	0.654	3.59	3.31	0.000	30	-92	-10
						0.999	0.905	3.39	3.15	0.001	28	-84	-20

Figure 21: Illustration of the SPM results. The design matrix (top left) assigns the volume scans to the paradigm. The contrast vector defines the contrast difference between the paradigm phases. The p-value sums up the significant clusters and their coordinates, which are colour coded accordingly, and visualized in the SPM glass brain. The largest cluster is marked green.

These coordinates (see Figure 22) can be labelled to anatomical atlases by additional SPM toolboxes. For the presented thesis the toolbox AAL (*automated anatomical labelling*, GIP

CYCERON,Caen http://www.cyceron.fr) was used. It maps the activations to the *Talairach* atlas.

Labels : *volume summary (labels and distances for entire volume)*

x,y,z mm	label	dist mm					
-56 -20 50	Parietal_Inf_L	0.00	Postcentral_L	2.00	SupraMarginal_L	8.00
-38 -26 62	Precentral_L	0.00	Postcentral_L	2.83	Parietal_Inf_L	15.62
-38 -10 60	Precentral_L	0.00	Postcentral_L	7.48	Frontal_Sup_L	8.72
16 -54 -18	Cerebelum_4_5_R	0.00	Cerebelum_6_R	2.83	Fusiform_R	5.66
22 -50 -26	Cerebelum_6_R	0.00	Cerebelum_4_5_R	2.00	Fusiform_R	8.94
2 -52 -4	Vermis_4_5	0.00	Cerebelum_4_5_L	6.00	Cerebelum_4_5_R	6.00
50 -30 18	Temporal_Sup_R	0.00	Rolandic_Oper_R	2.00	SupraMarginal_R	4.47
58 -18 14	Temporal_Sup_R	0.00	Rolandic_Oper_R	2.00	Postcentral_R	2.00
66 -24 8	Temporal_Sup_R	0.00	Rolandic_Oper_R	8.25	Temporal_Mid_R	10.00
42 0 48	Precentral_R	0.00	Frontal_Mid_R	4.00	Frontal_Sup_R	12.33
14 -68 -48	Cerebelum_8_R	0.00	Cerebelum_7b_R	7.21	Cerebelum_9_R	7.48
-52 -66 -2	Temporal_Mid_L	0.00	Occipital_Mid_L	2.00	Occipital_Inf_L	2.83
-50 -56 -4	Temporal_Mid_L	0.00	Temporal_Inf_L	2.00	Occipital_Inf_L	9.80
50 10 -10	Insula_R	2.00	Temporal_Pole_Sup_R	2.00	Temporal_Sup_R	8.00
50 -2 -8	Temporal_Sup_R	0.00	Insula_R	2.83	Temporal_Pole_Sup_R	8.83
-46 48 18	Frontal_Mid_L	0.00	Frontal_Inf_Tri_L	4.47	Frontal_Sup_L	18.22
38 -80 -32	Cerebelum_Crus1_R	0.00	Cerebelum_Crus2_R	6.00	Cerebelum_6_R	11.49
30 -92 -10	Occipital_Inf_R	0.00	Lingual_R	4.00	Fusiform_R	6.00
28 -84 -20	Cerebelum_Crus1_R	0.00	Cerebelum_6_R	2.83	Lingual_R	2.83
4 -12 -12	Thalamus_R	10.00	Hippocampus_R	11.49	Thalamus_L	11.66
-6 -16 -10	Thalamus_L	8.00	Hippocampus_L	11.49	Thalamus_R	12.81
-16 20 -20	Frontal_Sup_Orb_L	0.00	Frontal_Inf_Orb_L	2.00	Rectus_L	4.47
-22 -90 -8	Occipital_Inf_L	0.00	Fusiform_L	3.46	Occipital_Mid_L	4.00
6 18 30	Cingulum_Mid_R	0.00	Cingulum_Ant_R	2.00	Cingulum_Mid_L	5.66
14 -102 10	Cuneus_R	0.00	Occipital_Sup_R	4.90	Calcarine_R	6.00
44 54 -14	Frontal_Mid_Orb_R	0.00	Frontal_Inf_Orb_R	4.90	Frontal_Mid_R	13.42
48 -72 4	Temporal_Mid_R	0.00	Occipital_Mid_R	2.00	Occipital_Inf_R	6.63
8 -84 -10	Lingual_R	0.00	Cerebelum_6_R	4.00	Calcarine_L	4.90
-46 -46 -12	Temporal_Inf_L	0.00	Temporal_Mid_L	5.66	Fusiform_L	6.00
-6 -104 10	Occipital_Sup_L	0.00	Cuneus_L	3.46	Calcarine_L	4.47
-22 54 2	Frontal_Sup_L	0.00	Frontal_Mid_L	2.00	Frontal_Sup_Medial	10.00
-38 -60 -26	Cerebelum_6_L	0.00	Cerebelum_Crus1_L	2.00	Fusiform_L	4.00
-20 -58 -18	Cerebelum_6_L	0.00	Cerebelum_4_5_L	4.00	Fusiform_L	4.47
60 -50 -8	Temporal_Mid_R	0.00	Temporal_Inf_R	2.00	Occipital_Inf_R	17.20
-22 32 -22	Frontal_Mid_Orb_L	0.00	Frontal_Sup_Orb_L	2.83	Frontal_Inf_Orb_L	4.00

Figure 22 Table of anatomical labels of the activation clusters. The biggest cluster is marked red.

The visual presentation of the results can also be carried out by the projection of the activated regions on a standardized three dimensional brain sample, or by projections on optionally recorded high resolution MR images of the observed brain. In Figure 23, the activation of the left motor cortex, according to the above mentioned tapping experiment is illustrated.

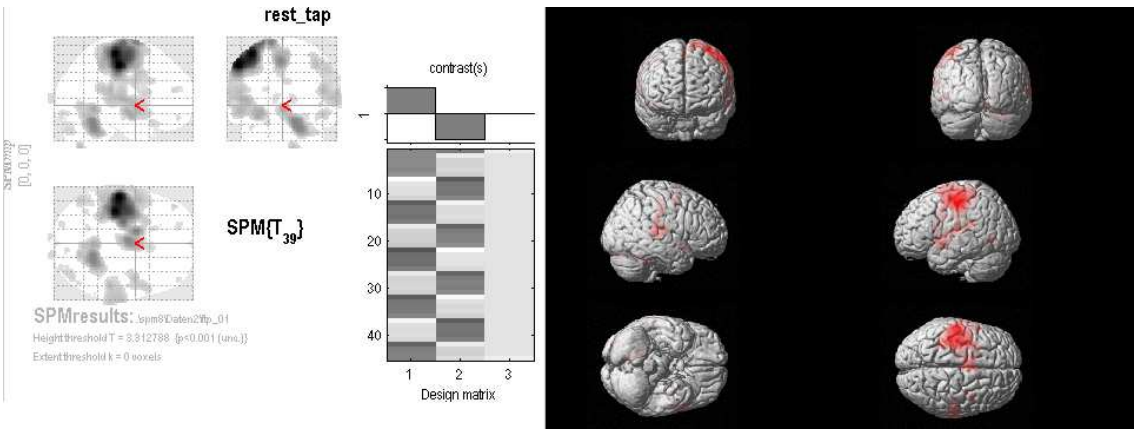

Figure 23: Activation of the left motor cortex according the exemplary tapping experiment

5 Overview of MRI-related EEG artifacts and corresponding suppression methods

This chapter summarizes EEG artifacts during combined EEG/fMRI recordings, together with hardware, software, and organizing aspects for artifact reduction.

5.1 Image Acquisition Artifact

The first big challenges in building MRI safe EEG hardware were to predict the saturation of EEG amplifiers, resulting from the induction of magnetic fields during the image acquisition, and to guarantee patient safety (Lazeyras, Zimine *et al.*, 2001). Therefore most hardware considerations are based on the reduction of magnetic coupling, starting at the EEG electrodes. The usually ring-shaped electrodes are arranged as rings with a slit to reduce eddy currents. The electrode material is nonmagnetic and in most cases chloride coated silver. To ensure sufficient patient safety and comfort, the electrodes are not placed directly on the head surface (Lemieux, Allen *et al.*, 1999). A special electrode gel provides a conductive connection between head and electrode and ensures reduced artifacts in the fMRI images in comparison to ordinary gel. Connecting the electrodes to the EEG amplifier with twisted laces results in better noise immunity (Matsuda, Matsuura *et al.*, 2002) (Goldman, Stern *et al.*, 2000). The amplifier itself is battery-driven, and shielded with nonmagnetic material. Using fibre optic cable to transfer the EEG data out of the MR room ensures galvanic decoupling.
Despite of all the hardware measures, the superimposed artifacts are still hundreds of times larger than the EEG signal. However the periodicity of the artifact allows suppressing the disturbances with relatively simple filtering methods. The following chapter contains the fundamental characteristics of the imaging artifact, which are needed in order to understand the methodical aspects of the filtering procedures in the subsequent chapters.

5.2 Characteristics of the Imaging artifact

The EEG of a phantom record in Figure 24 shows the typical imaging artifact of an EPI sequence. The sample frequency of the EEG amplifier is f_s=1024 Hz. The repetition time TR (see chapter 4.1, page 19) is 3 sec. and the number of slices is 24. A comparison with the EPI Sequence timing diagram shown in chapter 4.1 (Page 19) indicates the influences of the components of an MRI machine. The timing-related parameters (for example: phase shifts relative to the EEG) are the same across all channels, but amplitude deflection varies and is in the range of a few millivolt.

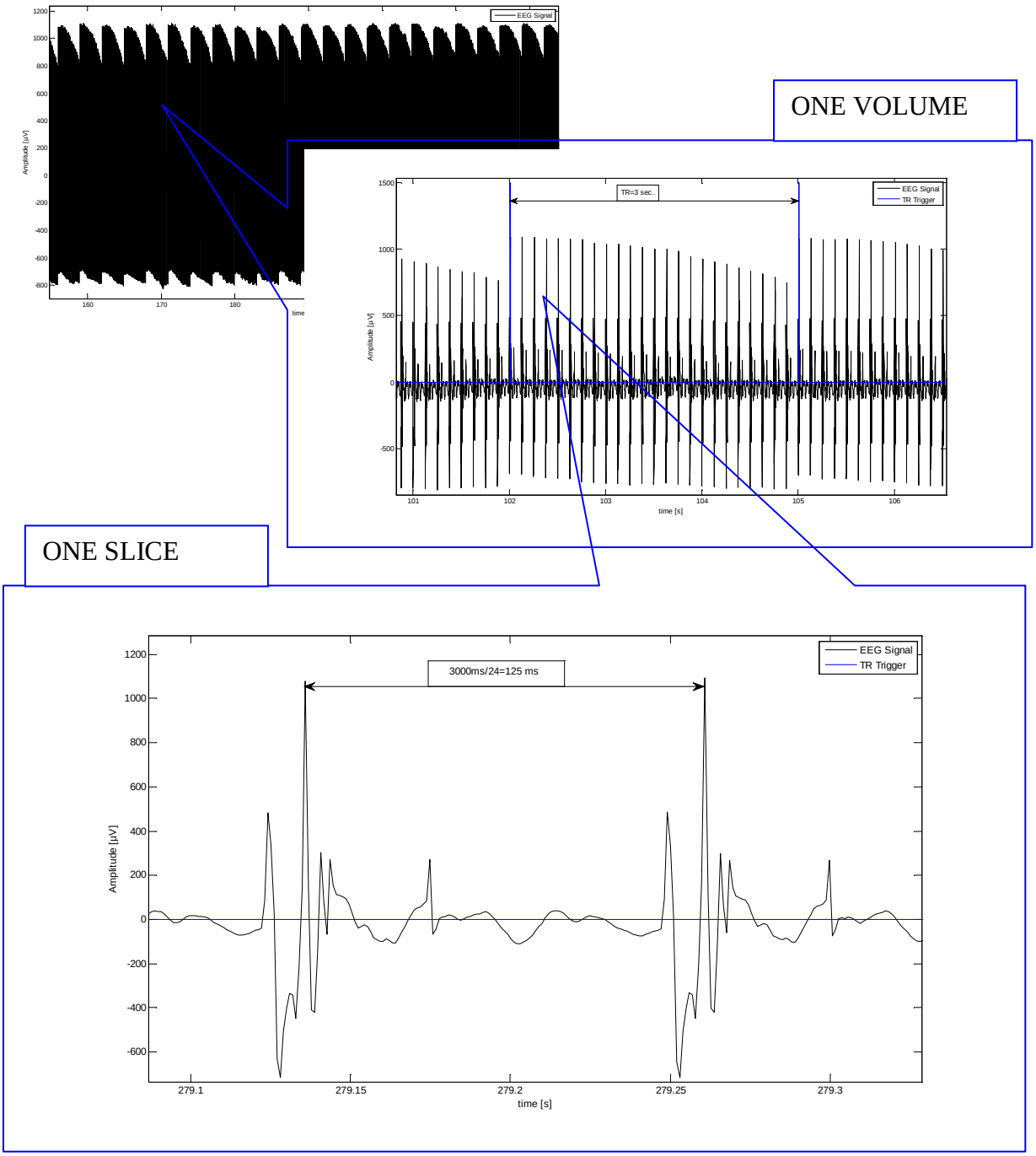

Figure 24: Time course of the imaging artifact contamined EEG signal, sample frequency fs = 1024 Hz, TR=3 sec., number of slices = 24

The influence of the imaging artifact in the frequency domain is noticeable in the form of spectral lines with a multiple of the fundamental frequency which is dependent on the following MRI settings:

$$f1 = \frac{Number \quad o\, f \quad Slices}{TR} = \frac{24}{3s} = 8Hz \tag{5.1}$$

Further spectral lines occur n times the reciprocal of the TR time:

$$f1,n = \frac{Number \quad o\,f \quad Slices}{TR} \pm n \cdot \frac{1}{TR} = \frac{24}{3s} \pm \frac{1}{3s} = 8Hz \pm n \cdot 0,33Hz \qquad (5.2)$$

Thus the skillful adjustment of TR time and the number of slices can prevent the appearance of the artifact in the used signal frequency range of the EEG. A further timing aspect arises trough the well documented asynchrony problem between the system clocks of the MR scanner and the EEG amplifier (Garreffa, Carnì *et al.*, 2003). If the timing of the sampling time points is not synchronized, than the superimposed imaging artifact starts jittering (see Figure 25) temporally, which results in displacements of the sampling time points. The sampling time points of the first slice of volume one, differ from the time points of slice one of the third volume.

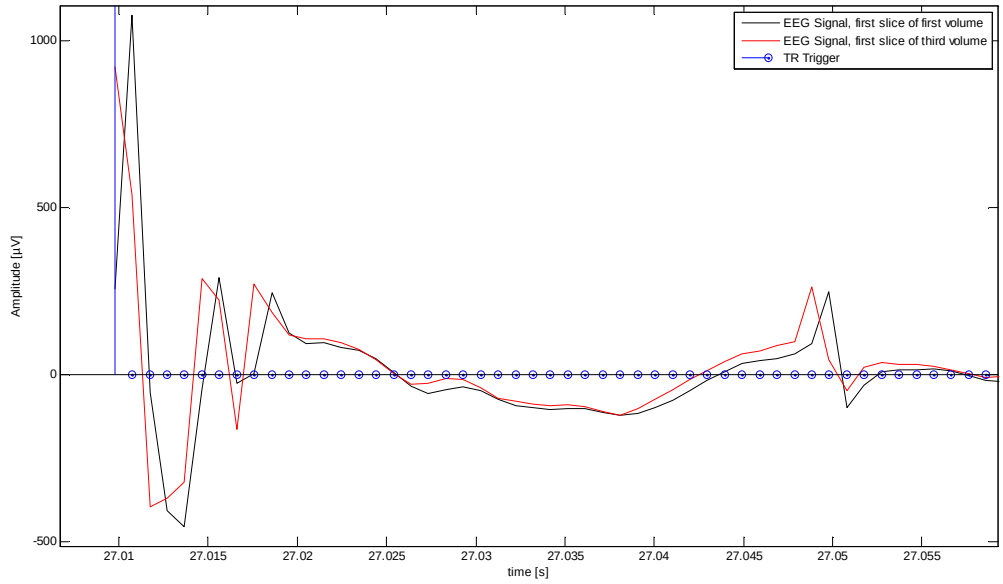

Figure 25: Illustration of the jittering effect, if the system clocks of MRI scanner and EEG amplifier are not synchronized

The jitter of the imaging artifact hampers the filtering processes, because all filter algorithms assume a periodical imaging artifact. The asynchrony of the system clocks can be suppressed to a certain extent by setting the above mentioned fundamental frequency so that the peaks occur at integer multiples of sample time points of the EEG amplifier. As a result the slice artifacts within a TR period still jitter, but the jitter is nearly constant over several TR periods, so a periodic artifact can be assumed (see details in chapter 6.3.1.1, page 40).

A hardware based method (Mandelkow, Halder *et al.*, 2006) solves the asynchrony problem by dividing the MR system clock frequency with frequency dividers, and using it as sampling

frequency for the EEG amplifier. The phase shift of the clocks is reduced with a phase-locked loop (PLL). This approach proves to be very efficient and thus ensures a relatively simple and effective filtering of the imaging artifact up to the gamma band.

5.3 Imaging Artifact filtering methods

This chapter gives a general overview of the current filtering methods for the correction of image artifacts. This overview is given without a qualitative comparison, because the test conditions and data are only comparable to a certain extent. Most of the filtering methods can be divided into the following filtering steps (Figure 26):

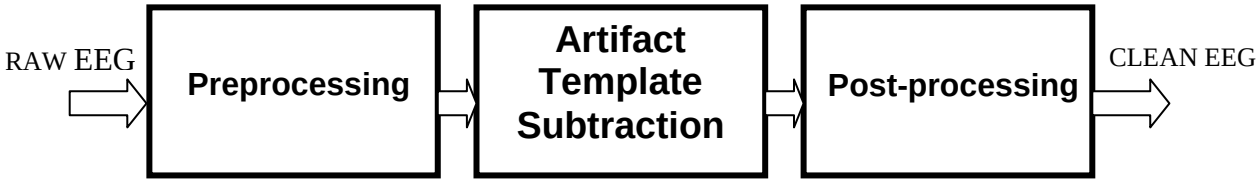

Figure 26: Overview of filtering steps of most imaging artifact filtering methods

First, the pre-processing step consists of frequency band limitations and averaging filters for offset and signal drift removal.

Secondly, the Artifact Template Subtraction step is applied to reduce most of the imaging artifact. The basic approach relies on two different assumptions. The first assumption is that the raw signal *x(t)* consists of the following three uncorrelated components (Garreffa, Carnì *et al.*, 2003):

$$x(t) = eeg(t) + n(t) + imga(t) \tag{5.3}$$

The EEG signal *eeg(t)*, the instrumental noise *n(t)*, and the imaging artifact *imga(t)*. The second assumption starts from the premise that if a periodic signal fragment with the length of *N* samples is arithmetically averaged *M* times, then all components except the imaging artifact become zero:

$$x_i = [x_{i,1} .... x_{i,N}] = eeg_i(t) + n_i(t) + imga_i(t), \qquad i = 1...M \,, N = TR \cdot fs \tag{5.4}$$

$$x_{avg}(t) = \frac{1}{M}\sum_{i=1}^{M} x_i(t) = \frac{1}{M}\sum_{i=1}^{M} eeg_i(t) + \frac{1}{M}\sum_{i=1}^{M} n_i(t) + \frac{1}{M}\sum_{i=1}^{M} imga_i(t) \tag{5.5}$$

$$x_{avg}(t) = eeg_{avg}(t) + n_{avg}(t) + imga_{avg}(t) \tag{5.6}$$

After M averages:

$$eeg_{avg}(t) \to 0, n_{avg}(t) \to 0\,, x_{avg}(t) \cong imga_{avg}(t) \tag{5.7}$$

The clean EEG is received after the periodical subtraction of the mean imaging artifact $imga_{avg}(t)$ from *x(t)*. One time period is usually a TR time, which is denoted as one *epoch*.

Finally, due to the limited efficiency of the artifact template subtraction (Allen e P., 2000), several post-processing steps for Residual Artifact Correction are necessary. For a better overview, the following filtering methods are subdivided into the three filtering steps shown in Figure 26.

5.3.1 AAS Method

The foundation of fMRI-related artifact correction was laid by Allen et al. (Allen e P., 2000) with the so called *Average Artifact Subtraction Method* (AAS), which was used as a basis for several other approaches. Therefore the following text contains a more detailed explanation of the abovementioned filtering steps (Figure 26) in this method, and the further method explanations contain just the differences in relation to the AAS method.

5.3.1.1 Pre-processing

The resting EEG of 5 subjects, recorded with a sampling frequency of 5 KHz, was cut off with a 70 Hz low pass filter. Additionally, a *TR trigger* was recorded, which indicates the start of a new volume acquisition by a short TTL impulse.

5.3.1.2 Artifact Template Subtraction (ATS)

For the artifact template subtraction step, 25 epochs were found to be sufficient in order to remove the EEG from the artifact template, where the first 5 epochs were used by default. Every further epoch would have been added if the cross-correlation factor between the artifact at hand and the template had exceeded the value of 0.975. The epochs were interpolated with a 25 coefficient FIR representation of a sinc function before the averaging step, in order to minimize the phase shift between artifact and TR trigger. After the averaging, the interpolation was carried out in the opposite direction in order to adapt the mean signal to the raw input signal.

5.3.1.3 Post-processing for Residual Artifact Correction

After the ATS, the EEG signal and the TR trigger were smoothed with an 80 Hz low pass filter, and down-sampled to 200 Hz. In order to correct the residual artifacts, a *Least Mean Squares* (LMS) filter was applied which adapts the filter coefficients in such a way that the error between the reference (TR trigger) and output signal of the LMS filter remains small. The output signal of the filter is then subtracted from the EEG signal.

5.3.2 Further variations of the Artifact Template Subtraction

In regard to the work of Allen et al. (2000) further similar methods were developed which all follow the basic principle of the AAS method. The post-processing, however, only occurred by low pass filtering.

Bénar et al. (Benar, Aghakhani *et al.*, 2003) evaded the asynchrony problem mentioned in the introduction of this chapter by establishing multiple artifact templates. The basic idea consists of combining the artifacts that show the same phase shift to the EEG signal into template groups and then correcting these accordingly.

The weighted moving averaged subtraction Method (MAS) of Becker et al. (Lazeyras, Zimine *et al.*, 2001) is based on the exponentially weighted median calculation of 120 signal epochs around the epoch at hand. The resulting template is again subtracted from the raw signal. Sun L. (Sun, 2009) has expanded this method with two additional steps. First, the current epochs are resampled according to a reference epoch, in order to solve the asynchrony problem (chapter 5.2 on page 25). In the second step the movements of the head are detected and integrated in the template correction. The movements are resolved temporally with eye-tracking hardware, and spatially with the Matlab (MATLAB, 2003) tool SPM (chapter 4.2 on page 20). This way, in addition to the imaging artifact, the movement artifacts can be corrected.

In contrast to the AAS based methods, the method of Garreffa et al. (Garreffa, Carnì *et al.*, 2003) can manage without the TR trigger. Peak detection separates the signal epochs through the recognition of the periodically occurring RF pulse artifacts. Beforehand the waveform of the artifact is analyzed for 48 seconds in order to determine the threshold for the peak detection. The AAS based template correction is then carried out in real-time.

A further method (Gonçalves, Pouwels *et al.*, 2007) (Goncalves, Pouwels *et al.*, 2007) which deals with the temporal shift of the EEG signal and the superimposed fMRI signal tackles the asynchrony problem through measurement of certain temporal parameters out of the artifact contaminated signal:

- MR sequence repetition time TR_{EEG}
- Time delay between MR Volume acquisition and the acquisition of the first slice DT
- Slice acquisition time ST

These three parameters make it possible to estimate the phase shifts of the epochs. With a FFT based resampling procedure, the phase shifts are equalized. After that three different types of template correction can be chosen:

- Slice Template Subtraction
- Volume Template Subtraction
- Slice and Volume Template Subtraction

A Taylor series based gradient artifact subspace (TS) method of Wan et al. (Wan, Iwata *et al.*, 2006) attempts to estimate the imaging artifacts as Taylor series. The order of the series is raised step by step until the squares error between the raw signal and the estimated artifact becomes minimal. Subsequently, the artifact is subtracted from the raw signal.

5.3.3 Further variations of the Post-processing for Residual Artifact Correction

The following methods that have the Artifact Template Subtraction step of the AAS method in common, apply higher statistic methods in the Post-processing step for the correction of residual artifacts.

5.3.3.1 fMRI artifact Slice Temporal Removal (FASTR) Method

The 'fMRI artifact slice template removal' method (FASTR) (Niazy, Beckmann *et al.*, 2005) estimates artifact residuals by using basis functions, generated from a channel-wise *principal component analysis* (PCA) (Jolliffe, 2002). The derived basis functions are added to the resulting templates of the Artifact Template Subtraction step and the final template is removed from the raw input signal. Finally a least mean squares filter is applied for noise cancellation.

This method is based on an empirical assumption of the number of the *Principal Components* (PC's), i.e. in case of an incorrect estimation the wanted EEG signal can be removed as well.

In his dissertation, Mandelkow H. (Mandelkow, 2009) discusses several different criteria for an automatic choice of the PC number:

- Variance Difference criterion: Eliminate PCs of highest variance if significantly different from the rest (Niazy, Beckmann *et al.*, 2005).
- Cross-Correlation criterion: Eliminate PCs for with the maximal cross-correlation
- Variance Normalisation criterion: Scale PC signals to match the pre-scan variance.
- Wiener Filter criterion: Assimilate PC signal spectra to the corresponding baseline spectra by eliminating peaks.

5.3.3.2 Independent Component Analysis (ICA) based approaches

The ICA is a statistical method used to separate the components of a signal which show maximum mutual temporal independence (Hyvärinen, 1999). The main goal is to subtract the EEG independent signal components from the raw signal so that the EEG remains. Nevertheless the estimation of the model order remains main problem as well as by PCA based methods.

In the work of Mantini et al. (Mantini, Perrucci *et al.*, 2007) ICA was applied after the AAS filtering step. However Ryali et al. (Ryali, Glover *et al.*, 2009) applied the ICA directly.

5.3.4 Frequency Domain Filtering Methods

As mentioned in chapter 5.2 (page 25) the imaging artifact occurs as greatly calculable spectral lines. The 'frequency removing method' (Hoffmann, Jäger *et al.*, 2000) deals with the suppression of these spectral lines with band pass filters. In order to successfully apply these methods, the spectral components of the imaging artifacts and the wanted signal must be well separated so that the used signal is not filtered out.

A similar approach was also conducted by Sijbers et al. (Sijbers, Michiels *et al.*, 1999) and Grouiller et. al. (Grouiller, Vercueil *et al.*, 2007). The former is called 'adaptive restoration scheme' in which the power spectrum of the template, consisting of 15 epochs, is adapted to the current raw signal with a scaling factor. Subsequently the template spectrum is substracted from the spectrum of the epoch of the raw signal. The latter relies on the calculation of the Fourier transform of the signal epoch of the artifact template and the raw signal. Where the raw signal indicates the same strong spectral parts as the templates, it is weighted inversely and transformed back to the time domain.

5.4 Pulse related artifact (PA)

Aside from the Imaging artifact, a further one emerges which already becomes visible in the EEG signal at the mere positioning of the test person in the MR scanner. The so-called *pulse*

related artifact (PA) emerges after the R Peak of the ECG with a variable time delay of approximately 220 ms (Allen, Polizzi *et al.*, 1998). As a result, it can be excluded that this is not a matter of a simple cross-talk of the ECG signal, but a complex interaction of mechanisms which arise from the cardiovascular system in correlation to the main magnetic field B0 of the MR scanner (Debener, Mullinger *et al.*, 2008). The next chapter summarizes the current insights which serve to characterize these artifacts. Subsequently, filter algorithms will act as suppressants to these artifacts.

5.5 Characteristics of the Pulse Related Artifact

Even though the PA has become noticeable already in the first simultaneous EEG-fMRI measurements, the exact origins of this artifact are still not explored in detail. The work of Sijbers et al (Sijbers, Van Audekerke *et al.*, 2000) sums up the main origins of the pulse related artifacts:

- "small cardiac related movements of the body" (Hill, Chiappa *et al.*, 1995),(Allen, Polizzi *et al.*, 1998),(Müri, René M., Felblinger, Jacques *et al.*, 1998)
- "small but firm movement of the electrodes and scalp due to expansion and contraction of scalp arteries between systolic and diastolic phase (Allen, Polizzi *et al.*, 1998).Ives suggested these to originate from the acceleration and abrupt directional change of blood flow in the aortic arch"(Ives, Warach *et al.*).
- fluctuation of the Hall-voltage due to the pulsating speed changes of the blood in the arteries (Müri, René M., Felblinger, Jacques *et al.*, 1998),(Allen, Polizzi *et al.*, 1998). Even with precautions taken, such as firmly fixing the electrodes to the scalp, cardiac pulses commonly generate artifacts with a standard deviation considerably larger than the EEG variations".

So far is definitly known that it is a time locked event to the R peak of the ECG, which changes the shape channel-wise, individual-wise and time-wise. The amplitude deflection rises with the intensity of the main field B_0 and is about 50 µV at 1.5 T (Mulert e Lemieux, 2010), and the frequencies are widely spread over the spectrum of the EEG signal. In recent studies it has become clear that the artifact starts to interfere when the heart rate becomes higher (Vincent, Larson-Prior *et al.*, 2007), (Mulert e Lemieux, 2010). Figure 27 illustrates the approximate course of the PA. The signal segments are recorded time-locked with the R peak and placed on top of each other to make the morphology alternation more clear.

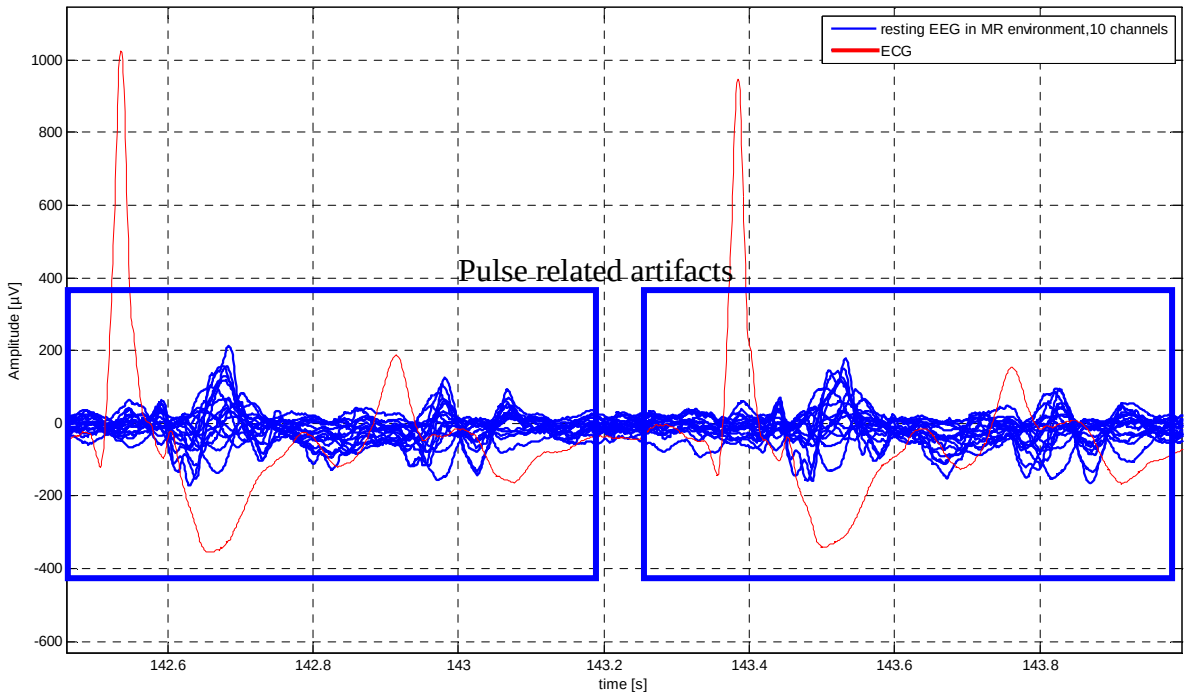

Figure 27: Overlaid PA of 10 EEG channels time locked to the ECG R-Peak.

5.6 Pulse Related Artifact filtering methods

Figure 28 shows the base frame of the methods presented here. Aside from the limited effectiveness, all the methods have in common the same problem of temporal detection of the PA. Whereas the PA is time-locked to the R-Peak of the ECG, peak detection is generally used to indicate the position of the R-Peak.

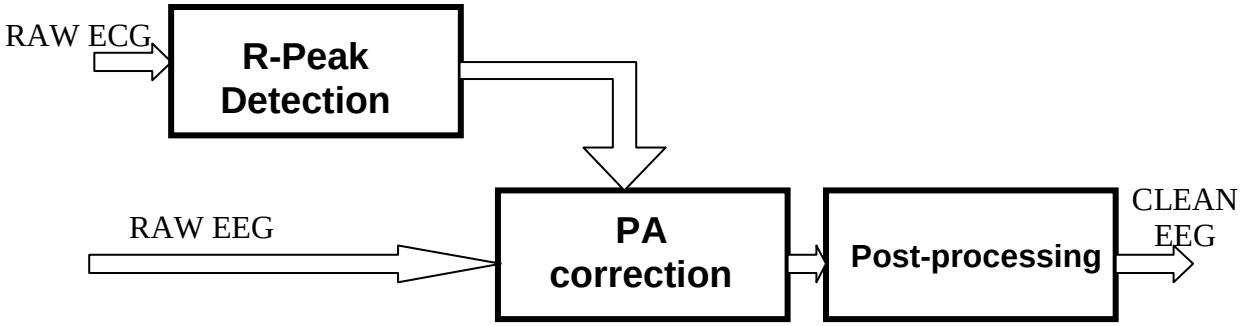

Figure 28: Base frame of pulse related artifact (PA) correction methods

Assuming the temporal position of the R peak, the PA peak position is either searched for or constant, depending on the filtering method. Allen et al. (Allen, Polizzi *et al.*, 1998) published an empiric value of approximately 220 ms for the distance between the R peak and PA. Considering the variation of the temporal shift between PA and R peak, the approach of the automatic PA peak detection, using the so called *Global Field Power* (GPF) (Skrandies,

1990), is more efficient. The GFP is denoted as the standard deviation over time (Strik e Lehmann, 1993). Consequently, the peak position of the PA was defined as the temporal centre between two minima which confine the maximum of the Global Field Power.

The PA-containing timeframe is used for the PA-suppression. The size of the time frame is beneath a sometimes unreliable R peak detection the second weak point. If the timeframe is too short, the residual artifacts remain in the EEG, and if it is too long, then the wanted signal could be filtered out. For the definition of the artifact length, two different approaches are possible. Either the length of the artifact is defined as the percent proportion of the mean R-Peak to R-Peak (R-R) periods (Ellingson, Liebenthal *et al.*, 2004), or the PA period is adapted to the appropriate R-R period (BrainVision Analyzer software). As far as the filtering method is concerned, all the filters mentioned in chapter 5.3 (up to the Frequency Domain Filters, page 28), are also applicable for this artifact. The basis for this also assumes a periodicity of the artifact, as well as the statistical independence of the EEG signal and the PA. The AAS method (chapter 5.3.1, page 29) is, in relation to the PA, also the most prominent method. The template is generated with a Moving Average Filter and subtracted from the image artifact freed EEG, (Allen, Polizzi *et al.*, 1998; Müri, R. M., Felblinger, J. *et al.*, 1998; Goldman, Stern *et al.*, 2000; Ellingson, Liebenthal *et al.*, 2004). Because of the morphological alteration of the PA, the selection of the main components of the PCA (Negishi, Abildgaard *et al.*, 2004; Niazy, Beckmann *et al.*, 2005) or independent components of ICA methods (Benar, Aghakhani *et al.*, 2003; Srivastava, Crottazherbette *et al.*, 2005; Briselli, Garreffa *et al.*, 2006) is more critical than in relation to the imaging artifact.

An entirely new concept was presented by Bonmasser et al. (Bonmassar, Purdon *et al.*, 2002), in order to suppress the PA adaptively. A piezoelectric-transducer with a silicon filling was placed on the temporal artery in order to detect movement artifacts as well as PA artifacts, which serve as a reference signal for an adaptive *Kalman* filter. Inspired by the idea of hardware-based detection of head movements three similar approaches followed. In el al. (In, Lee *et al.*, 2006) and Kim et al. (Kim, Yoon *et al.*, 2004) use the *electrooculogram* (EOG) as a reference signal for an adaptive filter, and Masterton et al. (Masterton, Abbott *et al.*, 2007) attached three loops on the electrode cap to model the head movements for a adaptive filtering process using the Recursive Least Squares algorithm.

The *moving general linear model* (mGLM) (Vincent, Larson-Prior *et al.*, 2007) approach, is based on the averaged template subtraction with the difference that the coefficients of the Fourier transform of the PA template are estimated by using a multi-channel template. The resulting PA template is subtracted from the EEG time-locked to the ECG signal.

5.7 Influences of the Helium Pump

The continuous cooling of the main magnet of the MR scanner by a helium pump (see chapter 4, page 17) results in small vibrations which can be detected by EEG amplifiers (Mulert e Lemieux, 2010). The amplitude is approximately in the range of EEG signals (10-200 µV) and the frequencies vary around 40 Hz. The undefined spectral occurrence allows just band pass filtering to reduce this artifact systematically. The best option is to switch the pump of, but this step is very time limited and consequently not recommendable. The vibrations can be most widely reduced by ballasting the electrode leads with sand bags.

6 Online MRI related artifact suppression methods and Setup for motor imagery BCI

The main goal which is pursued in an EEG/fMRI-combined BCI is to enable the measurement and evaluation of brain activity during the conduction of a BCI paradigm. The proficient temporal resolution of the EEG, as well as the excellent spatial resolution of the fMRI should provide the significant advantage in source localization of active brain regions. In order to debate the difficulty of the signal processing properly, accompanied with a combined EEG/fMRI measurement, the well documented motor imagery BCI presented in chapter 3.3 (Page 9) was applied (Guger, Edlinger *et al.*, 2003) (Pfurtscheller e Neuper, 2001).

Before the BCI measurements were performed, a series of test measurements was necessary with the aim of finding the optimal settings of the MRI scanner, the EEG system and the chosen filter methods for MRI related artifact reduction.

The following sub chapters show a step wise development of the filtering methods based on the measurements and the subsequent conclusions. The last part of this chapter contains the final BCI measurement setup, which was realized due to the gained knowledge.

All measurements were realized with the MRI scanner and EEG system described below. The resulting performance of the filtering steps was compared by overlaying the estimated power spectra applied with the Welch power spectrum estimation method (Welch, 1967). In order to compare different filtering methods, the *relative improvement normalized power spectrum* ratio (RINPS) (6.1) derived from the INPS (Tong, Bezerianos *et al.*, 2001) was calculated. This coefficient is the percental power density (P) ratio of the harmonics (i) of the MRI related artifact in the raw EEG (EEG_{raw}) and the artifact free EEG (EEG_{clean}). Consequently, this value provides information on how many percent of the original artifact power was suppressed over a defined amount of artifact harmonics. The frequency window width, within which the power density was calculated, depends on the artifact and is stated individually artifact in the results section.

$$INPS = \frac{\sum_{i=1}^{N} P_i^{EEG_{raw}}}{\sum_{i=1}^{N} P_i^{EEG_{clean}}} \longrightarrow RINPS = 100 - 100 \cdot \frac{\sum_{i=1}^{N} P_i^{EEG_{clean}}}{\sum_{i=1}^{N} P_i^{EEG_{raw}}} \tag{6.1}$$

The harmonics of the imaging artifacts can be calculated by using the equations (5.1) and (5.2). The pulse related artifact occurs periodically with the EEG so the multiple of the mean heart rate can be assumed as the approximate harmonics of the PA.

6.1 MRI Scanner

The functional imaging was performed with the standard Siemens EPI BOLD sequence *ep2d_bold_moco_Motor01* (Siemens, 2002) on a 3 Tesla MR scanner (Siemens Trio, Siemens, Germany) with an 8 channel RF coil. For timing, the BCI, and the filtering process, a volume trigger was recorded. This timing signal indicates the acquisition start of a volume by a short TTL impulse, and is externally accessible from the control cabinet of the MRI scanner via installation of a fibre optic cable. For the visualization of the BCI paradigm in the MR tube, a customized mirror was placed on the head coil.

6.2 EEG System

The recording of the EEG signal was carried out by an MRI safe 32 channel EEG amplifier (SD MRI, Micromed S.p.A., Mogliano Veneto, Italy), consisting of an electrode cap, the head box, a fibre optic cable and a data acquisition card (see Figure 29).

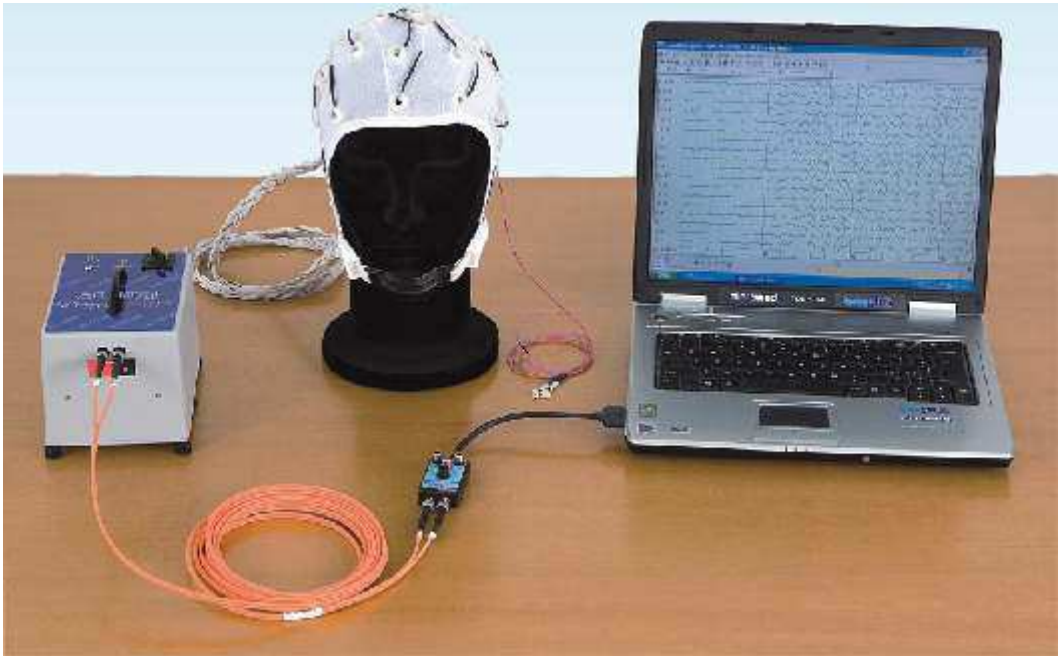

Figure 29: MRI safe 32 channel EEG amplifier (SD MRI, Micromed S.p.A., Mogliano Veneto, Italy). Electrode cap, head box, fibre optic cable, data acquisition card

The volume trigger was recorded with an optoelectronic signal converter, which is an additional device of the recording hardware. Instead of the maximum possible sample rate of

2048 Hz, 1024 Hz were used because the resulting higher data-rate strongly increases the computation time. The EEG signal was recorded with a proprietary acquisition Software (System PLUS Evolution, Micromed S.p.A., Mogliano Veneto, Italy). This program allows looping through the raw signals via network interface in order to carry out external signal processing and BCI experiments. The 32 channel EEG recording cap also contains an ECG channel, which was used for the purpose of detecting the pulse related artifact.

6.3 Online MRI related artifact reduction methods

As clarified in chapter 3.1 (Page 6), a BCI builds a closed loop communication between the computer and the human brain. The classification method, the quality of the signal and the temporal delay of single components exert the biggest influence on a successful communication. Consequently, the main task of the artifact reduction algorithms in a combined EEG/fMRI BCI measurement is to establish a signal quality equivalent to the quality of measurements outside of an MR environment in real-time. At the same time, the computation time should not be affected too much so that as many channels as possible can be recorded.

6.3.1 Image Acquisition Artifact

Looking back to the overview of the imaging artifact algorithms, only the pre-processing step and the Artifact Template Subtraction (chapter 5.3, page 28) complies with the requirements of real time processing, given that all the further filtering steps require either the complete signal for filtering (PCA, ICA based methods) or cause delays of a few seconds (Least Mean Squares Filter). The building of the templates can generally ensue in two different ways. Since the imaging artifact recurs quasi-periodically in every single slice acquisition, peak detection can separate the signal periods by capturing the distinct RF pulse. These signal fragments are used for a moving average template correction (slice based averaging method in Figure 30).

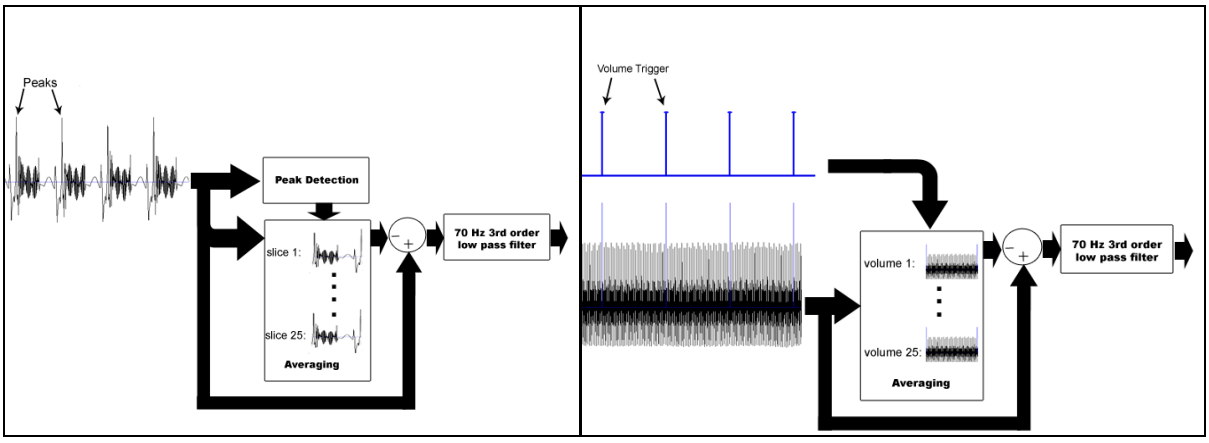

Figure 30 Shematic signal processing diagram of slice based averaging method (left) and volume based averaging method (right)

In a second attempt, the signal trains are subdivided in intervals with the length of a TR time with the help of the volume trigger (volume based averaging method in Figure 30). In the course of the thesis, both approaches were conducted as MATLAB offline functions, and online Simulink blocks and are subsequently discussed.

6.3.1.1 Phantom measurements for evaluation of artifacts and optimization of filtering methods

The evaluation of the pure imaging artifact and further MRI related artifacts was done using watermelons. Figure 31 shows the principal test setup. The melon (4.) was fixed in the scanner (1.) with support pillows and double-sided adhesive tape, to prevent motion. The electrode cable of the cap was stabilized with sandbags and tape in order to suppress vibrations of the cables. The headbox (3.) was connected via an optical cable to an adapter (5.) which converts the optical signal and sends it together with the volume trigger, coming from the optoelectronic signal converter (6.), to the acquisition laptop (7.), which records and pushes the data through to a signal processing laptop (8.) via TCP/IP port. A self-programmed C++ program loads the EEG data into Simulink for the purpose of data acquisition, signal processing and consequent realization of the BCI experiment.

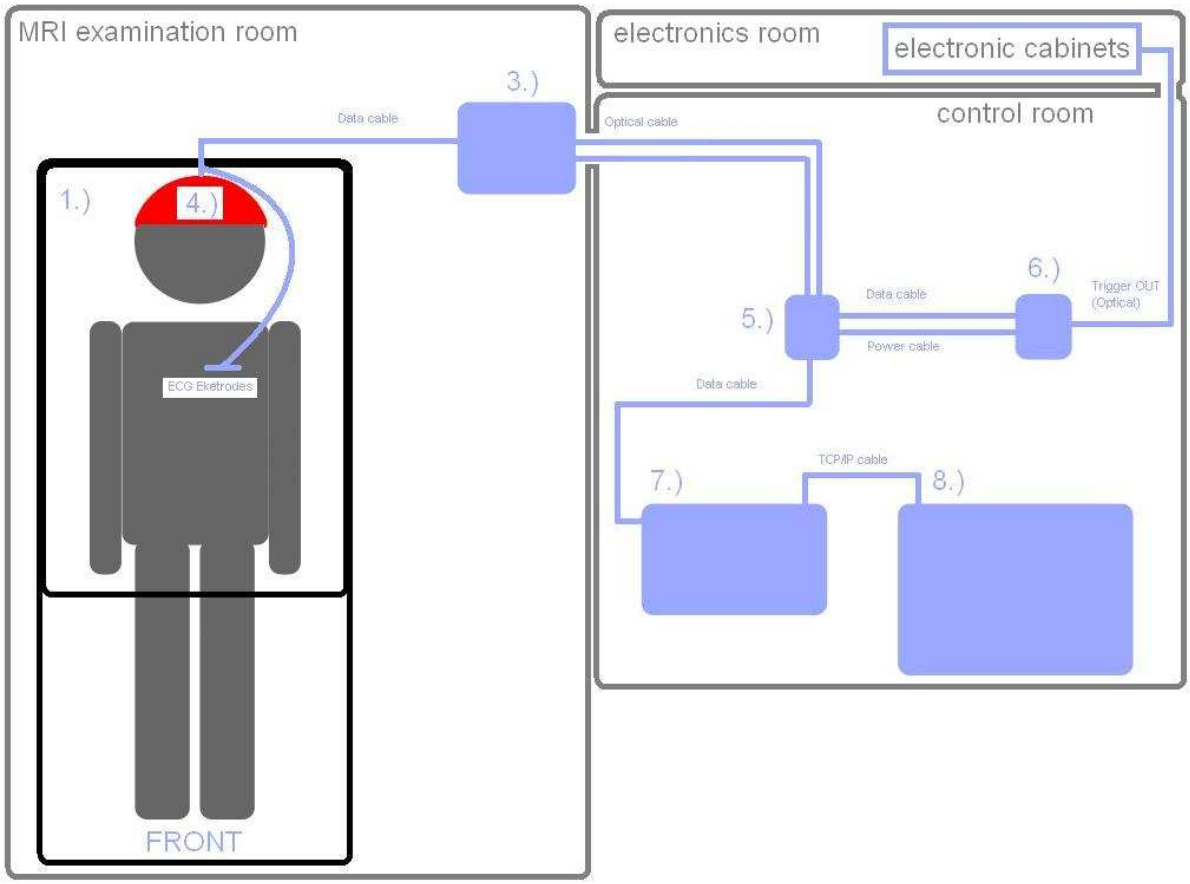

Figure 31: Test setup for phantom measurements. MR scanner (1.), EEG headbox (3.), (4.) phantom or test person, (5.) signal converter, (6.) volume trigger signal converter, (7.) acquisition laptop, (8.) signal processing laptop

In order to study the influences of the MRI scanner on the EEG signal, a 15 min. noise signal was recorded without any image acquisition, and compared to the artifact contaminated EEG. The repetition time TR is 2860 ms and the number of slices is 36. An overlay of the power spectra showed in Figure 32 reveals the influences of the noise background and the imaging artifacts. As stated in the literature (see chapter 5.2, page 25), the fundamental frequency f_1 of the imaging artifact is related to the MR scanner settings in the following way:

$$f1 = \frac{Number\ \ of\ \ Slices}{TR} = \frac{36}{2.860s} = 12,587Hz \qquad (6.2)$$

Further spectral lines arise *n* times the reciprocal of the TR time:

$$f1,n = \frac{Number\ \ of\ \ Slices}{TR} \pm n \cdot \frac{1}{TR} = \frac{36}{2.8s} \pm n \cdot \frac{1}{2.8s} = 12.587Hz \pm n \cdot 0,35Hz \qquad (6.3)$$

The residual spectral lines, which occur as harmonics of 2 Hz, are also visible in the signal without any image acquisition, which is why it is assumed that these spectral lines have their origins in the MR scanner vibrations (see chapter 5.7, page 36).

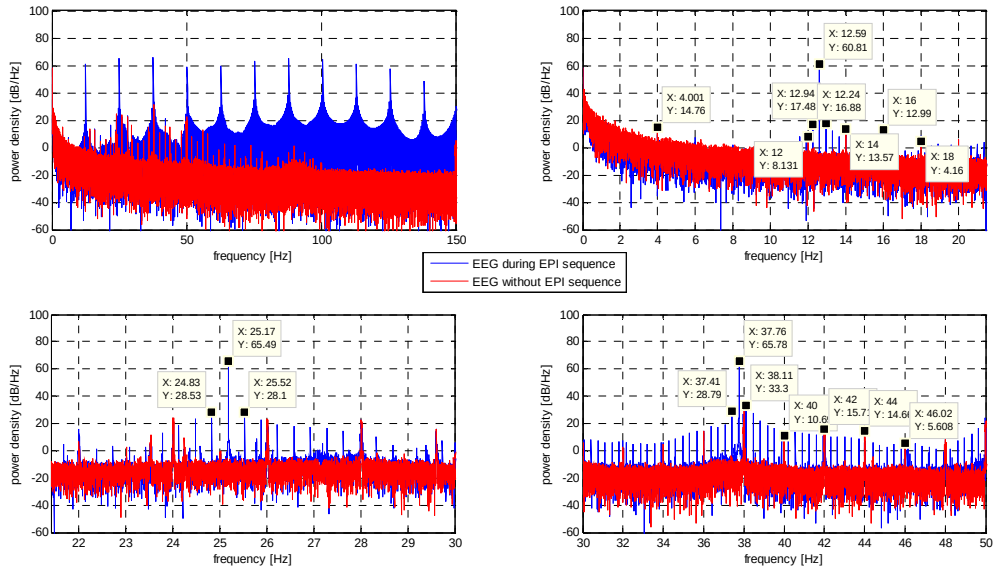

Figure 32: Comparison of the EEG power spectra on a typical EEG electrode with (blue) and without EPI acquisition (red).
<u>TOP LEFT:</u> Full spectra to 150 Hz. Remaining images: Zoom on the power spectra of the multiples of the fundamental EPI frequency of 12,587 Hz (36/(2.86 sec.)). Spectral lines occurring as harmonics of 2 Hz seem to be consequences of vibration artifacts.

The volume trigger and the EEG data evaluation showed that the TR periods and the imaging artifact are subject to a strong temporal jitter, which is assumed to arise from the unsynchronized system clocks of the EEG system and the MRI scanner, as stated in the literature. The template subtraction methods mentioned in the literature tackle the problem by interpolation of the imaging artifact epochs to the imaging artifact template. This procedure demands that the artifact epoch at hand is fully recorded before it can be aligned, thus the clean EEG is delayed by the duration of an imaging artifact period.

The evaluation of EEG test data sets, provided by Micromed (Micromed S.p.A., Mogliano Veneto, Italy), made clear that the temporal jitter disappears if the signal period of the imaging artifact is an integer multiple of the sampling period of the EEG system.

The above mentioned volume artifact period of 2,860 seconds, at a sample rate f_s=1024 Hz, results in 2928,64 (TR* f_s) samples. By dividing this value with the slice number of 36 slices, the sample period of one slice artifact is calculated. The result is that the TR period randomly jitters between 2928 and 2929 samples.

Figure 33 shows the power spectra of an optimized test data set with TR= 3 sec. and a slice number of 16 at f_s=1024 Hz of a Philips MR scanner (Philips Healthcare, DA Best,

Netherlands). The resulting number of samples is consequently 3072, and the slice artifact period is 192 samples. The calculated periods over all 200 recorded volumes are constant, so an interpolation procedure is not necessary. The overlaid power spectra of the raw EEG, and the clean EEG of the volume- and slice artifact based averaging filtering method show that the filtering performance of the slice based method is slightly better over a wider frequency region.

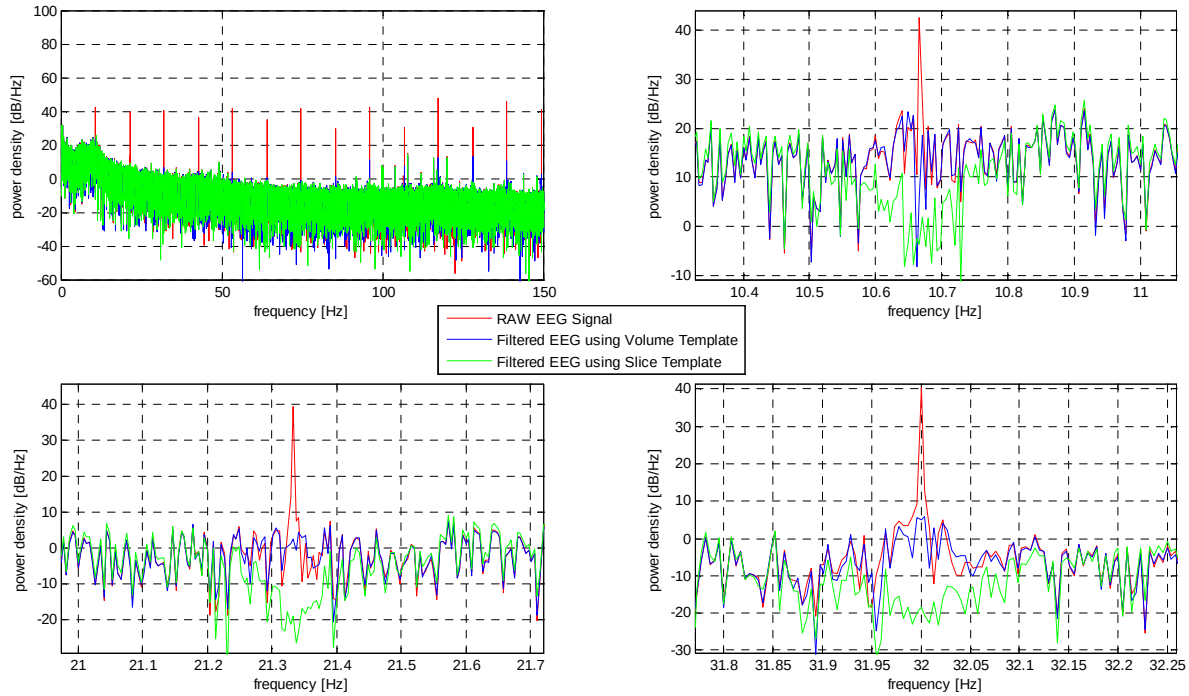

Figure 33: Comparison of the test data raw EEG power spectra (red) on a typical EEG electrode with the imaging artifact freed EEG using volume artifact based averaging method (blue) and slice based averaging method (green).
TOP LEFT: Full power spectra to 150 Hz. Remaining images: Zoom on the power spectra of the multiples of the fundamental EPI frequency of 5,33 Hz (16/(3 sec.)) .

In order to find out if the periodicity of the imaging artifact can be observed on the Siemens TRIO scanner, further measurements were realized with optimized MR settings (TR=3 sec. slice=24, f_s=1024Hz,→ TR in samples = 3072, slice artifact period =128).

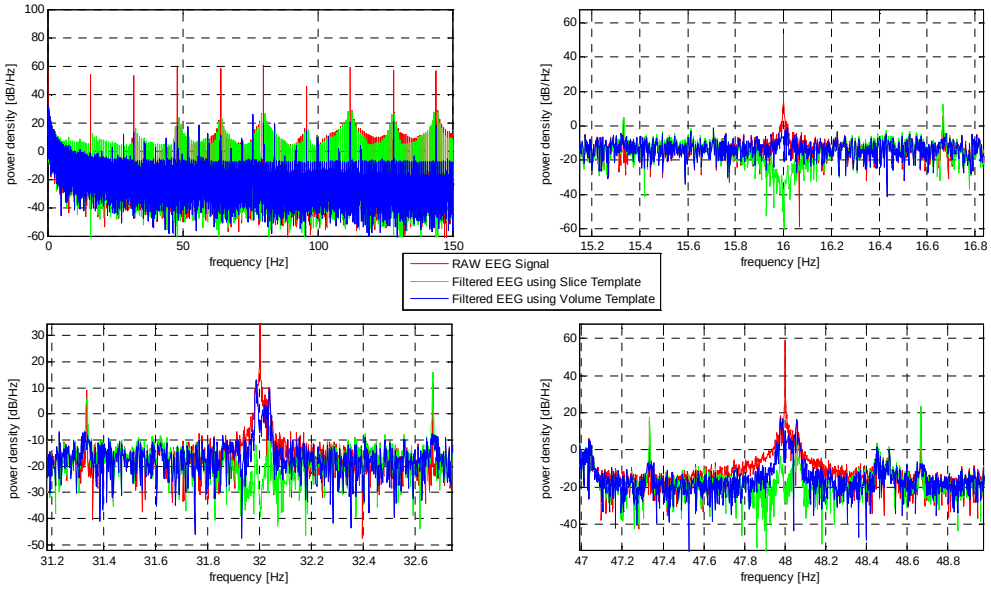

Figure 34: Comparison of phantom data raw EEG power spectra (red) on a typical EEG electrode with the imaging artifact freed EEG using volume artifact based averaging method (blue) and slice based averaging method (green).
<u>TOP LEFT:</u> Full power spectra to 150 Hz. Remaining images: Zoom on the power spectra of the multiples of the fundamental EPI frequency of 8 Hz (24/(3 sec.)) .

The power spectra comparison of the slice based and volume based averaging method reveals a better performance of the volume artifact subtraction (Figure 34), which is shown in the fact that not only the harmonics of the base frequency of f_1=8 Hz are suppressed, but also the frequencies $f_{1,n}$ of the convolution products over a wider spectral range. The worse artifact suppression of the slice based method can be attributed to the still temporal jitter of the slice artifact, while the jitter over volumes seems to be constant. The amplitude variation of the slice artifact is also more distinct, which can be proven by a comparison of the standard deviations per sample of the same data set.

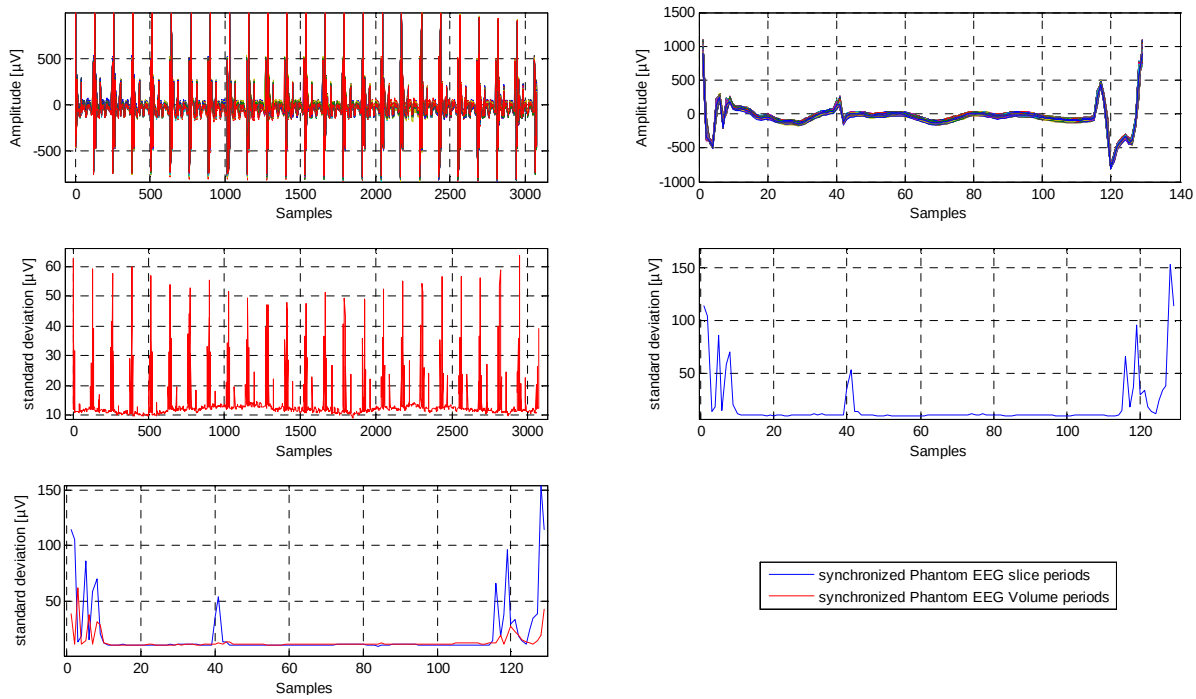

Figure 35: Comparison of the standard deviation per sample of 400 slices and 400 volumes of a typical EEG channel.
TOP: left: time series of 400 overlaid volume artifact periods, right: time series of 400 overlaid slice artifact periods.
MIDDLE: left: ensemble standard deviation of 400 volume artifact periods, right: standard deviation ensemble of 400 slice artifact periods
BOTTOM: Comparison of the ensemble standard deviation of 400 volume artifact periods and 400 slice artifact periods. The standard deviation of the slice periods is higher in every sample, and consequently so is the amplitude variability over time.

The ensemble standard deviation of 400 slices, compared to the fist slices of all recorded 400 volumes (Figure 35 left, bottom), shows that it is more than twice as high as the ensemble standard deviation of the volumes in the worst case. For all other samples the deviation is still higher.

However, long time measurements with synchronized settings yield that the synchronization of the EEG system and the MR scanner has a limited impact on the reproducibility of the volume artifact. In random time periods, which endure at least 4 minutes, the whole volume artifact starts jittering again (Figure 36). This residual jitter is extended over maximally one sample, and is considered in the real time filtering process by computing of the cross correlation factor between the volume at hand and the template over a quarter of the slice period. If the factor falls below 0.7, then the artifact volume is shifted until the maximum of the correlation factor is reached.

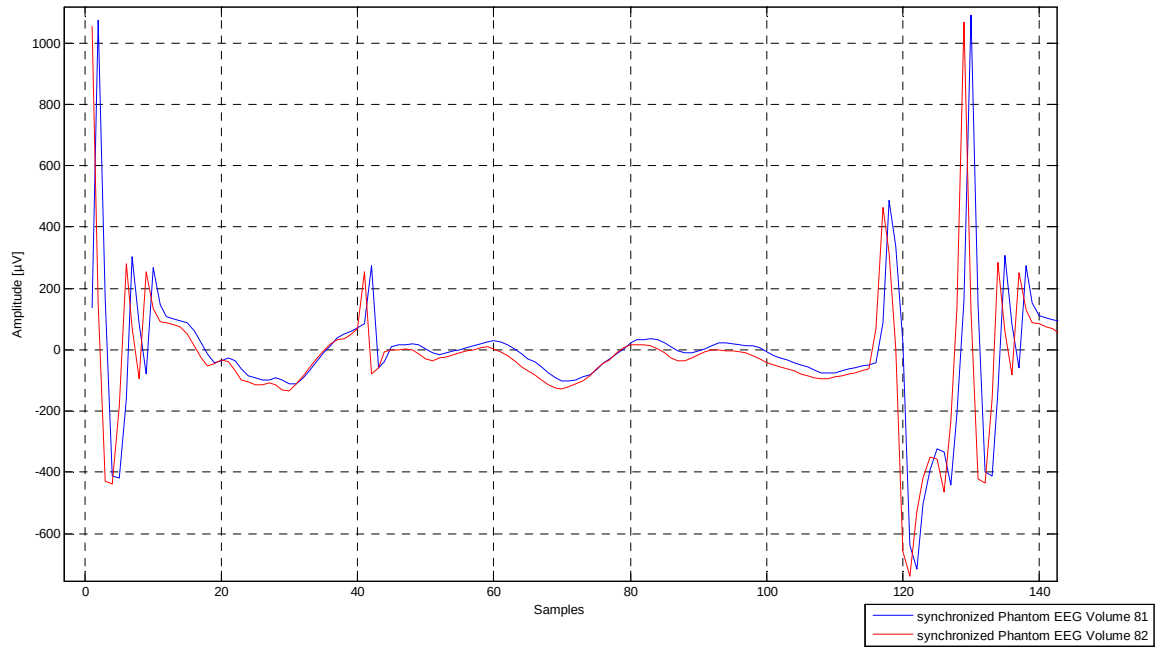

Figure 36: Volume artifact time jitter, during long time EPI acquisitions.

Based on the better correction performance, the volume based averaging method was applied in the following BCI experiments.

6.3.1.2 Qualitative comparison of Imaging Artifact filtering methods on resting EEG

A final comparison of the volume based method and the AAS method (chapter 5.3.1, page 29) should reveal the potential performance loss due to the simplified filtering approach of the volume based method. The order of the LMS Filter was set to 20, and the step size to 0.05/(number of weights x variance of the reference signal). The number of averaged epochs is 25, derived from the assumption that the amplitude of EEG events is in the range of 10-250 µV. "Hence A minimum of 25 epochs must be averaged so that the largest likely EEG event (250 µV) is reduced below that of the smallest (10 µV)." (Allen e P., 2000).

By comparing the cleaned EEG of unsynchronized (TR=2860 ms, 36 Slices) and synchronized (TR=3000 ms, 24 Slices) phantom datasets in the frequency domain, it is noticeable that the filtering performance is significantly better for synchronized data for both methods (comparing the power spectra in Figure 37 and Figure 38). In the synchronized data, the clean EEG follows the course of the raw except in the regions of the imaging artifact. However the, unsynchronized clean EEG contains additional noise, which was generated due to the misalignment of the averaged data epochs.

To prove that the filter performance of both methods is comparable, the time course of the artifact free data was depicted in Figure 39.

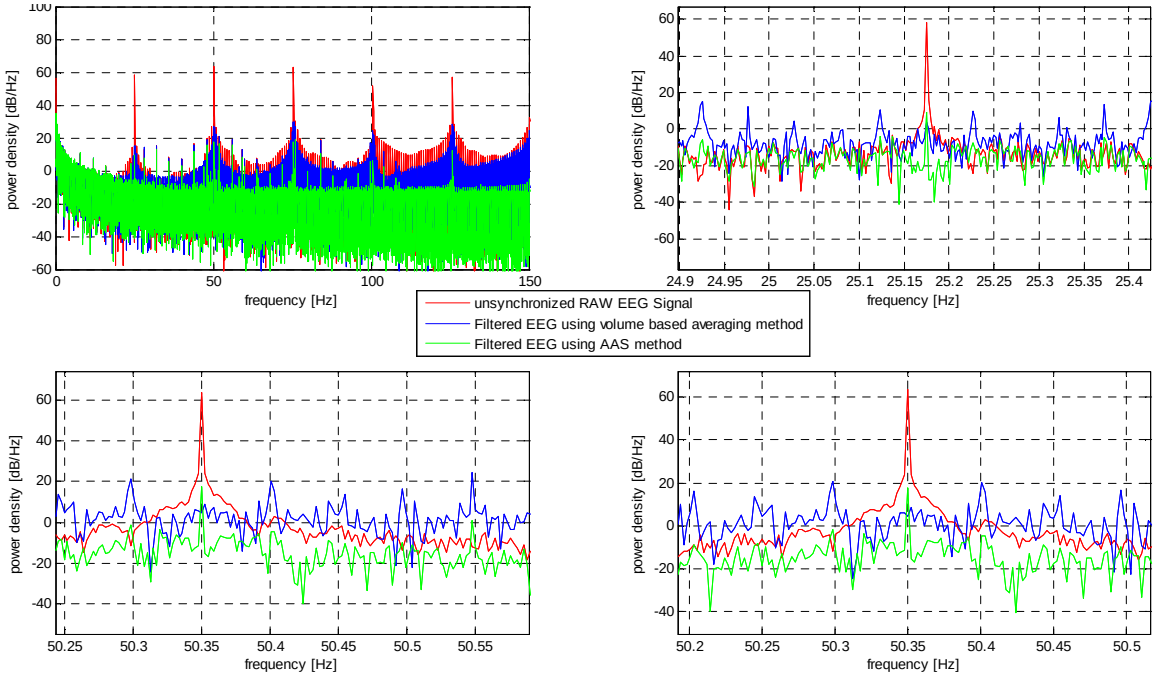

Figure 37: Comparison of unsynchronized phantom data raw EEG power spectra (red) on a typical EEG electrode with the imaging artifact cleaned EEG using the volume artifact based averaging method (blue) and the AAS method (green).
<u>TOP LEFT:</u> Full power spectra to 150 Hz. Remaining figures: Zoom on the power spectra arround the multiples of the fundamental EPI frequency of 12,587 Hz (36/(2.86 sec.)).

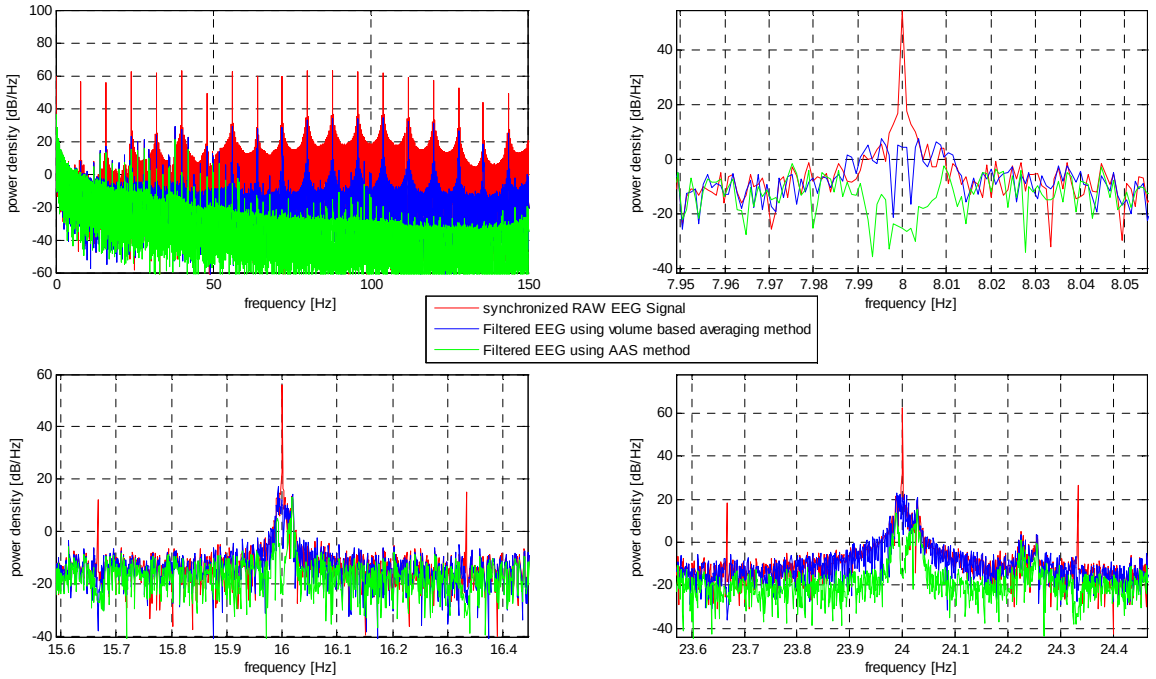

Figure 38: Comparison of synchronized phantom data raw EEG power spectra (red) on a typical EEG electrode with the imaging artifact cleaned EEG using the volume artifact based averaging method (blue) and the AAS method (green).
<u>TOP LEFT:</u> Full power spectra to 150 Hz. Remaining figures: Zoom on the power spectra around the multiples of the fundamental EPI frequency of 8 Hz (24/(3 sec.)).

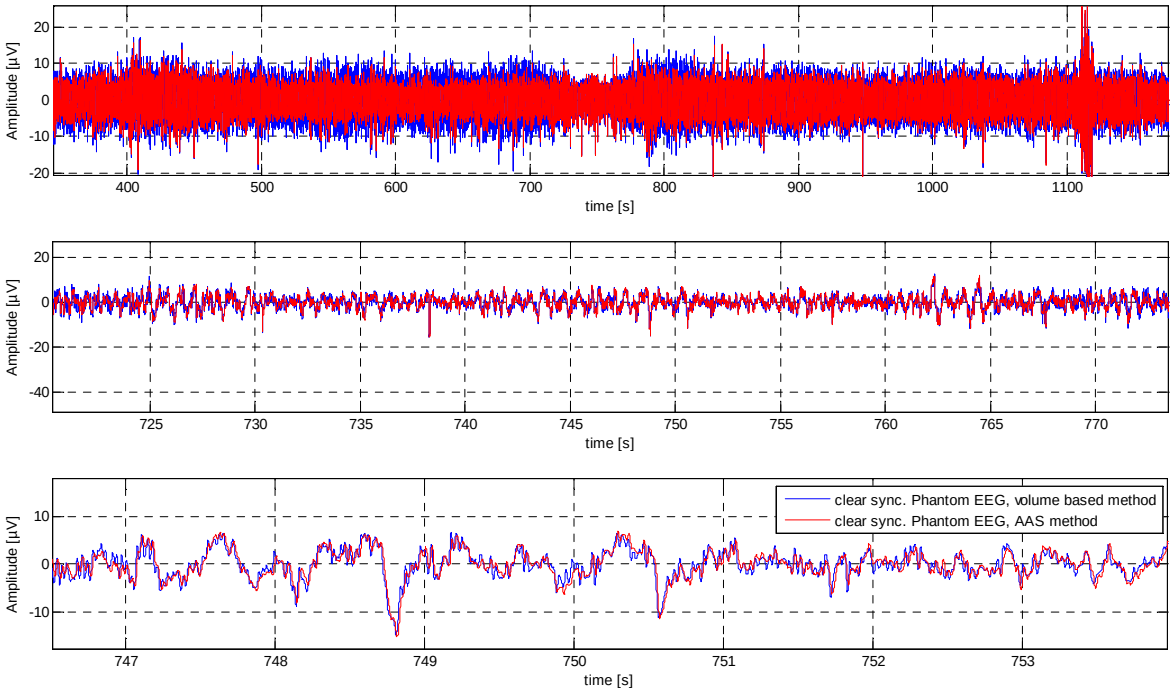

Figure 39: Time domain illustration of imaging artifact cleaned synchronized phantom EEG (TR=3000 ms, 24 slices) on a typical EEG electrode. The zoomed time course of artifact free data shows that the volume based method (blue) is still comparable to the AAS Method (red).

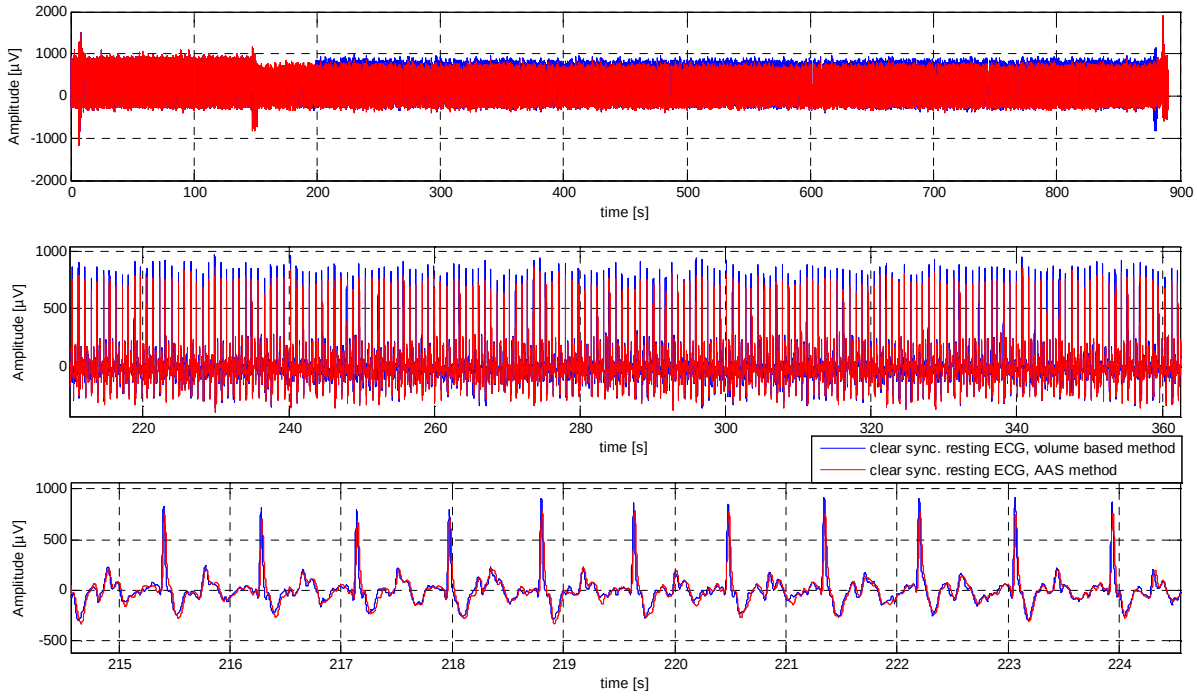

Figure 40: Time domain illustration of imaging artifact cleaned synchronized physiological ECG (TR=2000 ms, 32 slices). The zoomed time course of artifact free data shows that the volume based method (blue) is still comparable to the AAS Method (red).

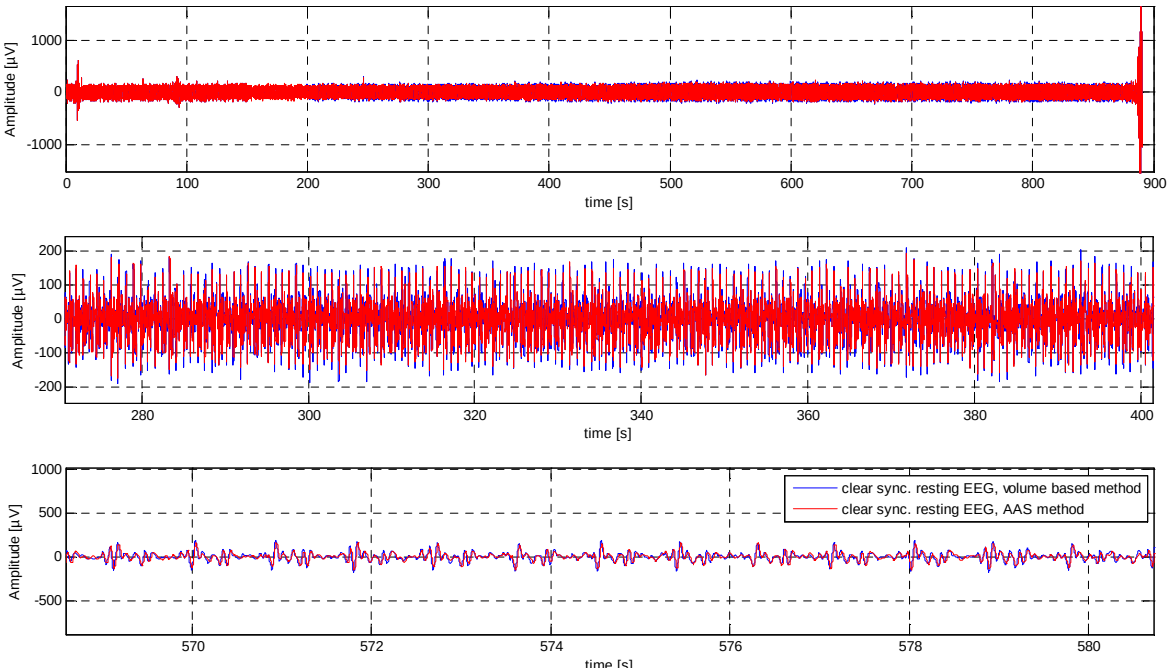

Figure 41: Time domain illustration of imaging artifact cleaned synchronized physiological EEG (TR=2000 ms, 32 slices). The periodic waveform on the bottom figure reveals the pulse related artifact.

Finally, the time domain illustration of artifact free human ECG (Figure 40) and EEG (Figure 41) (TR=2000 ms, 32 Slices) that the volume based method and the AAS method provide comparable results.

The RINPS (6.1) values, which were calculated for both methods by applying a frequency window of 0.01 Hz on all harmonics of the imaging artifact to a frequency of 150 Hz for all recorded EEG channels, indicate that both methods suppress the imaging artifact by approximately 98% to 99,99% (Figure 42).

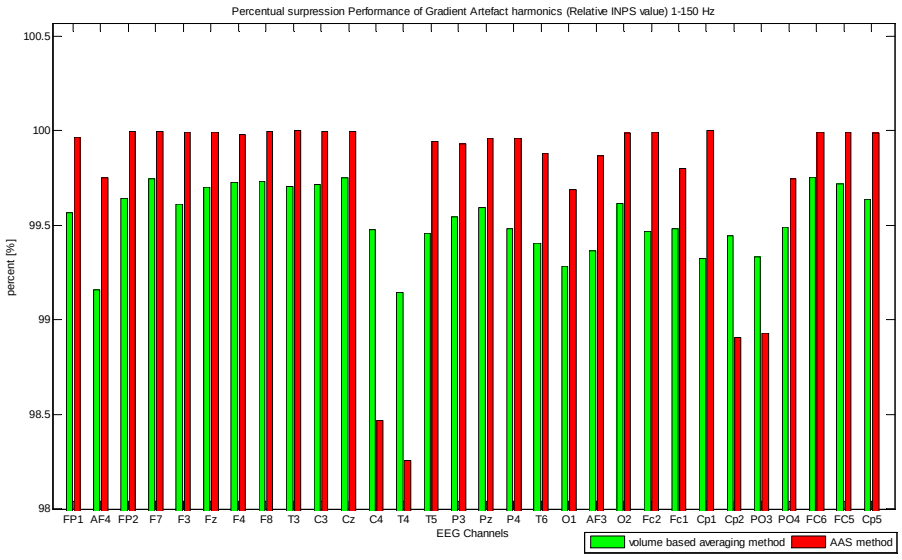

Figure 42: RINPS values of volume based averaging method and AAS method, calculated for all harmonics of the imaging artifact up to 150 Hz and all recorded channels separately.

The periodically occurring artifact in Figure 41 is not a cross talk between ECG and EEG channel, but rather the pulse related artifact which is discussed in the next chapter.

6.3.2 Pulse related artifact

Real time filtering of the PA is automatically intruduces temporal delays. As clarified in chapter 5.6 (Page 34), the use of an R-peak detector is essential in order to trigger the PA in real time. Therefore a heart-rate related delay of the acquired data can be expected. Additionally, a variable time span remains until the complete PA signal form is recorded. The Simulink Block g.HeartRate (G.Tec-Medical-Engineering-Gmbh, 2009) was applied for the real time detection of the R-peak. The subsequent filtering was carried out by means of subtraction of an artifact template, generated with a Moving Average Filter from the raw signal. In the further chapters this method is named *mean method*. The temporal distance between the R-peak and the PA is constant. The signal period of the PA was also defined to a fixed value derived from the distance of two R-peaks.

The test data for the filter evaluation is the resting EEG of a test person recorded in the MRI bore, since the PA occurs at the mere positioning of the test person in the MRI scanner. The measurement setup is the same as mentioned in chapter 6.3.1.1. (Page 40).

The final evaluation of the filtering method was carried out by comparing the resulting power spectra and RINPS to 3 offline correction methods.

6.3.2.1 PA detection

The main parameters of the averaged template based PA correction method are the position, the exact time duration of the PA and the number of averaging trials. In order to find them, a resting EEG data set was recorded in the MR bore without EPI sequence.

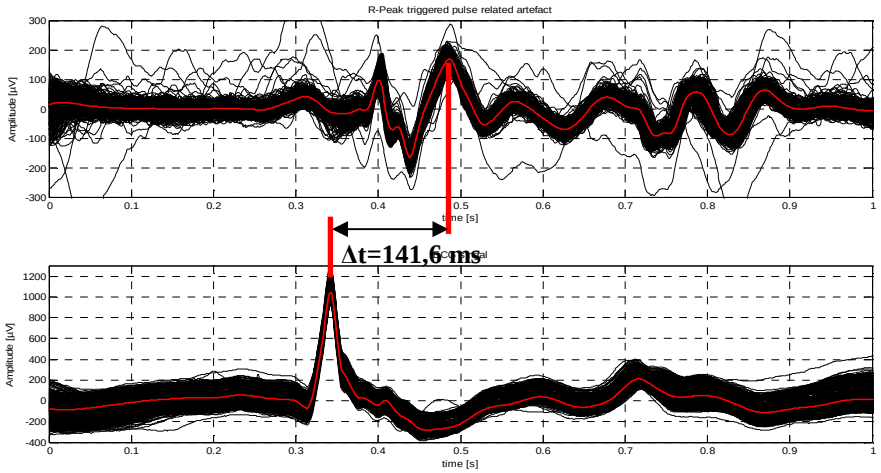

Figure 43: Time locked illustration of mean PA artifact (TOP) and mean R-Peak (bottom) over 500 trials

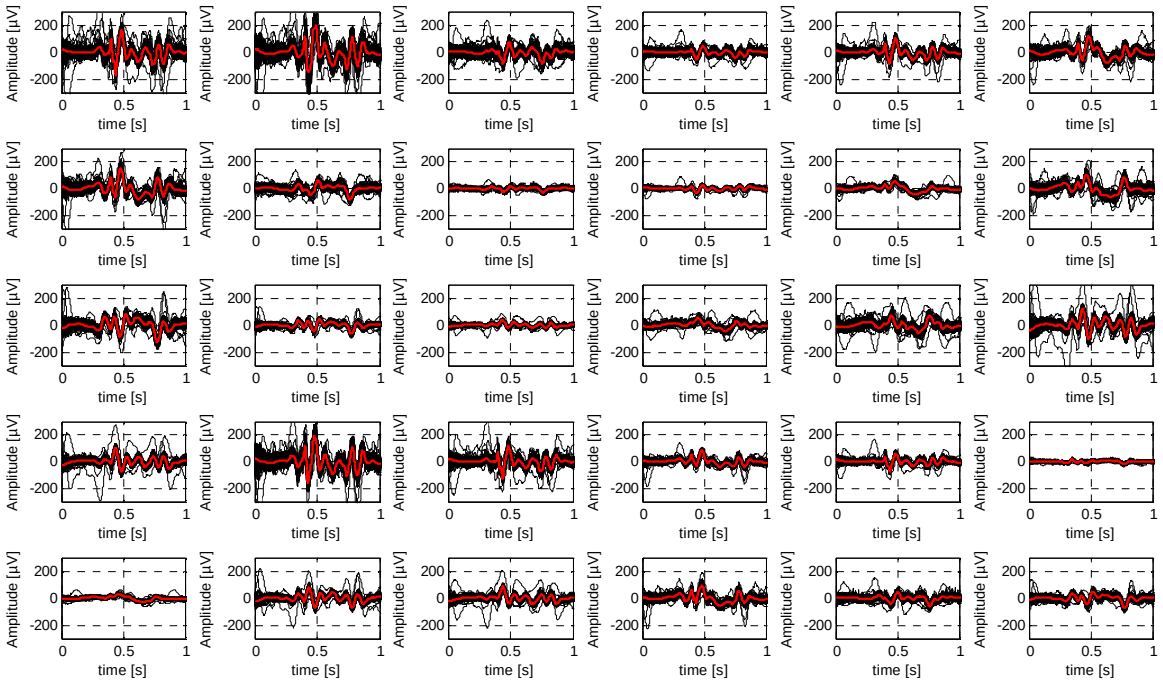

Figure 44: PA morphology on different EEG channels (black), overlaid with the mean time course of the PA (red).

The manual observation of the artifact revealed a remarkably constant time delay between the PA peak and the R-peak of 141,6 ms (see Figure 43), which can be observed on every EEG channel (see Figure 44). The power spectra of the resting EEG, compared to a resting EEG dataset outside the MRI environment, reveals the characteristic harmonics of the PA which usually occur at multiples of the heart rate (approximately 1 Hz) (Figure 45).

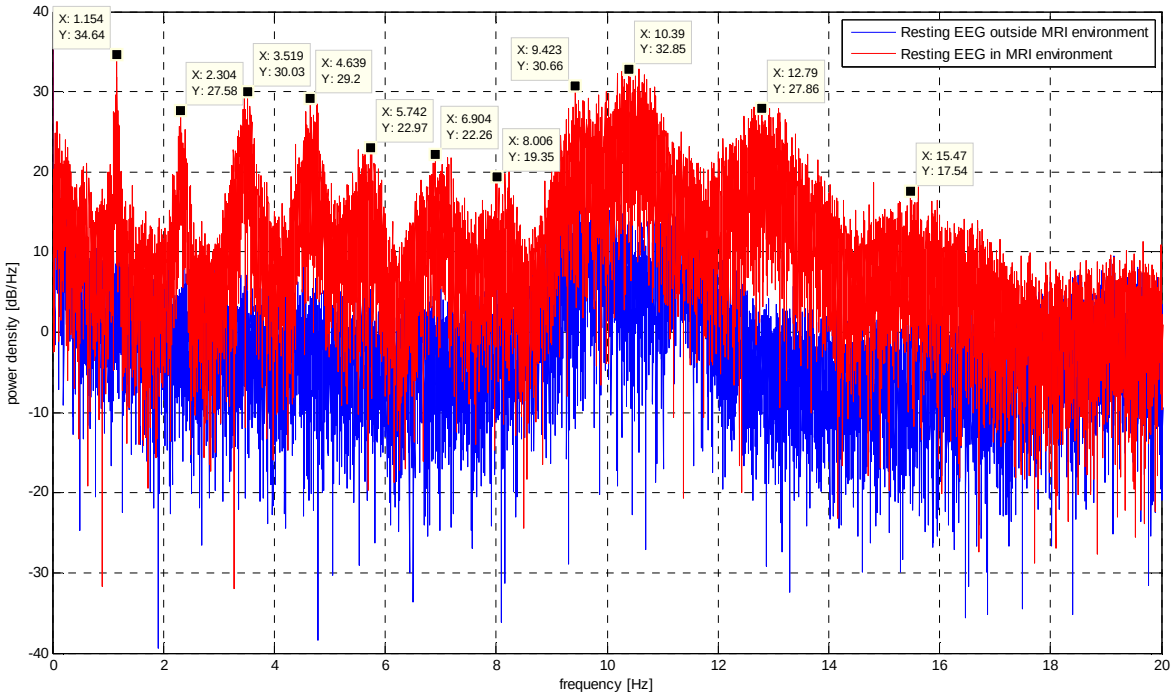

Figure 45: Power spectra of resting EEG inside (red) and outside (blue) MRI environment.

The major impact of the PA can be observed at a frequency range of 1-20 Hz. In the frequency range above 20 Hz, the EEG signal approximates the course of the EEG outside of the MRI environment.

The time window of the artifact was empirically assumed as the sum of the half distances between the R peak at hand to the previous and to the following R-peak. The number of averaging trials results in a compromise between specificity and sensitivity of the template from channel to channel. A visual inspection of the signal envelope of the raw EEG signal and the filtered data with an increasing number of PA trials revealed that a number of 10 artifacts are sufficient in order to suppress most artifacts. Figure 46 shows the dilemma of the PA trial choice. A smaller number of trials affect both the suppression of the PA artifact and the useful EEG signal. The respective increase of PA trials results in lower sensitivity of the template and subsequent reduced filtering performance.

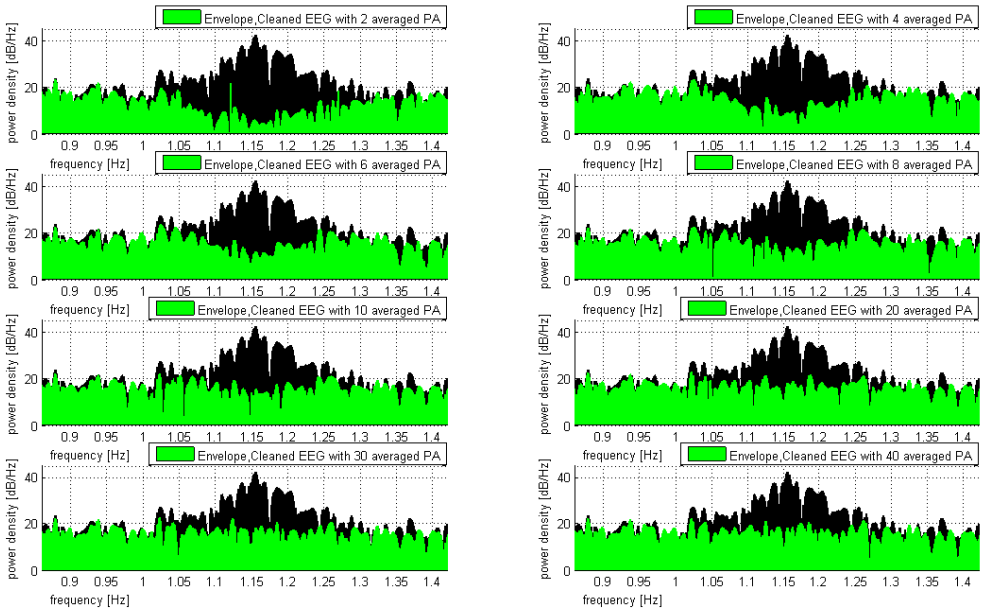

Figure 46: Power density signal envelope around the first artifact peak (1.154 Hz) of the raw EEG (black) and the clean EEG after application of the mean method with different PA averaging samples.

6.3.2.2 Qualitative comparison of Pulse related Artifact filtering methods on the resting EEG

The mean method was qualitatively compared to 3 offline methods, provided by an fMRI plug-in for the Matlab toolbox EEGLAB (fMRIB, University of Oxford Centre for Functional MRI of the Brain, Oxford, http://users.fmrib.ox.ac.uk/~rami/fmribplugin/), (Swartz Center for Computational Neuroscience University of California, San Diego, http://sccn.ucsd.edu/eeglab/).

The first method is the PCA based template subtraction (Niazy, Beckmann *et al.*, 2005). The fundamental procedure is to align all the pulse artifacts, in each EEG channel separately, in a matrix and perform a Principal Component Analysis (PCA) on the data. The first empirically defined number of PC's (the Optimal Basis Set) is then fitted to each artifact in that channel.

The residual two methods are based on the work of Allen et al. (Allen, Polizzi *et al.*, 1998). A template is generated within a window of 30 artifacts centred around the artifact at hand. The only difference between these two methods is the way the template is calculated. The *median method* builds an un-weighted median template, whereas the *Gaussian mean method* uses a mean template of Gauss-windowed artifact periods.

The number of principal components for the PCA based template subtraction method was empirically set to three after the observation of the signal envelopes of the filtered resting EEG data during an iterative increase of the PC number (see Figure 47).

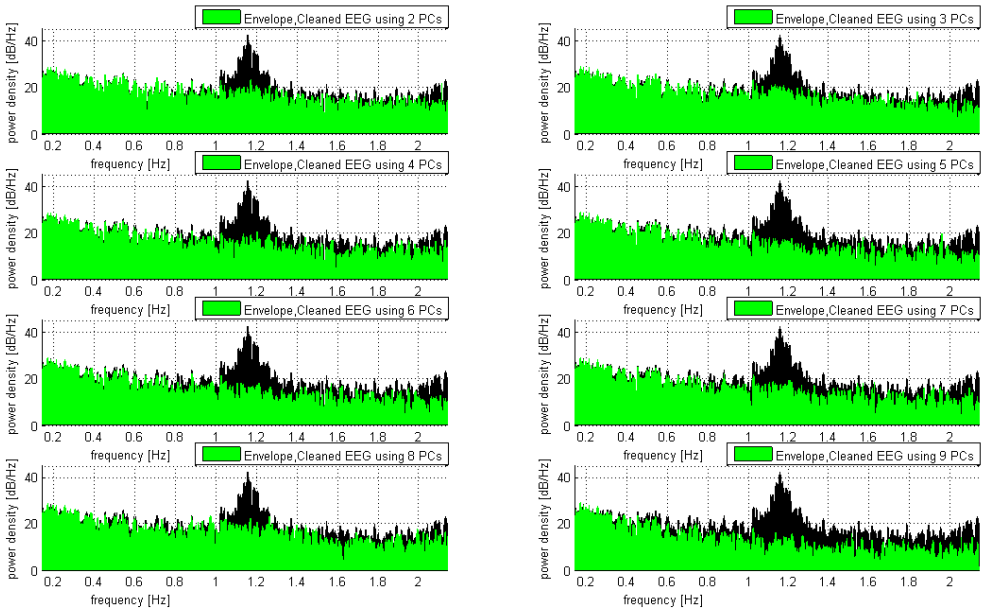

Figure 47: Power density envelope of the raw EEG signal (black). The envelopes after applying the PCA based filtering method with increased number of PC's illustrate the stepwise improvement of PA suppression.

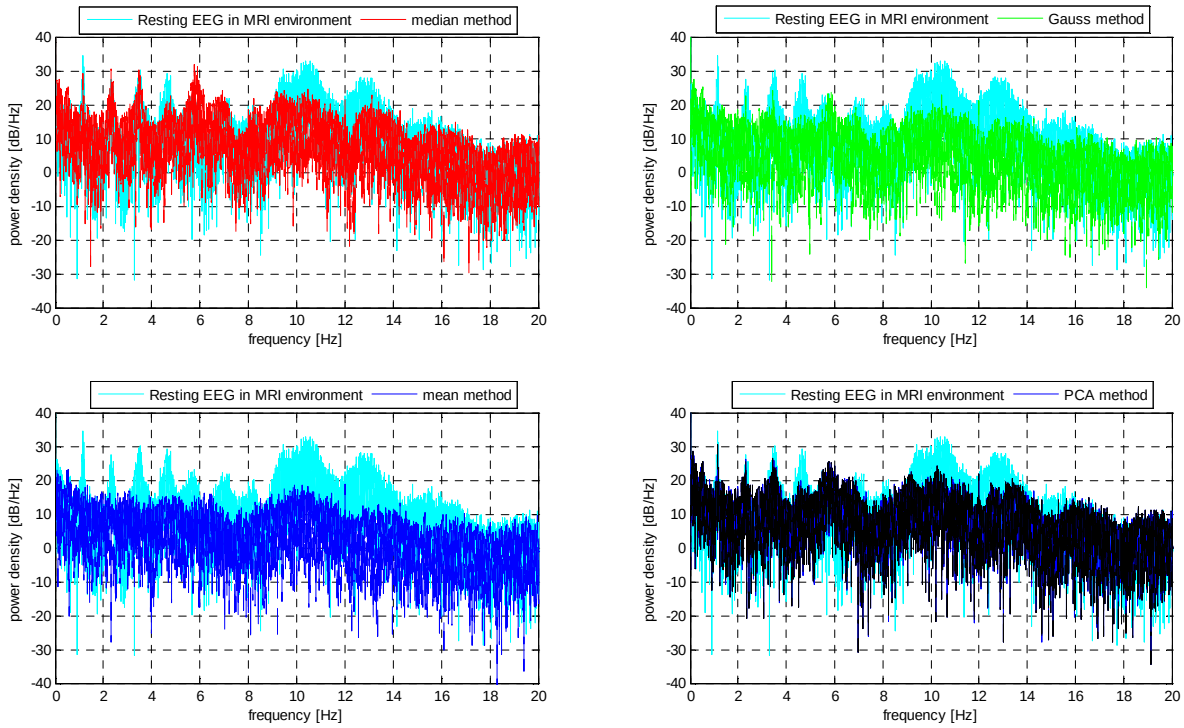

Figure 48: Power density functions after applying PA filtering methods on exemplary EEG channel

Through the visual evaluation of the power density function of the artifact cleaned EEG and the raw EEG, the mean method suppresses the PA harmonics best in comparison to the other methods over a wider frequency region (Figure 48).

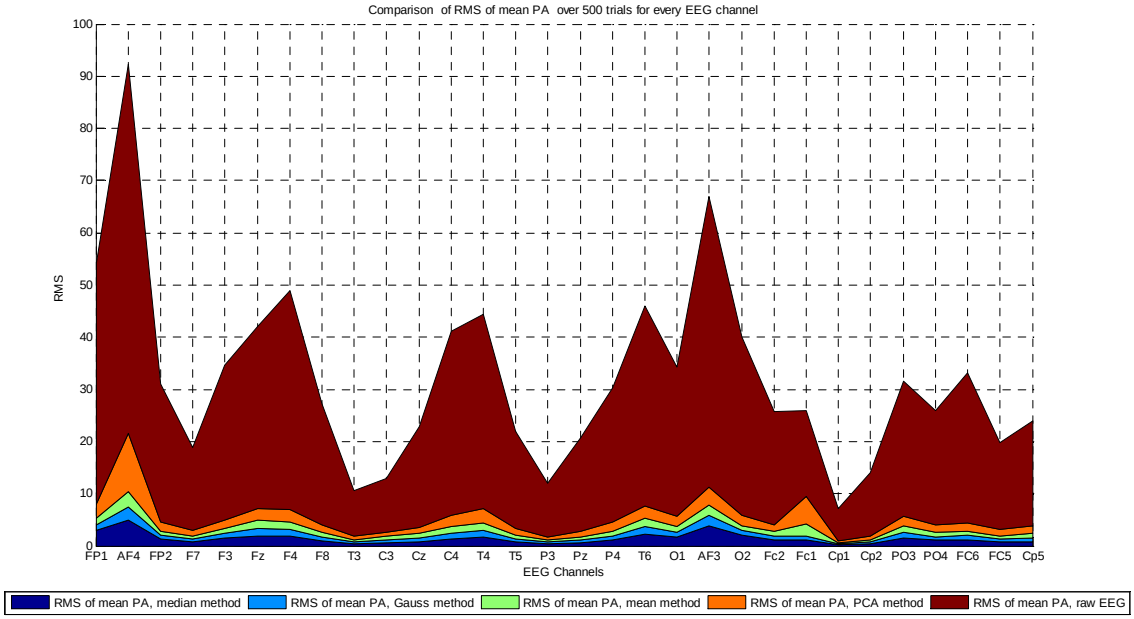

Figure 49: Root mean square (RMS) of the mean time course of PA compared to RMS of averaged artifact residuals after application of PA filtering methods, on all EEG channels over 500 trials.

The comparison of the RMS of the mean PA to the RMS of the mean artifact residuals after the application of all methods (see overview of stacked RMS values for all recorded EEG channels in Figure 49), reveals that the mean method and the gauss method result in better suppression performance than others.

Finally, the RINPS value, measured with a frequency window of 0.1 Hz of all PA harmonics up to 150 Hz, was calculated for every recorded EEG channel. In most channels, the mean method suppresses the majority of artifact residuals better than other methods.

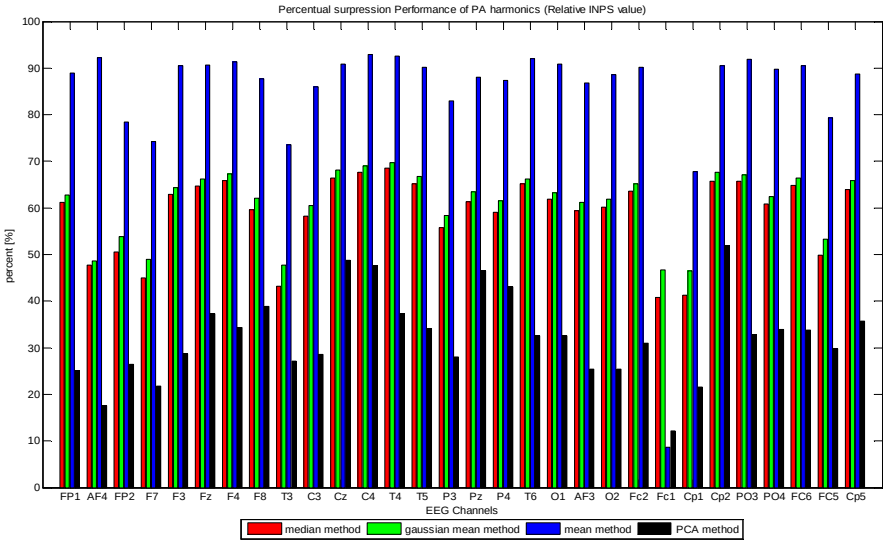

Figure 50: RINPS values of all PA filtering methods, calculated for all harmonics of the PA up to 150 Hz and all recorded channels separately.

As can be observed in Figure 45, the spectrum pulse related artifact is extended over a wide frequency region of the usable EEG signal. Consequently, the suppression of the PA is closely associated to loss of signal quality. In order to study these influences, defined evoked potentials were generated by means of the motor imagery BCI. By discussing the results of the signal quality, the time-frequency maps and the outcome of the classification, a good overview of artifact suppression performance can be given.

6.4 Setup for Motor imagery BCI

The discussed methods for MRI related artifact suppression should be tested on the motor imagery BCI, described in the chapter 3.3. (Page 9)

The functional activation has to be observed in the fMRI images as well, so the time duration of the BOLD answer has to be taken into consideration in the EEG based paradigm. In terms of fMRI image analysis, the goal is to achieve a noticeable contrast change between phases of

no motor imagery, left- and right hand imagination. For this the TR Trigger was used in order to time the three phases. The length of one trial was principally extended to 14 seconds as opposed to the initial 8 seconds. Although the BOLD response does not completely subside until after 15 seconds (chapter 4, page 17), the duration of the trial is kept as tight as possible in order to prevent fatigue. The TR trigger is selected with 2000 ms, so that 7 images are created during the 14 seconds of every trial. The final paradigm is depicted in Figure 51 together with the detailed MRI scanner settings. In order to initialize the imaging artifact filter, which needs at least 25 volumes for a sufficient imaging artifact suppression, and the pulse related artifact filter, witch needs about 20 seconds for initialization (10 seconds for collecting the PA's and approximately 8 seconds for initialization of the Peak detection), a waiting time of 40 volumes was set before the actual BCI experiment starts.

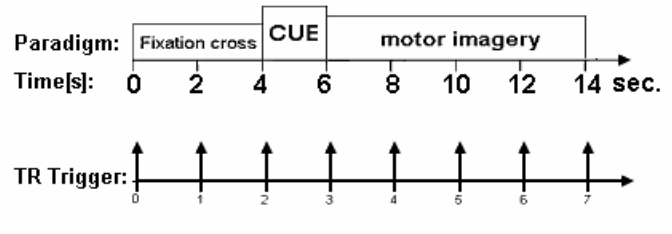

TR Time	2000 ms
Number of Slices	32
Slice Thickness	5 mm
Slice Gap	1 mm
TE Time	30 ms
Field of view (FOV)	192 mm x 192 mm
Matrix Size:	64x64

Figure 51: LEFT: Extended Motor imagery paradigm for combined EEG/fMRI measurement. RIGHT: Detailed MRI scanner settings for the fMRI measurement.

The originally used channels FC3/C3 and FC4/C4 were switched to FC5/C3 and FC2/C4 because of the channels FC3 and FC4 do not exist on the used MRI-save EEG electrode cap.

During the BCI experiment, all 32 EEG channels of a well trained, healthy test person was recorded. In order to find out if the BCI experiment works with the temporally extended paradigm and the switched EEG channels, a session of 40 trials was recorded outside the MRI environment without feedback and, subsequently, with feedback.

For a separate test of the imaging artifact filtering methods the data which was recorded outside the MRI surroundings was superimposed to a phantom data set (TR=3000 ms, 24 slices). Afterwards, the same BCI session was repeated in the MRI tube without the fMRI measurement, in order to study the filtering performance of the pulse related artifact filtering methods. The final execution of the first session and two further sessions with a different cue order during the application of the EPI sequence revealed the combined filtering performances. For a qualitative comparison the classification error time course (see chapter 3.3 on page 9) was investigated.

The measurement setup is the same as for the phantom tests (chapter 6.3.1.1, page 40), with the difference that the paradigm was presented to the test person with a video beamer, which projected onto a milk glass surface in the MRI bore. The paradigm is visualized by a mirror attachment on the RF coil (Figure 52). In order to ensure the full concentration of the test person during the MRI data acquisition earplugs were used.

Figure 52: MRI RF coil and mirror attachment, used for motor imagery BCI (Siemens, 2002)

7 Results

7.1 Measurements outside MRI environment

The execution of the BCI experiment outside the MRI environment is the qualitative reference for the measurements inside the MRI surroundings. It should reveal to what extent the test person is able to control the temporally extended BCI, for the aim of concurrent EEG/fMRI analysis and in which frequency regions whose ERD/ERS activities are. Therefore a session consisting of 40 trials was executed without feedback (training phase) and with feedback (feedback phase).

The time-frequency maps of the mean EEG signal during the imagination of the right hand in the training phase are shown in Figure 53. The respective mean brain activity of the left hand imagination is depicted in Figure 54.

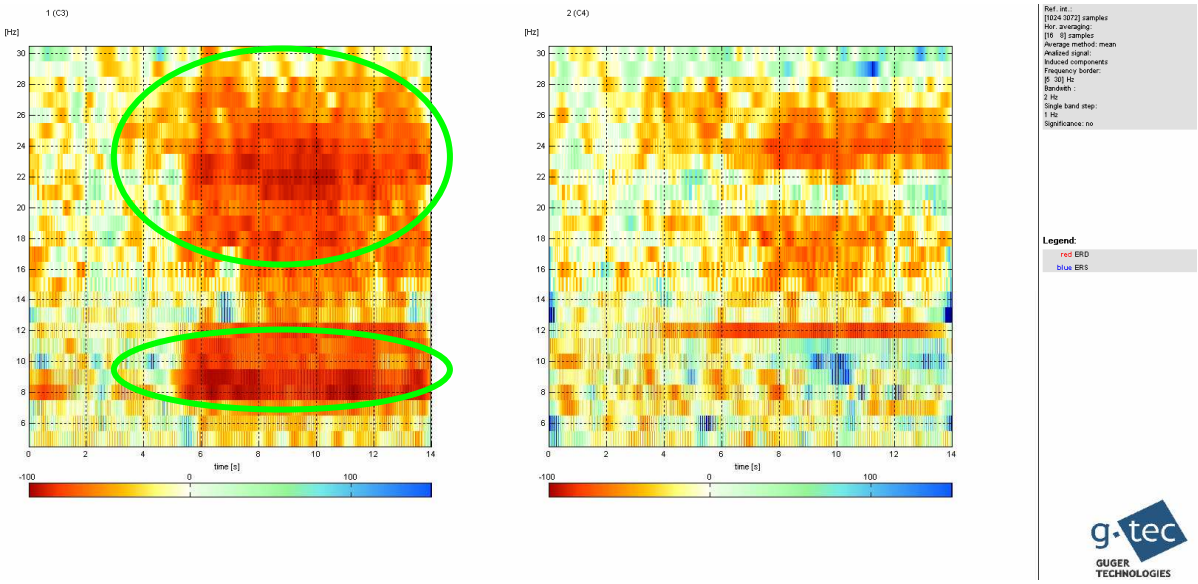

Figure 53: Time-frequency map on the channels C3 (left) and C4 (right) of imagination trials of the right hand. The active regions are marked with green circles. ERD (red)/ERS (blue).

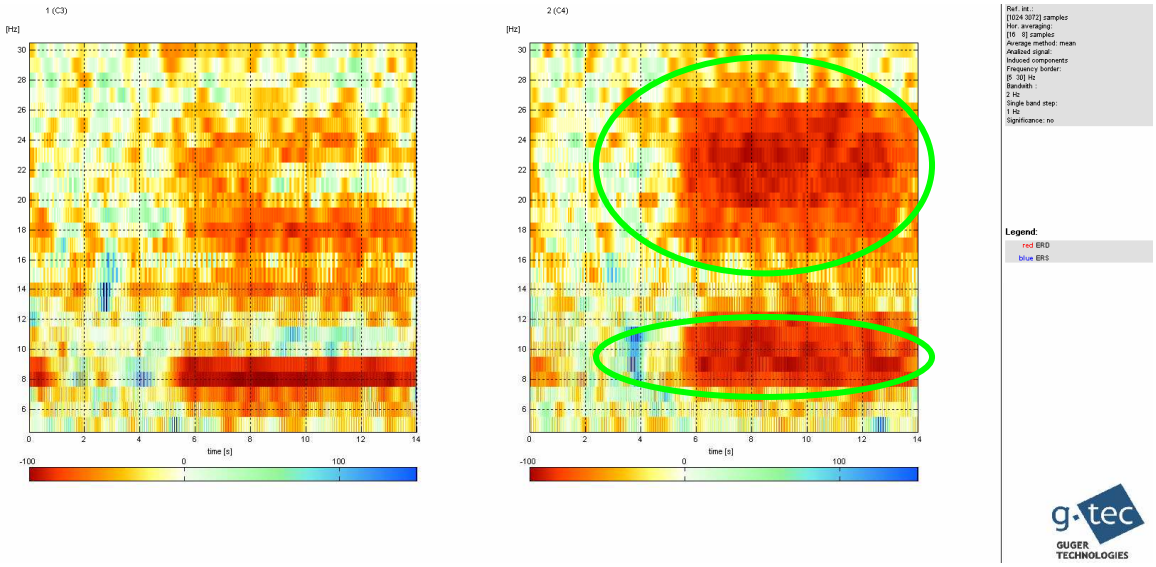

Figure 54: Time-frequency map on the channels C3 (left) and C4 (right) of imagination trials of the left hand. The active regions are marked with green circles. ERD (red)/ERS (blue).

By a visual inspection of the time frequency maps, it can be observed that the mean activation difference between the right EEG channel (C4) and the left EEG channel (C3) is located approximately in the frequency regions of 8-12 Hz and 18-26 Hz. These regions were consequently used for the training of the classifier.

Comparing the classification results during training and feedback (Figure 55) one finds a mean classification error of 7.88 % (training) and 4.62 % (feedback) over the imagination phase (second 6 to second 14).

Figure 55: Time courses of the classification error during the training session (red) and the feedback session (green). The dashed red line shows the ideal error time course (see chapter 3.3, page 9).

7.1.1 Filtering performance test of the volume based averaging method

Since the imaging artifact occurs only in combination with the pulse related artifact in the MRI environment, the EEG data outside of the MRI surroundings was overlaid with a synchronized phantom data set (TR=3000 ms, 24 Slices), and filtered again with (using) the volume based averaging method, in order to analyze the filtering performance of (only) the imaging artifact filtering method (alone).

Before the artifacts were superimposed to the clean EEG, the 50 Hz power frequency was suppressed with a 50 Hz 3rd-order Butterworth Notch filter and bandwidth limited to 0.5-30 Hz (3rd order, Butterworth band pass). After the filtering process the data was again band limited by a 0.5- 30 Hz band pass filter.

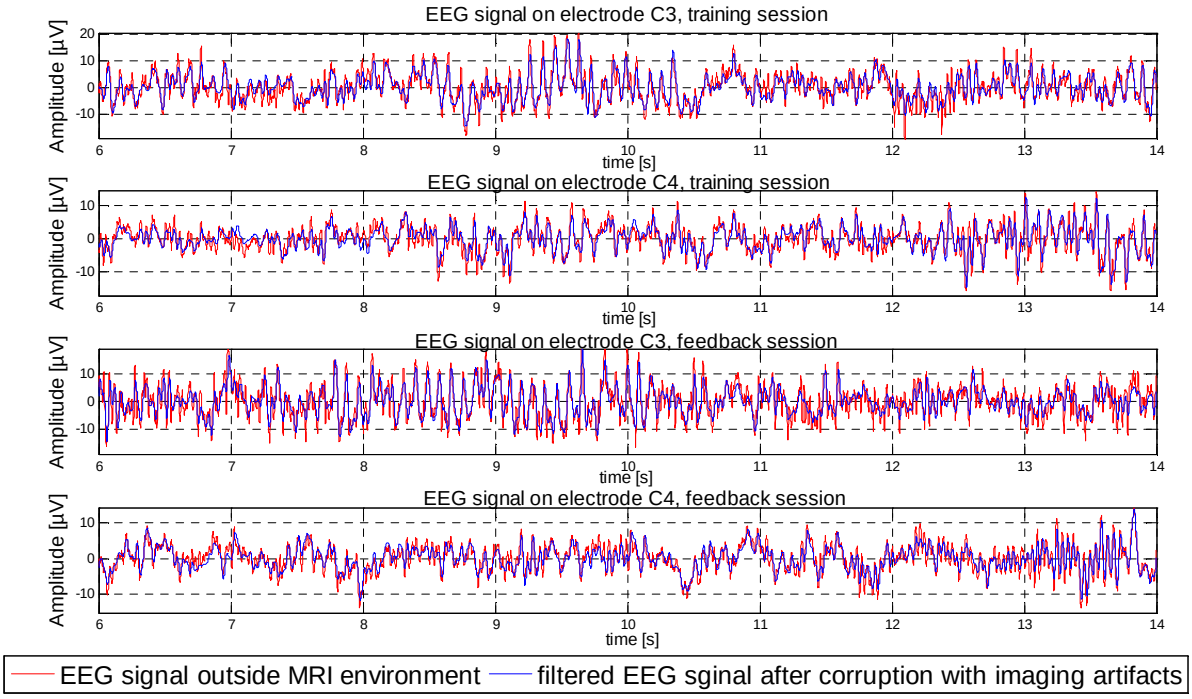

Figure 56: Imagination phase (6th to 14th sec.) of clean EEG data trials (red) of the training session (first two graphs) and the feedback session (second two graphs) in comparison to the imaging artifact freed data (blue) after imaging artifact corruption and consequential filtering.

The comparison of the imaging artifact free data, and the clean EEG in the time domain (Figure 56), shows a slightly different time course which impacts the classification result accordingly (Figure 57). The mean classification error of the training phase changes from 7.88 % to 6.54 % and the error of the feedback phase 4.62 % rises to 4.81 % within the imagination time (6th to 14th sec.).

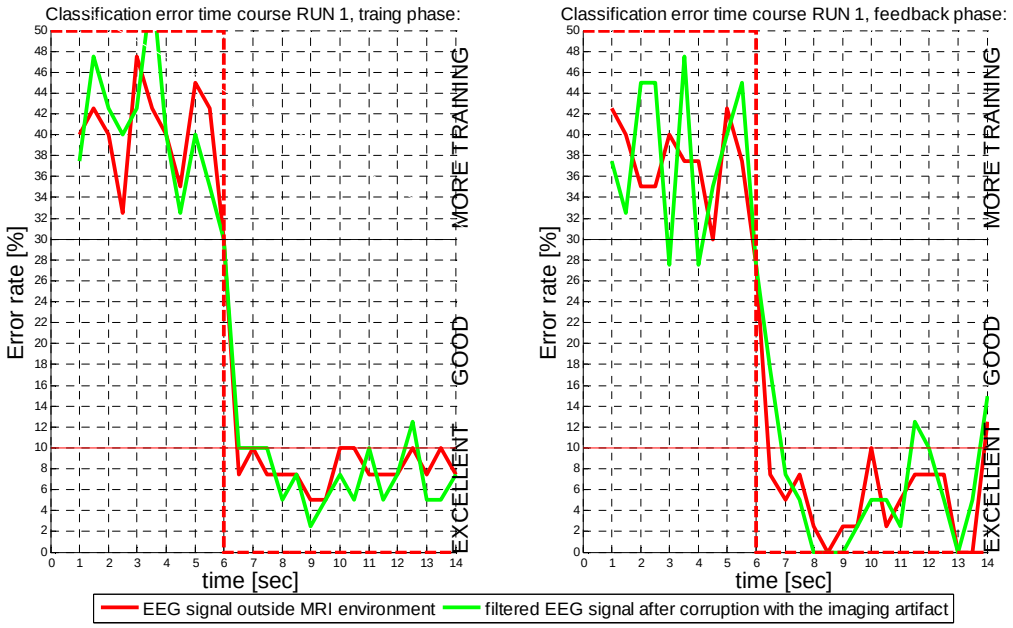

Figure 57: Classification error time course of clean data (red) and artifact free data (green). Left: training phase. Right: feedback phase.

7.2 Measurements in the MRI environment

7.2.1 Filtering performance test of the PA filtering methods

For a separate performance test of the pulse related artifact filtering methods, which are discussed in chapter 6.3.2.2 (page 52), a training session was performed inside of the MRI tube without any EPI sequence, with the same cue order as used for the experiment outside the MRI surroundings

The time frequency maps of the raw signal in Figure 58 and Figure 59 give prior information on the signal quality without filtering.

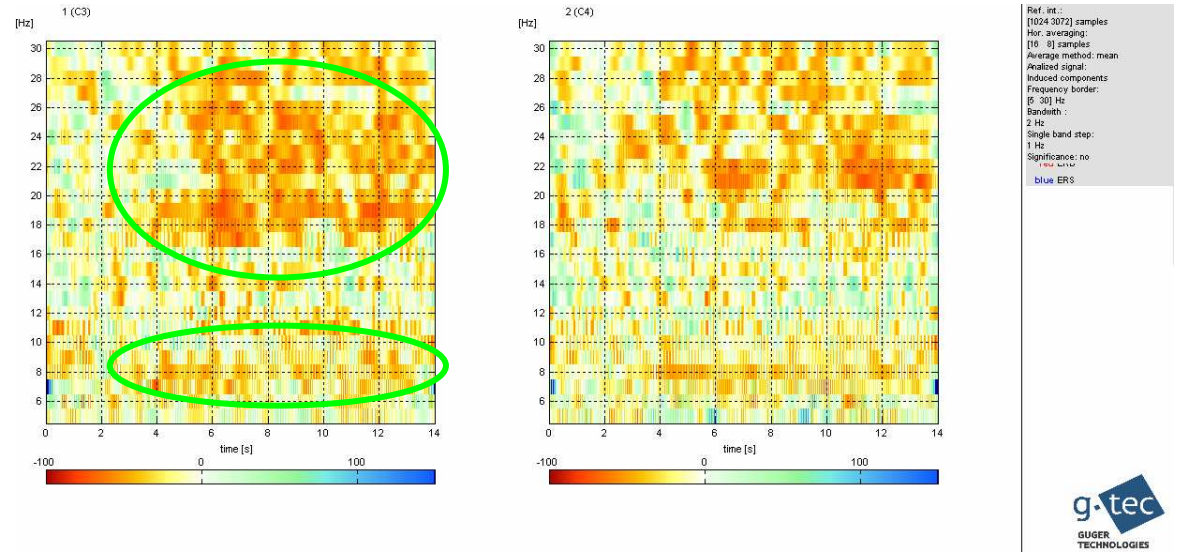

Figure 58: Time-frequency map on the channels C3 (left) and C4 (right) of imagination trials of the right hand. The active regions are marked with green circles. ERD (red)/ERS (blue).

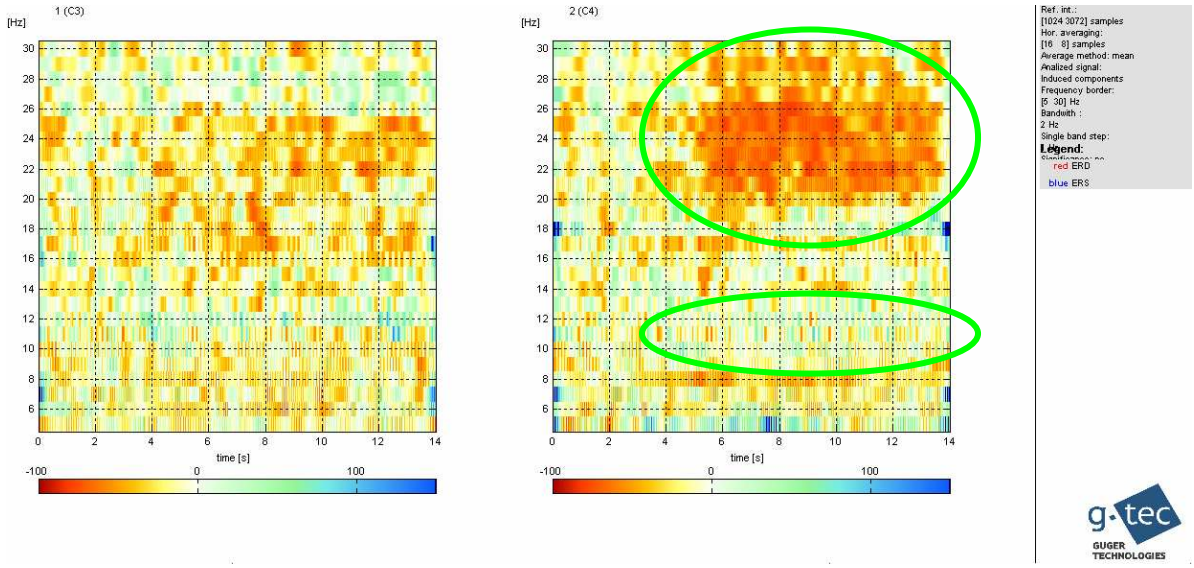

Figure 59: Time-frequency map on the channels C3 (left) and C4 (right) of imagination trials of the left hand. The active regions are marked with green circles. ERD (red)/ERS (blue).

By comparing the raw signal time frequency maps to the maps of the session outside the MRI (Figure 53and Figure 54), it becomes clear that the activation difference between the EEG channels of the raw signal is less distinct i.e. is missing completely in the frequency region of 8 to 12 Hz.

The comparison of the classification error of the raw data and the PA free data illustrate the impact of the BCC artifact removal methods on the classification outcome (Figure 60).

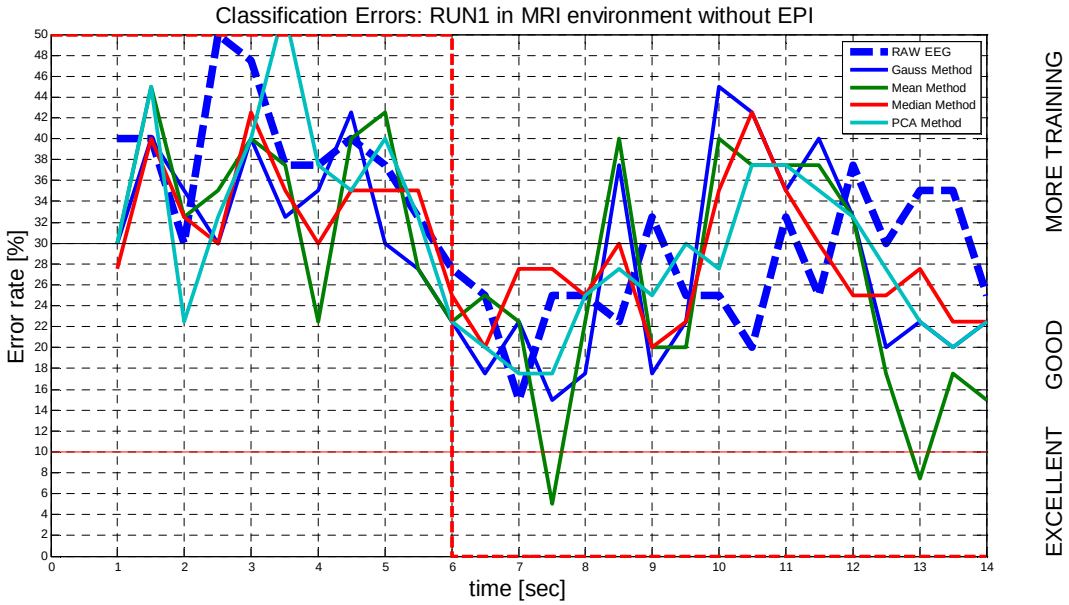

Figure 60: Time courses of the classification error of the raw EEG data (dashed blue) and the cleaned data after application of PA filtering methods

The very high mean classification error of 28.46 % of the raw signal, during the imagination phase, reflects the fact that the pulse related artifact strongly affects the useful EEG data. After the application of the filtering methods, the mean classification error changes to 28.85% (Gauss method), 26.54% (mean method), 27.88% (median method) and 28.46% (PCA method).

7.3 Combined EEG/fMRI measurement

For the final three combined BCI sessions during a concurrent fMRI record the application of all discussed imaging- (chapter 6.3.1.2, page 46) and pulse related artifact filtering methods (chapter 6.3.2.2, page 52) should reveal the impact of data separability. The evaluation of the fMRI images should provide additional information on the concentration level of the test person during the BCI experiment execution.

7.3.1 EEG results

After the application of the IA and the PA filters the classification error time courses of all three runs (Figure 61) show a consistent drop at defined time points (sec. 7 at run 1, sec. 7 at run 2, sec. 11 at run 3), but the characteristical drop of the classification error over the whole imagination phase (6^{th} to 14^{th} sec.) can't be observed in any of the evaluated comparisons.

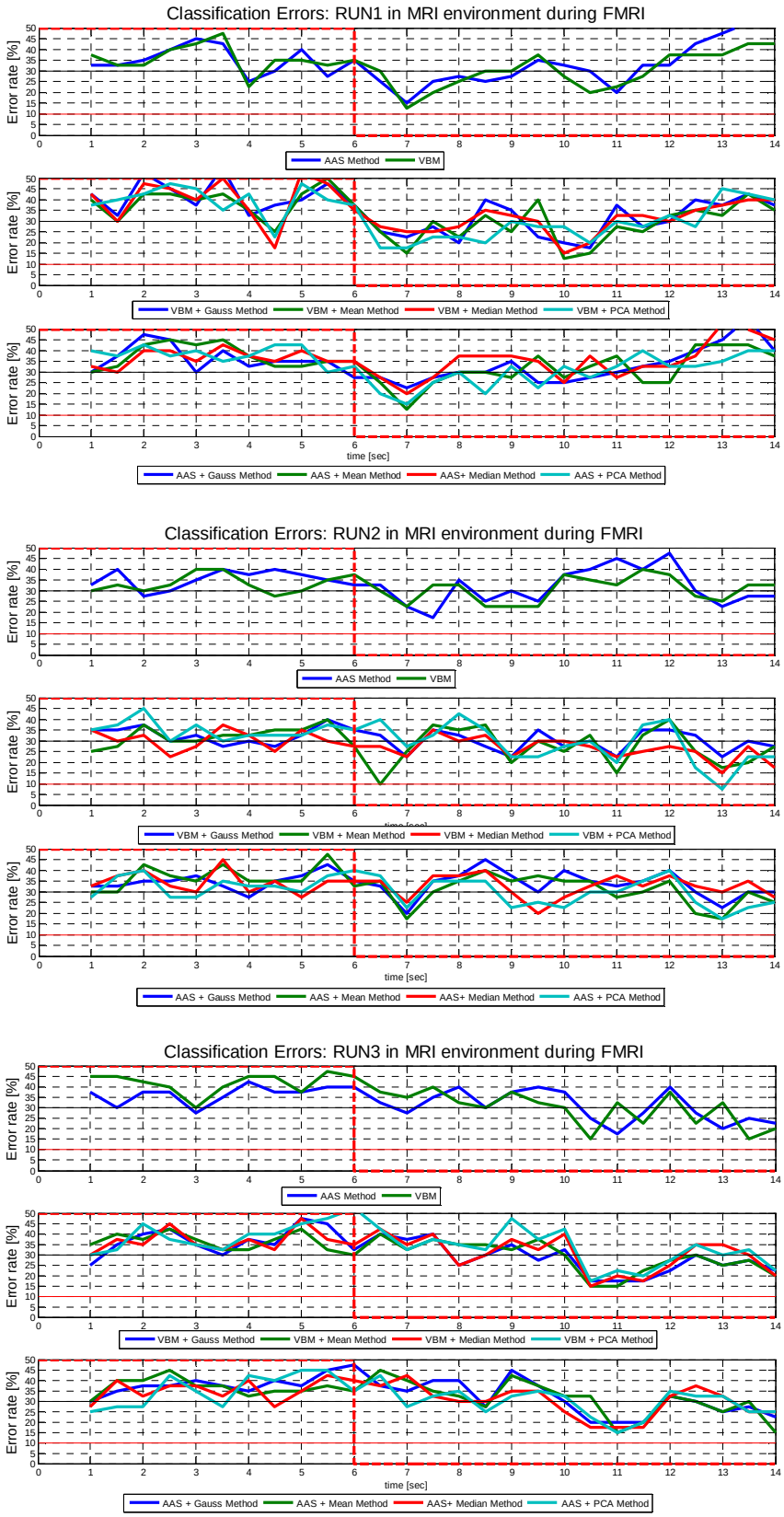

Figure 61: Time courses of the classification error of all three BCI sessions during concurrent fMRI measurement. The first graph of each run shows the classification error after the application of the imaging artifact suppression methods. The second and the third graphs show the error time course after combined application of the imaging artifact filtering methods and the pulse artifact filtering methods. It can be noticed that after the combined application of the filtering methods the classification error falls only at specific time points in the imagination phase (6th to 14th sec.).

The mean classification errors during the imagination phase (6th to 14th sec.) are summed up in Table 1.

	Mean classification error during imagination phase [%]		
Methods	**RUN 1**	**RUN 2**	**RUN 3**
AAS	35.2	33.3	30.0
VBA	32.1	30.8	27.7
AAS+ Gauss	34.6	34.2	29.0
AAS+ Mean	33.7	**31.0**	28.7
AAS+ Median	**37.5**	32.3	27.7
AAS+PCA	32.1	28.1	28.3
VBM+ Gauss	31.3	29.2	**25.4**
VBM+ Mean	**29.1**	27.5	27.1
VBM+ Median	31.3	**25.6**	27.9
VBM+PCA	30.2	26.7	**31.0**

Table 1: Mean classification errors of all BCI sessions during the concurrent EEG/fMRI recording, after application of all imaging- and pulse related artifact suppression methods.

7.3.2 fMRI results

The central expectations of the analysis of the MRI images were to observe the brain activity in the motor cortex laterally reversed to the arrow directions presented in the BCI paradigm. For this purpose three contrast conditions were introduced. The first contrast results from a comparison of the images during the passive and the images during the active imagination phase. The second and the third contrast result from the comparison of the right to left and left to right imagination phases. The significance of greyscale levels and the visualization of the results were calculated with SPM (chapter 4.2, page 20). The p-value (significance threshold) of the voxel-wise t-test was set to 0,001. The coordinates of the activations were labeled to the functional areas according to the Talairach atlas with the freeware tool AAL (chapter 4.2, page 20).

Figure 62 shows the functional activations of the first run projected on a standard 3D brain template. It is striking that the activations left, right and base can be clearly separated spatially. The anatomical association of the activities in the active phases can be assigned according to the above mentioned exception to the right respective left motor cortex (see a detailed summary in appendix chapter 9.1 on page 75).The images of the passive phase show a weak activity in the occipital brain area, which is the visual processing centre of the human brain.

RUN 1

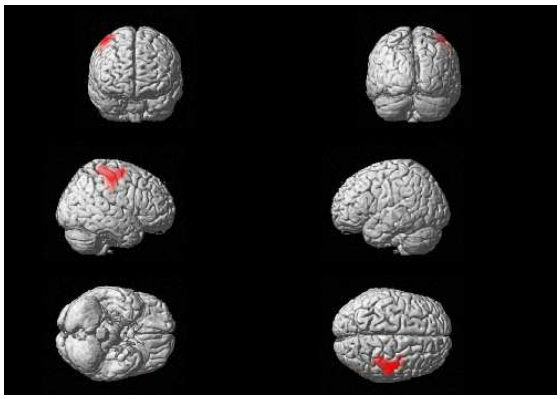

left hand imagination phase

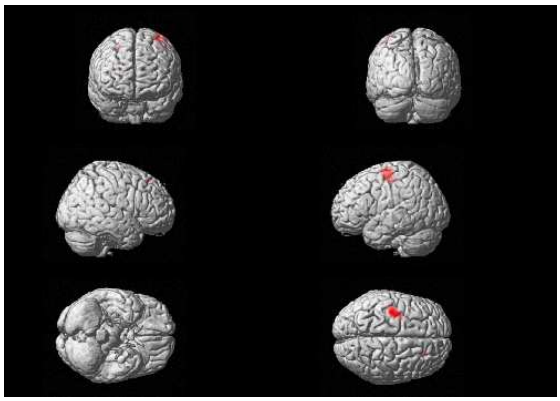

right hand imagination phase

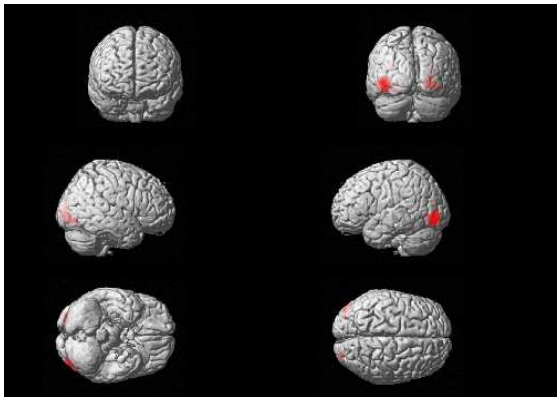

No motor imagination (base)

Figure 62: Functional activations of left hand imagination phase (top left), right hand imagination (top right) and base (bottom) of RUN 1, projected on the standard SPM brain template.
TOP LEFT: Biggest cluster level is extended over the right motor cortex
(detailed labels in appendix 9.1.1, Figure 65)
TOP RIGHT: Less distinct then the left hand activation over the left motor cortex
(detailed labels in appendix 9.1.2, Figure 66)
BOTTOM: images without any motor activations show activities in the occipital cortex (detailed labels in appendix 9.1.3, Figure 67)

A similar image emerges after an observation of run two (Figure 63) with the difference that the left hand imagination phase can't be separated from the baseline that well as in run one. In the end the left hand activation in run three is reduced exclusively to the occipital area (Figure 64). This can most likely be explained by a diminishing concentration over time (Detailed anatomical labels of run two in appendix 9.2 on page 78, respectively of run three in appendix chapter 9.3 on page 80).

RUN 2

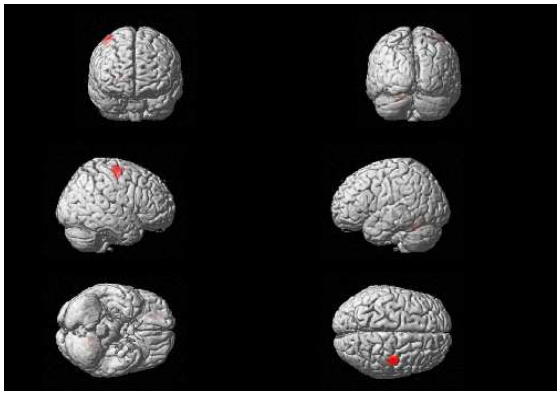

left hand imagination phase

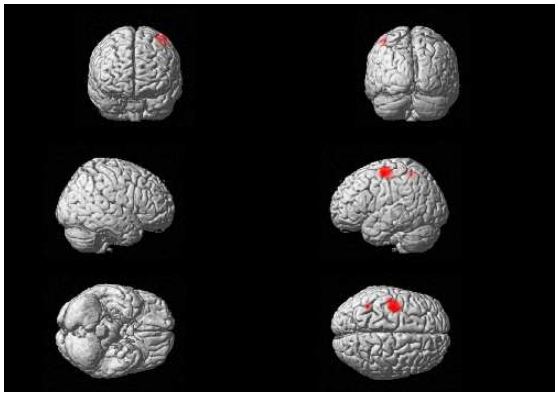

right hand imagination phase

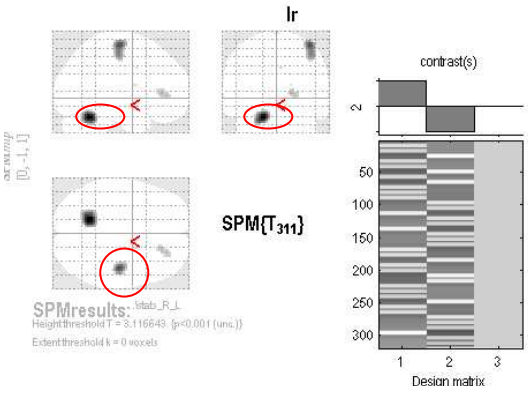

Figure 63: Functional activations of left hand imagination phase (top left), right hand imagination (top right) of RUN 2, projected on the standard SPM brain template. The bottom figure illustrates an additional activation in the occipital area during the left hand imagination phase (red mark on the glass brain).
<u>TOP LEFT:</u> Biggest cluster level is extended over the occipital area (detailed labels in appendix 9.2.1, Figure 68). Additionally a weak activation on the right motor cortex can be noticed.
<u>TOP RIGHT:</u> Strongest activation over the left motor cortex
(detailed labels in appendix 9.2.2, Figure 69)

RUN 3	
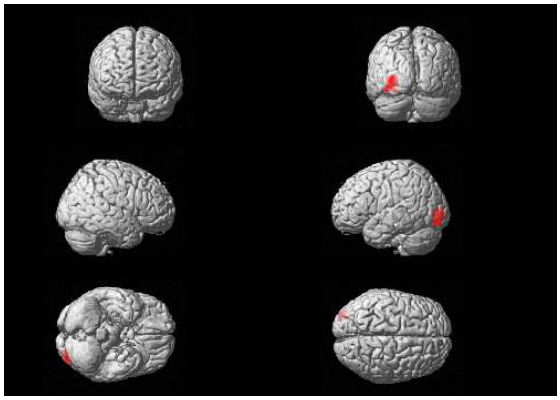	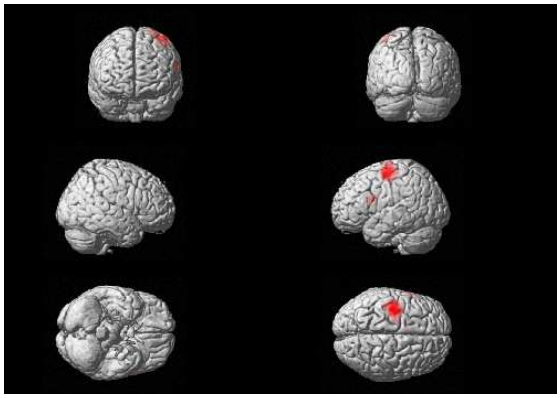
left hand imagination phase	right hand imagination phase
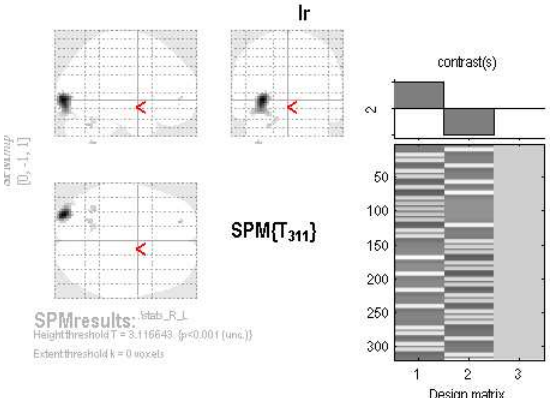	**Figure 64: Functional activations of left hand imagination phase (top left), right hand imagination (top right) of RUN 3, projected on the standard SPM brain template. The bottom figure shows that the activation during the left hand imagination is reduced exclusively to the occipital area.** **<u>TOP LEFT:</u> Biggest cluster level is extended over the occipital area (detailed labels in appendix 9.3.1, Figure 70).** **<u>TOP RIGHT:</u> Strongest activation over the left motor cortex** **(detailed labels in appendix 9.3.2, Figure 71)**

8 Discussion

The operation of EEG based brain computer interfaces in MRI environment is restricted by massive artifacts occurring from electromagnetic coupling of magnetic coils and the EEG electrodes. In order to ensure a closed interaction between the test person and the paradigm, the feedback signal has to be cleaned from artifacts in real-time.

In the course of this thesis, two types of artifacts were treated. The first artifact (imaging artifact) emerges due to the periodically switching magnetic fields during the MR imaging sequences. Under the condition of a periodic occurrence of the imaging artifact, a template based filtering method can be used for suppression in real-time. Phantom measurements showed that the artifact periodicity can be ensured to a certain extent if the ratio of repetition time and number of slices is set to an integer value of sampling time points of the EEG amplifier. The independent test of this method was carried out by superimposition of corrupted phantom data, with clean EEG data of a motor imagery BCI experiment and subsequent filtering. The results showed only marginal quality losses in comparison to the clean EEG signal course.

The second artifact is called pulse related artifact and occurs with the rhythmic electrode movements resulting from respiration and blood flow. The strong time course fluctuations, and the difficulty to capture the exact signal period and the time of occurrence of this artifact, are the main factors which hamper the filtering process. The BCI measurements in MRI environment without image acquisition showed that the useful signal is almost entirely destroyed by the pulse related artifact. The artifact suppression methods presented in this thesis showed that the reduction of the PA is strongly connected to the loss of the useful signal, which makes a linear classification of EEG data rarely impossible. Additionally, it can be said that the choice of artifact samples for the filtering template is not trivial, and only an offline evaluation of the artifact time course leads to optimal filtering settings. The very limited suppression effect of template based methods raise the question if a systematic suppression of electrode movements by fixing the brain with vacuum pillows would give better results.

The evaluation of the fMRI images support the assumption that the BCI experiment was successful and led to noticeable brain activations in the theoretically assumed brain regions.

ALLEN; P. A Method for Removing Imaging Artifact from Continuous EEG Recorded during Functional MRI. *Neuroimage* [S.I.], v. 12, n. 2, p. 230-239, 2000.

ALLEN, P. J. *et al.* Identification of EEG events in the MR scanner: the problem of pulse artifact and a method for its subtraction. *Neuroimage* [S.I.], v. 8, n. 3, p. 229-39, Oct 1998.

BENAR, C. *et al.* Quality of EEG in simultaneous EEG-fMRI for epilepsy. *Clinical Neurophysiology* [S.I.], v. 114, n. 3, p. 569-580, 2003.

BONMASSAR, G. *et al.* Motion and Ballistocardiogram Artifact Removal for Interleaved Recording of EEG and EPs during MRI. *Neuroimage* [S.I.], v. 16, n. 4, p. 1127-1141, 2002.

BRISELLI, E. *et al.* An independent component analysis-based approach on ballistocardiogram artifact removing. *Magnetic Resonance Imaging* [S.I.], v. 24, n. 4, p. 393-400, 2006.

CARIA, A. *et al.* Regulation of anterior insular cortex activity using real-time fMRI. *Neuroimage* [S.I.], v. 35, n. 3, p. 1238-1246, 2007.

CENTER-FOR-INTEGRATING-RESEARCH-&-LEARNING. http://www.magnet.fsu.edu/education/tutorials/magnetacademy/mri/images/mri-scanner.jpg. Kristen Coyne, 2010.

DEBENER, S. *et al.* Properties of the ballistocardiogram artefact as revealed by EEG recordings at 1.5, 3 and 7 T static magnetic field strength. *International Journal of Psychophysiology* [S.I.], v. 67, n. 3, p. 189-199, 2008.

DEPARTMENT OF BIOMEDICAL ENGINEERING NITRO LAB, U. O. W.-M. http://nitrolab.engr.wisc.edu/images/BCIoverview1.png. 2010.

DUDA, R. *et al. Pattern Classification (2nd Edition)*. Wiley-Interscience, 2000.

ELLINGSON, M. L. *et al.* Ballistocardiogram artifact reduction in the simultaneous acquisition of auditory ERPS and fMRI. *Neuroimage* [S.I.], v. 22, n. 4, p. 1534-1542, 2004.

FARWELL, L. A.; DONCHIN, E. Talking off the top of your head: toward a mental prosthesis utilizing event-related brain potentials. *Electroencephalography and Clinical Neurophysiology* [S.I.], v. 70, n. 6, p. 510-523, 1988.

G.TEC-MEDICAL-ENGINEERING-GMBH, G. Motor Imagery BCI www.gtec.at. 2009.

GARREFFA, G. *et al.* Real-time MR artifacts filtering during continuous EEG/fMRI acquisition. *Magnetic Resonance Imaging* [S.I.], v. 21, n. 10, p. 1175-1189, 2003.

GOLDMAN, R. I. *et al.* Acquiring simultaneous EEG and functional MRI. *Clinical Neurophysiology* [S.I.], v. 111, n. 11, p. 1974-1980, 2000.

GONCALVES, S. I. *et al.* Correction for desynchronization of EEG and fMRI clocks through data interpolation optimizes artifact reduction. In: Engineering in Medicine and Biology Society, 2007. EMBS 2007. 29th Annual International Conference of the IEEE. 2007. p.1590-1594. Disponível em:<10.1109/IEMBS.2007.4352609>. Acesso em.

GONÇALVES, S. I. *et al.* Artifact removal in co-registered EEG/fMRI by selective average subtraction. *Clinical Neurophysiology* [S.I.], v. 118, n. 11, p. 2437-2450, 2007.

GROUILLER, F. *et al.* A comparative study of different artefact removal algorithms for EEG signals acquired during functional MRI. *Neuroimage* [S.I.], v. 38, n. 1, p. 124-137, 2007.

GUGER, C. *et al.* How many people are able to operate an EEG-based brain-computer interface (BCI)? *Neural Systems and Rehabilitation Engineering, IEEE Transactions on* [S.I.], v. 11, n. 2, p. 145-147, 2003.

HILL, R. A. *et al.* EEG during MR imaging: Differentiation of movement artifact from paroxysmal cortical activity. *Neurology* [S.I.], v. 45, n. 10, p. 1942, 1995.

HINTERBERGER, T. *et al.* Brain-computer communication and slow cortical potentials. *Biomedical Engineering, IEEE Transactions on* [S.I.], v. 51, n. 6, p. 1011-1018, 2004.

HOFFMANN, A. *et al.* Electroencephalography during functional echo-planar imaging: Detection of epileptic spikes using post-processing methods. *Magn. Reson. Med.* [S.I.], v. 44, n. 5, p. 791-798, 2000.

HYVÄRINEN, A. Fast and Robust Fixed-Point Algorithms for Independent Component Analysis. 1999.

IN, M. H. *et al.* Ballistocardiogram artifact removal from EEG signals using adaptive filtering of EOG signals. *Physiological Measurement* [S.I.], v. 27, n. 11, p. 1227-1240, 2006.

IVES, J. R. *et al.* Monitoring the patient's EEG during echo planar MRI. *Electroencephalography and Clinical Neurophysiology* [S.I.], v. 87, n. 6, p. 417-420, 1993.

JOLLIFFE, I. T. *Principal Component Analysis*. Springer, 2002.

KAPER, M. *P300-based brain-computer interfacing*. (2006). (Dr.) - AG Neuroinformatik -- Technische Fakultät (Bereich Informatik), Universität Bielefeld, Bielefeld, 2006.

KIM, K. H. *et al.* Improved ballistocardiac artifact removal from the electroencephalogram recorded in fMRI. *Journal of Neuroscience Methods* [S.I.], v. 135, n. 1-2, p. 193-203, 2004.

KLEM, G. H. *et al.* The ten-twenty electrode system of the International Federation. The International Federation of Clinical Neurophysiology. *Electroencephalogr Clin Neurophysiol Suppl* [S.I.], v. 52, p. 3-6, 1999.

KÜBLER, A. *et al.* The thought translation device: a neurophysiological approach to communication in total motor paralysis. Konstanz: Bibliothek der Universität Konstanz, 2007. (First publ. in: Experimental brain research 124 (1999), pp. 223-232).

LABORATORY OF BRAIN-COMPUTER INTERFACES. http://bci.tugraz.at/brunner/IVM/IVM06.pdf. In: MENSCHEN, I. I. (Ed.). Graz: Clemens Brunner.

LAZEYRAS, F. *et al.* Functional MRI with simultaneous EEG recording: Feasibility and application to motor and visual activation. *Journal of Magnetic Resonance Imaging* [S.I.], v. 13, n. 6, p. 943-948, 2001.

LEMIEUX, L. *et al.* Methodological Issues in EEG-correlated Functional MRI Experiments. *INTERNATIONAL JOURNAL OF BIOELECTROMAGNETISM* [S.I.], v. 1, p. 9, 1999.

LYTTON, W. W. *From computer to brain: foundations of computational neuroscience*. Berlin: Springer, 2002.

MALMIVUO, J.; PLONSEY, R. *Bioelectromagnetism : Principles and Applications of Bioelectric and Biomagnetic Fields*. Oxford University Press, USA, 1995.

MANDELKOW, H. *Commbining EEG and MRI for the purpose of imaging neuronal currents in humans.* (2009). 79 f. - Swiss Federal Institute of Technology, Eidgenössische Technische Hochschule Zürich, Zürich, 2009.

MANDELKOW, H. *et al.* Synchronization facilitates removal of MRI artefacts from concurrent EEG recordings and increases usable bandwidth. *Neuroimage* [S.I.], v. 32, n. 3, p. 1120-1126, 2006.

MANTINI, D. *et al.* Complete artifact removal for EEG recorded during continuous fMRI using independent component analysis. *Neuroimage* [S.I.], v. 34, n. 2, p. 598-607, 2007.

MASTERTON, R. A. J. *et al.* Measurement and reduction of motion and ballistocardiogram artefacts from simultaneous EEG and fMRI recordings. *Neuroimage* [S.I.], v. 37, n. 1, p. 202-211, 2007.

MATLAB. Natick, Massachusetts: The MathWorks Inc., 2003.

MATSUDA, T. *et al.* Simultaneous recording of EEG and functional MRI. *International Congress Series* [S.I.], v. 1232, p. 351-355, 2002.

MICROMED_S.P.A., M. V. Cablatura Cuffia-1. In: CUFFIA-1.PDF, C. (Ed.)2009.

MILNIK, V. Anleitung zur Elektrodenplatzierung des internationalen 10-20-Systems. *Das Neurophysiologie-Labor* [S.I.], v. 31, n. 1, p. 1-35, 2009.

MRC COGNITIONAND BRAIN SCIENCES UNIT CAMBRIDGE. http://imaging.mrc-cbu.cam.ac.uk/images/acline.gif. In: ACLINE.GIF (Ed.): Brett, Matthew, 2006.

MULERT, C.; LEMIEUX, L. *EEG-fMRI: Physiological Basis, Technique and Applications*. 1. ed. Berlin: Springer-Verlag, Berlin Heidlberg, 2010.

MÜRI, R. M. *et al.* ecording of electrical brain activity in a magnetic resonance environment: Distorting effects of the static magnetic field. *Magnetic Resonance in Medicine* [S.I.], v. 39, n. 1, p. 22, 1998.

MÜRI, R. M. *et al.* Recording of electrical brain activity in a magnetic resonance environment: Distorting effects of the static magnetic field. *Magnetic Resonance in Medicine* [S.I.], v. 39, n. 1, p. 18-22, 1998.

NEGISHI, M. *et al.* Removal of time-varying gradient artifacts from EEG data acquired during continuous fMRI. *Clinical Neurophysiology* [S.I.], v. 115, n. 9, p. 2181-2192, 2004.

NEUDÖRFLER, B. *EEG-Fibel Das EEG in der ärztlichen Praxis*. 5. ed. München: Urban Fischer, 2002.

NIAZY, R. K. *et al.* Removal of FMRI environment artifacts from EEG data using optimal basis sets. *Neuroimage* [S.I.], v. 28, n. 3, p. 720-737, 2005.

NIEDERMEYER, E. D. S., FERNANDO LOPES. *Electroencephalography: Basic Principles, Clinical Applications, and Related Fields*. 5. ed.: LIPPINCOTT RAVEN, 2004.

PFURTSCHELLER, G. Functional brain imaging based on ERD/ERS. *Vision Research* [S.I.], v. 41, n. 10-11, p. 1257-1260, 2001.

PFURTSCHELLER, G.; NEUPER, C. Motor imagery and direct brain-computer communication. *Proceedings of the IEEE* [S.I.], v. 89, n. 7, p. 1123-1134, 2001.

RYALI, S. *et al.* Development, validation, and comparison of ICA-based gradient artifact reduction algorithms for simultaneous EEG-spiral in/out and echo-planar fMRI recordings. *Neuroimage* [S.I.], v. 48, n. 2, p. 348-361, 2009.

SCHANDRY, R. *Biologische Psychologie*. 2. ed.: Beltz, 2006.

SCOTT H. FARO, F. B. M. *BOLD fMRI: A Guide to Functional Imaging for Neuroscientists*. Berlin: Springer, 2010.

SIEMENS. *Application Guide MAGNETOM TRIO*. 2002.

SIJBERS, J. *et al.* Restoration of MR-induced artifacts in simultaneously recorded MR/EEG data. *Magnetic Resonance Imaging* [S.I.], v. 17, n. 9, p. 1383-1391, 1999.

SIJBERS, J. *et al.* Reduction of ECG and gradient related artifacts in simultaneously recorded human EEG/MRI data. *Magnetic Resonance Imaging* [S.I.], v. 18, n. 7, p. 881-886, 2000.

SKRANDIES, W. Global field power and topographic similarity. *Brain Topography* [S.I.], v. 3, n. 1, p. 137-141-141, 1990.

SRIVASTAVA, G. *et al.* ICA-based procedures for removing ballistocardiogram artifacts from EEG data acquired in the MRI scanner. *Neuroimage* [S.I.], v. 24, n. 1, p. 50-60, 2005.

STRIK, W. K.; LEHMANN, D. Data-determined window size and space-oriented segmentation of spontaneous EEG map series. *Electroencephalography and Clinical Neurophysiology* [S.I.], v. 87, n. 4, p. 169-174, 1993.

SUN, L. *Simultaneous recording of EEG and fMRI: New approach to remove gradient and ballistocardiogram EEG-artifacts*. (2009). 123 f. (Dr.) - Fakultät für Elektrotechnik und Informationstechnik, Otto-von-Guericke-Universität Magdeburg, Magdeburg, 2009.

TONG, S. *et al.* Removal of ECG interference from the EEG recordings in small animals using independent component analysis. *Journal of Neuroscience Methods* [S.I.], v. 108, n. 1, p. 11-17, 2001.

UNIVERSITY HOSPITALS OF CLEVELAND. http://www.epilepsy.uhhs.com/_borders/brain.1.jpg. 2005.

VINCENT, J. L. *et al.* Moving GLM ballistocardiogram artifact reduction for EEG acquired simultaneously with fMRI. *Clinical Neurophysiology* [S.I.], v. 118, n. 5, p. 981-998, 2007.

WALTER, D. M. D. P. H. *Funktionelle Bildgebung in Psychiatrie und Psychotherapie, Methodische Grundlagen und klinische Anwendungen*. 1. ed.: Schattauer GmbH, 2005.

WAN, X. *et al.* Artifact reduction for simultaneous EEG/fMRI recording: Adaptive FIR reduction of imaging artifacts. *Clinical Neurophysiology* [S.I.], v. 117, n. 3, p. 681-692, 2006.

WELCH, P. The use of fast Fourier transform for the estimation of power spectra: A method based on time averaging over short, modified periodograms. *Audio and Electroacoustics, IEEE Transactions on* [S.I.], v. 15, n. 2, p. 70-73, 1967.

WOLPAW, J. R. *et al.* Brain-computer interfaces for communication and control. *Clinical Neurophysiology* [S.I.], v. 113, n. 6, p. 767-791, 2002.

YE, N. The Handbook of Data Mining. v. 1: Lawrence Erlbaum Assoc Inc, 2004. p. 720.

9 Appendix

9.1 SPM fMRI results RUN 1

9.1.1 Left hand imagination

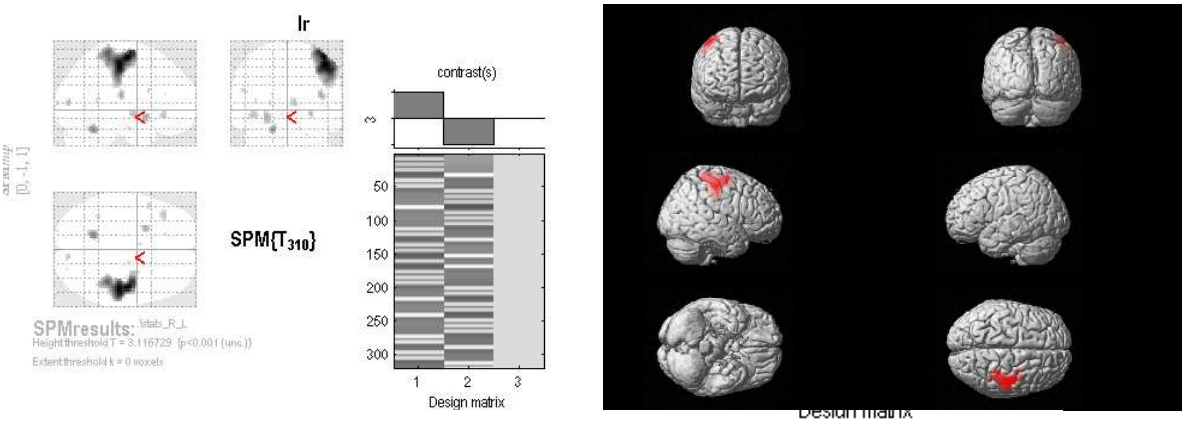

Statistics: *p-values adjusted for search volume*

set-level		cluster-level				peak-level					mm mm mm		
p	c	$p_{FWE\text{-}corr}$	$q_{FDR\text{-}corr}$	k_E	p_{uncorr}	$p_{FWE\text{-}corr}$	$q_{FDR\text{-}corr}$	T	(Z=)	p_{uncorr}			
0.257	14	0.000	0.000	727	0.000	0.000	0.000	7.05	6.79	0.000	45	-10	64
						0.000	0.000	6.89	6.64	0.000	48	-22	55
						0.008	0.004	5.21	5.10	0.000	39	-37	67
		0.351	0.177	29	0.038	0.073	0.023	4.69	4.60	0.000	-18	-52	-23
		0.471	0.195	24	0.056	0.547	0.197	4.05	3.99	0.000	42	-19	16
		0.275	0.177	33	0.028	0.619	0.206	3.99	3.93	0.000	-27	11	-8
		0.749	0.283	15	0.121	0.846	0.331	3.78	3.73	0.000	30	-4	-5
		0.898	0.400	10	0.200	0.864	0.331	3.76	3.71	0.000	9	-82	10
		0.619	0.237	19	0.085	0.949	0.445	3.62	3.58	0.000	-42	32	-8
		0.973	0.557	6	0.318	0.994	0.704	3.43	3.39	0.000	-51	14	22
		0.996	0.673	3	0.486	1.000	0.900	3.27	3.24	0.001	-39	-46	13
		0.999	0.673	2	0.577	1.000	0.900	3.27	3.24	0.001	-6	5	-5
		0.999	0.673	2	0.577	1.000	0.915	3.21	3.18	0.001	-21	-97	7
		1.000	0.707	1	0.707	1.000	0.915	3.17	3.15	0.001	24	-85	-29
		0.996	0.673	3	0.486	1.000	0.915	3.17	3.14	0.001	15	-7	-23
		1.000	0.707	1	0.707	1.000	0.915	3.15	3.13	0.001	-18	35	19

table shows 3 local maxima more than 8.0mm apart

Height threshold: T = 3.12, p = 0.001 (1.000)
Extent threshold: k = 0 voxels, p = 1.000 (1.000)
Expected voxels per cluster, <k> = 6.509
Expected number of clusters, <c> = 11.40
FWEp: 4.786, FDRp: 4.688, FWEc: 727, FDRc: 727

Degrees of freedom = [1.0, 310.0]
FWHM = 11.4 11.7 11.4 mm mm mm; 3.8 3.9 3.8 {voxels}
Volume: 1799415 = 66645 voxels = 1065.9 resels
Voxel size: 3.0 3.0 3.0 mm mm mm; (resel = 56.22 voxels)

Labels: *volume summary (labels and distances for entire volume)*

x,y,z mm	label	dist mm					
45 -10 64	Precentral_R	0.00	Frontal_Mid_R	4.12	Frontal_Sup_R	8.06	
48 -22 55	Postcentral_R	0.00	Precentral_R	4.58	Parietal_Inf_R	9.85	
39 -37 67	Postcentral_R	0.00	Precentral_R	9.11	Parietal_Sup_R	9.11	
-18 -52 -23	Cerebelum_4_5_L	0.00	Cerebelum_6_L	2.24	Fusiform_L	8.06	
42 -19 16	Rolandic_Oper_R	0.00	Heschl_R	2.24	Insula_R	3.00	
-27 11 -8	Putamen_L	1.41	Insula_L	4.24	Frontal_Sup_Orb_L	6.78	
30 -4 -5	Putamen_R	0.00	Pallidum_R	2.24	Amygdala_R	7.00	
9 -82 10	Calcarine_R	0.00	Cuneus_R	4.58	Calcarine_L	5.00	
-42 32 -8	Frontal_Inf_Orb_L	0.00	Frontal_Inf_Tri_L	6.00	Frontal_Mid_Orb_L	10.20	
-51 14 22	Frontal_Inf_Oper_L	0.00	Frontal_Inf_Tri_L	2.24	Precentral_L	7.81	
-39 -46 13	Temporal_Mid_L	3.74	Temporal_Sup_L	5.10	Rolandic_Oper_L	9.06	
-6 5 -5	Caudate_L	0.00	Pallidum_L	3.74	Putamen_L	4.69	
-21 -97 7	Occipital_Mid_L	0.00	Occipital_Sup_L	5.92	Occipital_Inf_L	11.45	
24 -85 -29	Cerebelum_Crus1_R	0.00	Cerebelum_Crus2_R	4.24	Cerebelum_6_R	8.60	
15 -7 -23	ParaHippocampal_R	0.00	Hippocampus_R	5.92	Amygdala_R	8.66	
-18 35 19	Cingulum_Ant_L	4.24	Frontal_Sup_Medial_L	10	Frontal_Mid_L	5.83	

Figure 65: SPM results of RUN 1. Motor imagery left. The biggest clusters are marked green, and the corresponding anatomical labels are marked red.

9.1.2 Right hand imagination

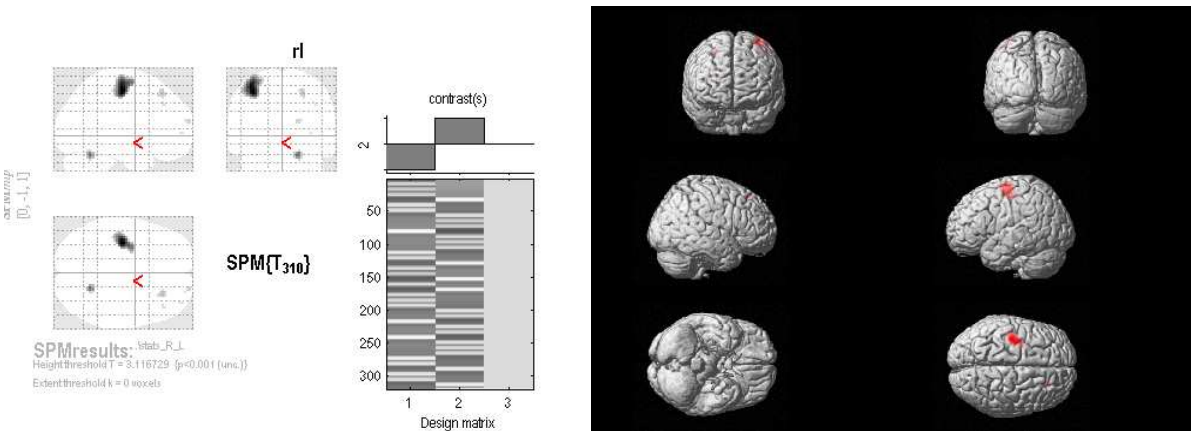

Statistics: *p-values adjusted for search volume*

set-level		cluster-level				peak-level					mm mm mm		
p	c	$p_{FWE-corr}$	$q_{FDR-corr}$	k_E	p_{uncorr}	$p_{FWE-corr}$	$q_{FDR-corr}$	T	(Z=)	p_{uncorr}			
0.970	6	0.000	0.000	248	0.000	0.000	0.000	6.44	6.23	0.000	-36	-16	52
						0.013	0.005	5.10	5.00	0.000	-33	-7	64
		0.351	0.114	29	0.038	0.050	0.012	4.78	4.70	0.000	18	-55	-23
		0.619	0.169	19	0.085	0.964	0.585	3.58	3.54	0.000	27	35	52
		0.959	0.422	7	0.281	0.999	0.884	3.34	3.31	0.000	21	65	19
		0.996	0.577	3	0.486	1.000	0.884	3.27	3.24	0.001	39	35	40
		0.999	0.577	2	0.577	1.000	0.884	3.17	3.15	0.001	36	56	4

Labels : *volume summary (labels and distances for entire volume)*

x,y,z mm	label	dist mm				
-36 -16 52	Precentral_L	0.00	Postcentral_L	4.47	Frontal_Mid_L	10.20
-33 -7 64	Precentral_L	0.00	Frontal_Sup_L	2.45	Frontal_Mid_L	3.16
18 -55 -23	Cerebelum_6_R	0.00	Cerebelum_4_5_R	2.45	Fusiform_R	9.27
27 35 52	Frontal_Sup_R	0.00	Frontal_Mid_R	2.45	Frontal_Sup_Medial_R	7.57
21 65 19	Frontal_Sup_R	0.00	Frontal_Sup_Medial_R	20	Frontal_Mid_R	5.92
39 35 40	Frontal_Mid_R	0.00	Frontal_Inf_Tri_R	12.41	Frontal_Sup_R	13.19
36 56 4	Frontal_Mid_R	0.00	Frontal_Sup_R	5.66	Frontal_Mid_Orb_R	6.00

Height threshold: T = 3.12, p = 0.001 (1.000)
Extent threshold: k = 0 voxels, p = 1.000 (1.000)
Expected voxels per cluster, <k> = 6.509
Expected number of clusters, <c> = 11.40
FWEp: 4.786, FDRp: 4.784, FWEc: 248, FDRc: 248

Degrees of freedom = [1.0, 310.0]
FWHM = 11.4 11.7 11.4 mm mm mm; 3.8 3.9 3.8 {voxels}
Volume: 1799415 = 66645 voxels = 1065.9 resels
Voxel size: 3.0 3.0 3.0 mm mm mm; (resel = 56.22 voxels)

Figure 66: SPM results of RUN 1. Motor imagery right. The biggest clusters are marked green, and the corresponding anatomical labels are marked red.

9.1.3 Passive to Active phase

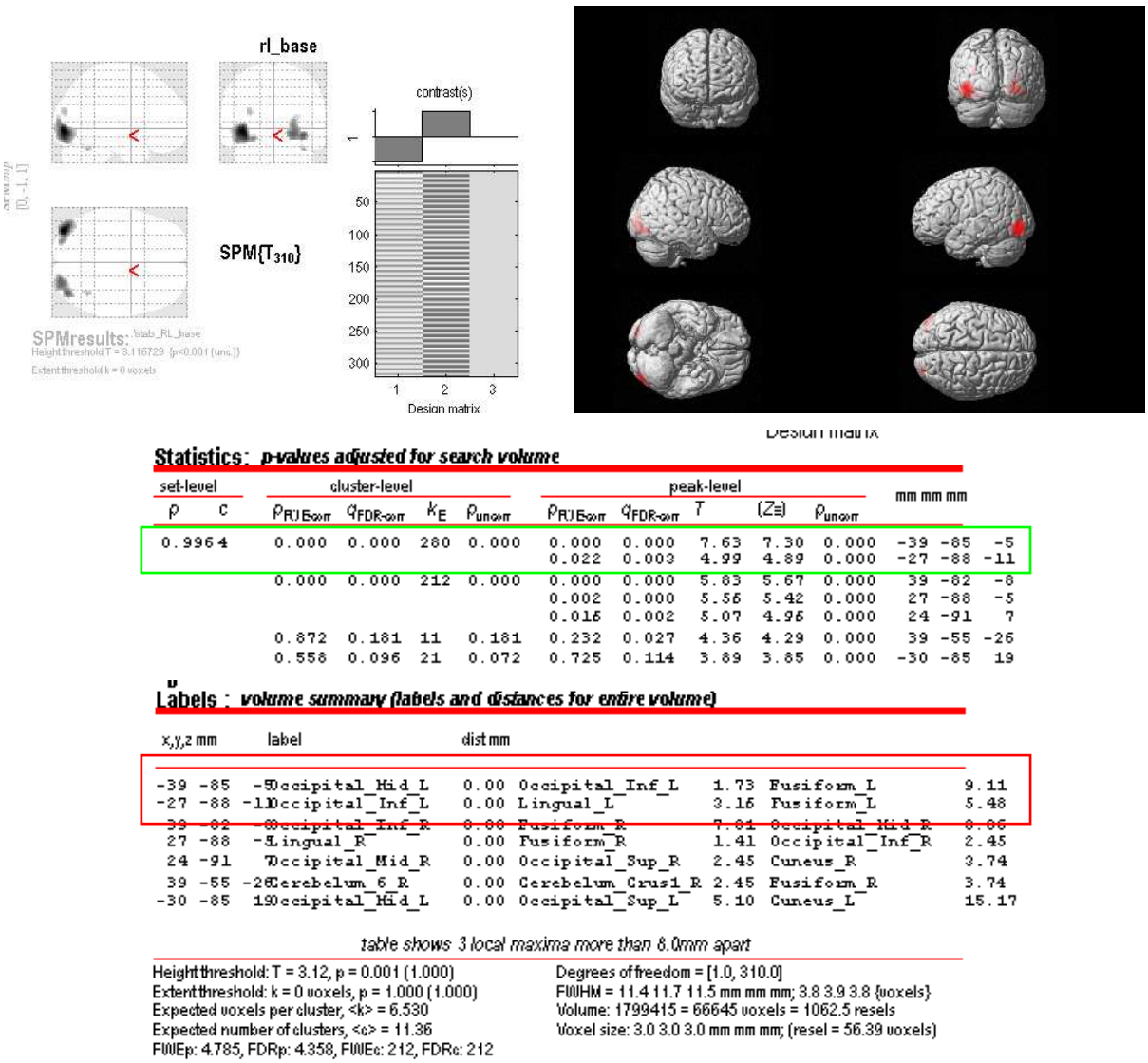

set-level		cluster-level				peak-level					mm mm mm		
p	c	$p_{FWE-corr}$	$q_{FDR-corr}$	k_E	p_{uncorr}	$p_{FWE-corr}$	$q_{FDR-corr}$	T	(Z≡)	p_{uncorr}			
0.9964		0.000	0.000	280	0.000	0.000	0.000	7.63	7.30	0.000	-39	-85	-5
						0.022	0.003	4.99	4.89	0.000	-27	-88	-11
		0.000	0.000	212	0.000	0.000	0.000	5.83	5.67	0.000	39	-82	-8
						0.002	0.000	5.56	5.42	0.000	27	-88	-5
						0.016	0.002	5.07	4.96	0.000	24	-91	7
		0.872	0.181	11	0.181	0.232	0.027	4.36	4.29	0.000	39	-55	-26
		0.558	0.096	21	0.072	0.725	0.114	3.89	3.85	0.000	-30	-85	19

x,y,z mm	label	dist mm					
-39 -85 -5	Occipital_Mid_L	0.00	Occipital_Inf_L	1.73	Fusiform_L	9.11	
-27 -88 -11	Occipital_Inf_L	0.00	Lingual_L	3.16	Fusiform_L	5.48	
39 -82 -8	Occipital_Inf_R	0.00	Fusiform_R	7.81	Occipital_Mid_R	8.06	
27 -88 -5	Lingual_R	0.00	Fusiform_R	1.41	Occipital_Inf_R	2.45	
24 -91 7	Occipital_Mid_R	0.00	Occipital_Sup_R	2.45	Cuneus_R	3.74	
39 -55 -26	Cerebelum_6_R	0.00	Cerebelum_Crus1_R	2.45	Fusiform_R	3.74	
-30 -85 19	Occipital_Mid_L	0.00	Occipital_Sup_L	5.10	Cuneus_L	15.17	

Figure 67: SPM results of RUN 1. Motor imagery passive to active. The biggest clusters are marked green, and the corresponding anatomical labels are marked red.

9.2 SPM fMRI results RUN 2

9.2.1 Left hand imagination

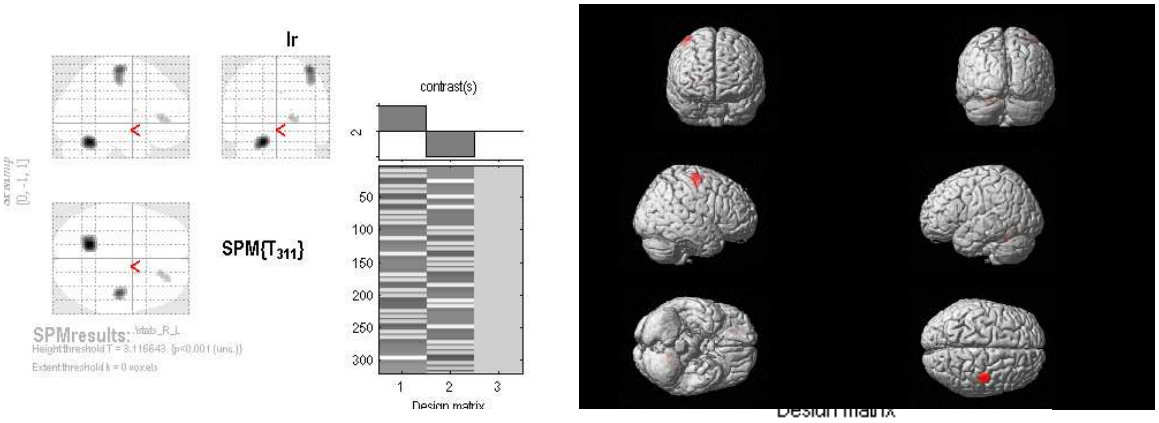

Statistics: *p-values adjusted for search volume*

set-level		cluster-level				peak-level					mm mm mm		
p	c	$p_{FWE-corr}$	$q_{FDR-corr}$	k_E	p_{uncorr}	$p_{FWE-corr}$	$q_{FDR-corr}$	T	(Z≡)	p_{uncorr}			
0.853	5	0.003	0.002	175	0.000	0.000	0.000	6.23	6.04	0.000	-18	-55	-23
		0.006	0.002	151	0.001	0.009	0.004	5.09	4.99	0.000	42	-16	64
						0.109	0.037	4.46	4.39	0.000	45	-16	55
		0.358	0.101	38	0.061	0.673	0.267	3.80	3.75	0.000	18	38	7
						0.888	0.419	3.57	3.54	0.000	24	44	4
		0.997	0.780	1	0.780	0.997	0.893	3.21	3.18	0.001	6	5	37
		0.993	0.780	2	0.675	0.999	0.893	3.16	3.14	0.001	18	2	16

Labels : *volume summary (labels and distances for entire volume)*

x,y,z mm			label	dist mm					
-18	-55	-23	Cerebelum_6_L	0.00	Cerebelum_4_5_L	2.45	Fusiform_L		8.12
42	-16	64	Precentral_R	0.00	Postcentral_R	7.48	Frontal_Sup_R		9.38
45	-16	55	Precentral_R	0.00	Postcentral_R	2.45	Frontal_Mid_R		8.60
18	38	7	Cingulum_Ant_R	3.00	Frontal_Sup_Medial	8R06	Frontal_Med_Orb_R		10.05
24	44	4	Frontal_Mid_R	2.83	Frontal_Sup_Medial	4R47	Cingulum_Ant_R		6.00
6	5	37	Cingulum_Mid_R	0.00	Cingulum_Mid_L	6.16	Cingulum_Ant_R		9.06
18	2	16	Caudate_R	0.00	Putamen_R	6.32	Pallidum_R		10.00

Height threshold: T = 3.12, p = 0.001 (0.999)
Extent threshold: k = 0 voxels, p = 1.000 (0.999)
Expected voxels per cluster, <k> = 10.770
Expected number of clusters, <c> = 7.31
FWEp: 4.672, FDRp: 4.460, FWEc: 151, FDRc: 151

Degrees of freedom = [1.0, 311.0]
FWHM = 13.8 13.7 13.3 mm mm mm; 4.6 4.6 4.4 {voxels}
Volume: 1850931 = 68553 voxels = 665.7 resels
Voxel size: 3.0 3.0 3.0 mm mm mm; (resel = 93.00 voxels)

Figure 68: SPM results of RUN2. Motor imagery left. The biggest clusters are marked green, and the corresponding anatomical labels are marked red.

9.2.2 Right hand imagination

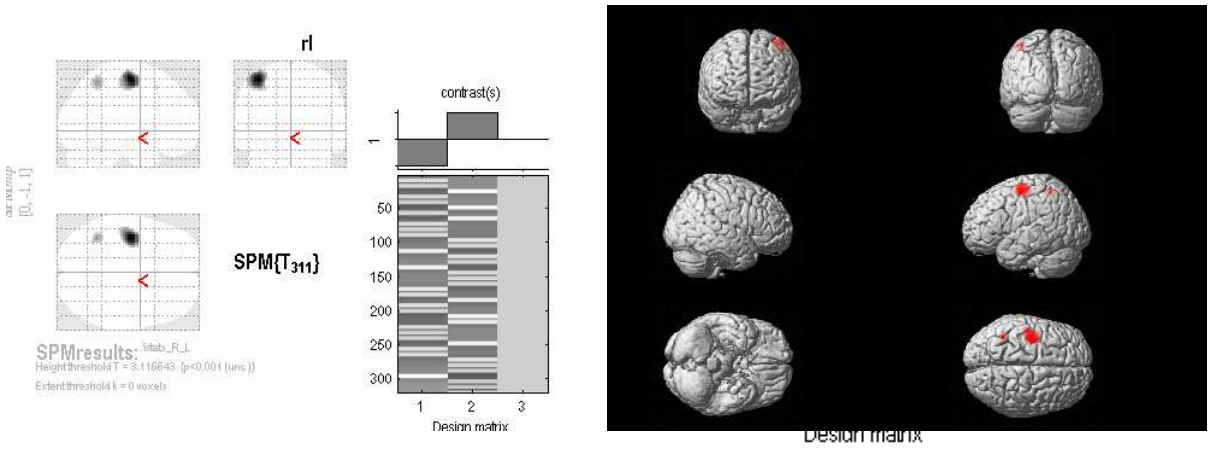

Statistics: ***p-values adjusted for search volume***

set-level		cluster-level				peak-level					mm mm mm		
p	c	$p_{FWE-corr}$	$q_{FDR-corr}$	k_E	p_{uncorr}	$p_{FWE-corr}$	$q_{FDR-corr}$	T	(Z=)	p_{uncorr}			
0.977	3	0.000	0.000	250	0.000	0.002	0.001	5.46	5.33	0.000	-39	-10	61
		0.223	0.052	50	0.035	0.626	0.231	3.80	3.75	0.000	-39	-52	55
		0.993	0.675	2	0.675	0.997	0.816	3.20	3.17	0.001	-30	20	52

Labels : ***volume summary (labels and distances for entire volume)***

x,y,z mm	label	dist mm					
-39 -10 61	Precentral_L	0.00	Postcentral_L	7.35	Frontal_Sup_L	8.83
-39 -52 55	Parietal_Inf_L	0.00	Parietal_Sup_L	4.24	Postcentral_L	9.49
-30 20 52	Frontal_Mid_L	0.00	Frontal_Sup_L	6.32	Precentral_L	13.11

table shows 3 local maxima more than 8.0mm apart

Height threshold: T = 3.12, p = 0.001 (0.999)
Extent threshold: k = 0 voxels, p = 1.000 (0.999)
Expected voxels per cluster, <k> = 10.770
Expected number of clusters, <c> = 7.31
FWEp: 4.672, FDRp: 5.460, FWEc: 250, FDRc: 250

Degrees of freedom = [1.0, 311.0]
FWHM = 13.8 13.7 13.3 mm mm mm; 4.6 4.6 4.4 {voxels}
Volume: 1850931 = 68553 voxels = 665.7 resels
Voxel size: 3.0 3.0 3.0 mm mm mm; (resel = 93.00 voxels)

Figure 69: SPM results of RUN2. Motor imagery right. The biggest clusters are marked green, and the corresponding anatomical labels are marked red.

9.3 SPM fMRI results RUN 3

9.3.1 Left hand imagination

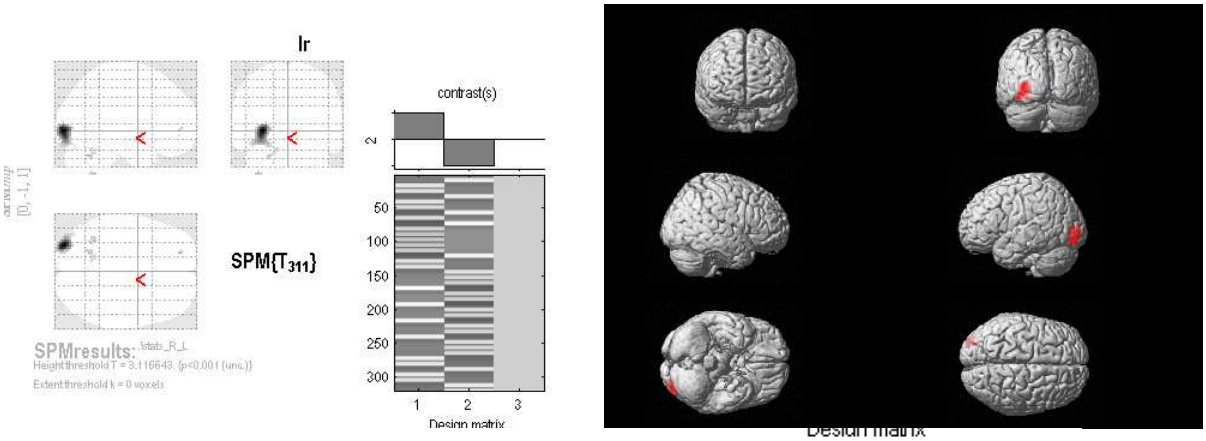

Statistics: *p-values adjusted for search volume*

set-level		cluster-level				peak-level					mm mm mm		
p	c	$p_{FWE-corr}$	$q_{FDR-corr}$	k_E	p_{uncorr}	$p_{FWE-corr}$	$q_{FDR-corr}$	T	(Z≡)	p_{uncorr}			
0.793	5	0.002	0.001	209	0.000	0.024	0.029	4.83	4.74	0.000	-30	-91	1
		0.983	0.770	3	0.616	0.931	0.970	3.47	3.43	0.000	-21	50	1
		0.841	0.691	13	0.276	0.960	0.970	3.40	3.37	0.000	-21	-58	-29
						0.994	0.970	3.23	3.20	0.001	-12	-55	-20
		0.954	0.770	6	0.464	0.966	0.970	3.38	3.35	0.000	-36	-52	-50
		0.995	0.792	1	0.792	0.999	0.983	3.12	3.10	0.001	-51	50	-5

Labels: *volume summary (labels and distances for entire volume)*

x,y,z mm	label	dist mm					
-30 -91	Occipital_Mid_L	0.00	Occipital_Inf_L	5.83	Occipital_Sup_L	12.08	
-21 50	Frontal_Sup_L	0.00	Frontal_Sup_Orb_L	3.74	Frontal_Mid_L	4.24	
-21 -58 -29	Cerebelum_6_L	0.00	Cerebelum_Crus1_L	6.78	Cerebelum_4_5_L	7.35	
-12 -55 -20	Cerebelum_4_5_L	0.00	Cerebelum_6_L	3.00	Vermis_4_5	8.31	
-36 -52 -50	Cerebelum_8_L	0.00	Cerebelum_7b_L	5.66	Cerebelum_Crus2_L	8.25	
-51 50 -5	Frontal_Mid_Orb_L	1.41	Frontal_Inf_Orb_L	4.24	Frontal_Inf_Tri_L	5.10	

table shows 3 local maxima more than 8.0mm apart

Height threshold: T = 3.12, p = 0.001 (0.999)
Extent threshold: k = 0 voxels, p = 1.000 (0.999)
Expected voxels per cluster, <k> = 11.842
Expected number of clusters, <c> = 6.66
FWEp: 4.647, FDRp: 4.833, FWEc: 209, FDRc: 209

Degrees of freedom = [1.0, 311.0]
FWHM = 14.2 14.1 13.8 mm mm mm; 4.7 4.7 4.6 {voxels}
Volume: 1839267 = 68121 voxels = 601.3 resels
Voxel size: 3.0 3.0 3.0 mm mm mm; (resel = 102.26 voxels)

Figure 70: SPM results of RUN 3. Motor imagery left. The biggest clusters are marked green, and the corresponding anatomical labels are marked red.

9.3.2 Right hand imagination

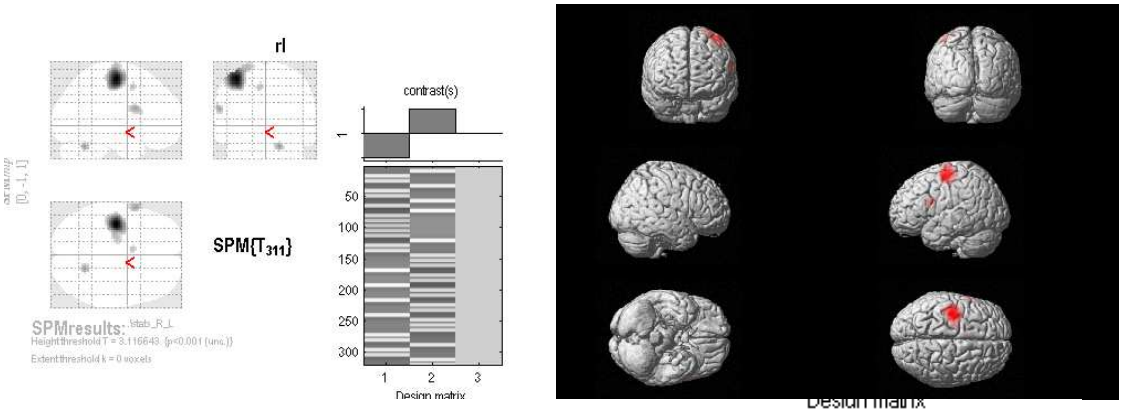

Statistics: *p-values adjusted for search volume*

set-level		cluster-level				peak-level					mm mm mm		
p	c	$p_{FWE-corr}$	$q_{FDR-corr}$	k_E	p_{uncorr}	$p_{FWE-corr}$	$q_{FDR-corr}$	T	(Z≡)	p_{uncorr}			
0.899	4	0.000	0.000	499	0.000	0.000	0.000	7.65	7.32	0.000	-39	-13	61
		0.395	0.101	37	0.025	0.097	0.031	4.47	4.39	0.000	18	-55	-26
		0.191	0.064	57	0.032	0.156	0.034	4.33	4.26	0.000	-60	11	22
		0.678	0.170	21	0.170	0.767	0.219	3.68	3.64	0.000	-9	5	49

Labels: *volume summary (labels and distances for entire volume)*

x,y,z mm	label	dist mm					
-39 -13 61	Precentral_L	0.00	Postcentral_L	7.14	Frontal_Sup_L	9.95
18 -55 -26	Cerebelum_6_R	0.00	Cerebelum_4_5_R	3.00	Cerebelum_9_R	10.05
-60 11 22	Frontal_Inf_Oper_L	0.00	Precentral_L	3.00	Frontal_Inf_Tri_L	6.71
-9 5 49	Supp_Motor_Area_L	0.00	Frontal_Sup_L	4.36	Cingulum_Mid_L	5.20

table shows 3 local maxima more than 8.0mm apart

Height threshold: T = 3.12, p = 0.001 (0.999)
Extent threshold: k = 0 voxels, p = 1.000 (0.999)
Expected voxels per cluster, <k> = 11.842
Expected number of clusters, <c> = 6.66
FWEp: 4.647, FDRp: 4.331, FWEc: 499, FDRc: 499

Degrees of freedom = [1.0, 311.0]
FWHM = 14.2 14.1 13.8 mm mm mm; 4.7 4.7 4.6 {voxels}
Volume: 1839267 = 68121 voxels = 601.3 resels
Voxel size: 3.0 3.0 3.0 mm mm mm; (resel = 102.26 voxels)

Figure 71: SPM results of RUN 3. Motor imagery right. The biggest clusters are marked green, and the corresponding anatomical labels are marked red.